INVESTIGATION OF THE SPUTTERING CONDITIONS OF NIOBIUM AND MAGNETITE THIN FILMS FOR REALIZING FERROMAGNETIC JOSEPHSON JUNCTIONS

by

TUNA ALP

Submitted to the Graduate School of Engineering and Natural Sciences

in partial fulfillment of

the requirements for the degree of Master of Science

Sabanci University

Spring 2023

ABSTRACT

INVESTIGATION OF THE SPUTTERING CONDITIONS OF NIOBIUM AND MAGNETITE THIN FILMS FOR REALIZING FERROMAGNETIC JOSEPHSON JUNCTIONS

TUNA ALP

Master of Science Dissertation, July 2023

Supervisor: Asst. Prof. Dr. Yılmaz Şimşek

Keywords: Iron Oxide, Niobium, Magnetite, Superconductivity, Ferromagnetism, Josephson Junctions, X-Ray Diffraction, Vibrating Sample Magnetometry, Raman Spectroscopy, Magnetic Force Microscopy

Ferromagnetic Josephson junctions have attracted a great deal of interest for superconducting electronics and cryogenic memory devices since their sandwiched heterostructures exhibit the coexistence of superconductivity and magnetism, which comprises rich physics concepts such as Fulde-Ferrell-Larkin-Ovchinnikov pairing, Andreev bound states, anomalous current-phase behavior due to phase shifting, spin triplet supercurrent valving due to ferromagnetic tunneling domains and mutual proximity effects. These versatile junctions offer new approaches in developing new cryogenic quantum devices such as phase qubits, spin valve-based memory circuits and phase shifters for programmable logic circuits. In this work, an optimized sputtering system have been systematically studied to achieve high superconducting characteristics in niobium layers and ferromagnetic-insulator characteristics in iron oxide layers for ultimately realizing new-type π-junctions. For this purpose, a series of niobium and iron oxide thin films on periclase and sapphire substrates have been grown under various magnetron sputtering conditions from niobium and magnetite targets respectively. Their

structural electrical and magnetic characteristics have been analyzed by X-ray diffraction, Raman spectroscopy, vibrating sample magnetometry, magnetic force microscopy, and electrical transport measurements. The best growth condition was employed to deposit each layer of coplanar Nb/Fe_3O_4/Nb junctions. In addition to the film deposition by sputtering, thermal and e-beam evaporation, electron beam lithography and non-reactive ion etching was employed to form the coplanar junction arrays. The resulting effects of different in-situ growing temperatures on surface morphology, crystal structure, electrical and magnetic responses were investigated for iron oxide thin films. The effects of crystalline quality and size on the superconductive transition of niobium thin films are discussed. For electrical characterization of the coplanar Josephson junctions, 4-point transport measurements are carried out under various magnetic fields in a cryogenic system from room temperature down to 2 K. The prerequisite signatures of π-junctions were investigated in their Fraunhofer patterns, and temperature dependence of I_c and I_cR_N products. The effects of the growth and fabrication conditions on these properties are discussed in order to realize ideal ferromagnetic-insulator based Josephson junction layers for applications of cryogenic memory and phase qubits.

ÖZET

FERROMANYETİK JOSEPHSON EKLEMLERİNİN OLUŞTURULMASI İÇİN NİYOBYUM VE MAGNETİT İNCE FİLMLERİN PÜSKÜRTME KOŞULLARININ İNCELENMESİ

TUNA ALP

Yüksek Lisans Tezi, Temmuz 2023

Tez Danışmanı: Dr. Öğr. Üyesi Yılmaz Şimşek

Anahtar Kelimeler: Demir Oksit, Niyobyum, Magnetit, Süperiletkenlik, Josephson Eklemleri, X-Işını Kırınımı, Titreşimli Numune Manyetometresi, Raman Spektroskopisi, Manyetik Kuvvet Mikroskopisi

Ferromanyetik Josephson eklemleri süperiletken elektronik ve kriyojenik bellek cihazları için büyük ilgi görmüştür, çünkü sandviç heteroyapıları Fulde-Ferrell-Larkin-Ovchinnikov eşleşmesi, Andreev bağıl durumları, faz kayması nedeniyle anormal akım-faz davranışı, ferromanyetik tünelleme alanları ve karşılıklı yakınlık etkileri nedeniyle spin üçlü süper akım vanası gibi zengin fizik kavramlarını içeren süperiletkenlik ve manyetizmanın bir arada var olduğu yapılardır. Bu çok yönlü eklemler, faz kübitleri, spin valf tabanlı bellek devreleri ve programlanabilir mantık devreleri için faz kaydırıcılar gibi yeni kriyojenik kuantum cihazlarının geliştirilmesinde yeni yaklaşımlar sunmaktadır. Bu çalışmada, niyobyum katmanlarında yüksek süper iletkenlik özellikleri ve demir oksit katmanlarında ferromanyetik yalıtkanlık özellikleri elde etmek için optimize edilmiş bir püskürtme sistemi sistematik olarak incelenmiş ve sonuçta yeni tip π-eklemler oluşturulmuştur. Bu amaçla, periklaz ve safir alt tabakalar üzerinde bir dizi

niyobyum ve demir oksit ince film, sırasıyla niyobyum ve manyetit hedeflerden çeşitli magnetron püskürtme koşulları altında büyütülmüştür. Yapısal elektriksel ve manyetik özellikleri X-ışını kırınımı, Raman spektroskopisi, titreşimli numune manyetometrisi, manyetik kuvvet mikroskobu ve elektriksel taşınım ölçümleri ile analiz edilmiştir. Eş düzlemli Nb/Fe_3O_4/Nb eklemlerinin her bir katmanını oluşturmak için en iyi büyüme koşulu kullanılmıştır. Eş düzlemli eklemleri oluşturmak için termal ve e-ışın buharlaştırma, elektron demeti litografisi ve reaktif olmayan iyon aşındırma yoluyla film püskürtmeye ek olarak kullanılmıştır. Farklı yerinde büyütme sıcaklıklarının yüzey morfolojisi, kristal yapı, elektriksel ve manyetik tepkiler üzerindeki etkileri demir oksit ince filmler için incelenmiştir. Kristal kalitesi ve boyutunun niyobyum ince filmlerin süper iletkenlik geçişi üzerindeki etkileri tartışılmıştır. Eş düzlemli Josephson bağlantılarının elektriksel karakterizasyonu için, oda sıcaklığından 2 K'e kadar kriyojenik bir sistemde çeşitli manyetik alanlar altında 4 noktalı taşınım ölçümleri gerçekleştirilmiştir. π-eklemlerinin önkoşul durumları Fraunhofer desenlerinde incelenmiş ve I_c ve I_cR_N çarpımının sıcaklığa bağımlılığı tartışılmıştır. Büyüme ve fabrikasyon koşullarının bu özellikler üzerindeki etkileri, kriyojenik bellek ve faz kübitlerinin uygulamaları için ideal ferromanyetik yalıtkan tabanlı Josephson eklem katmanlarını gerçekleştirmek amacıyla bu malzeme seçimi için tartışılmıştır.

ACKNOWLEDGEMENTS

I would like to thank every member of our research group SUQUD for their unlimited support, their persistence and dedication on experimentation and scientific endeavors since the beginning of this research. In addition, I would like to thank the members of BUSPIN research group for their collaboration, scientific contribution, and hospitality at the time I was experimenting in Boğaziçi University. Also, I would like to thank the cleanroom technicians at SUNUM for their help and for sharing their expertise. I would also like to thank my family and friends at Sabancı University and Middle East Technical University for the enlightening brainstorms on fundamental science and new technological frontiers.

Finally, I would like to acknowledge the financial supports of the Scientific and Technological Research Council of Turkey (TÜBİTAK) for the scholarship and research funding awarded under BIDEB-2232 International Fellowship for Outstanding Researchers Support Program (Project ID: 118C339, Project Title: “ A novel route to develop new π-junctions for quantum computing applications”).

Datça güneşine…

TABLE OF CONTENTS

LIST OF FIGURES

LIST OF TABLES

LIST OF ABBREVIATIONS

AB	:	Ambegaokar Baratoff
AC	:	Alternating Current
ABS	:	Andreev Bound States
AFM	:	Atomic Force Microscope
AR	:	Andreev Reflection
BCS	:	Bardeen Cooper Schrieffer
CMOS	:	Complementary Metal-Oxide Semiconductor
CVD	:	Chemical Vapor Deposition
DC	:	Direct Current
EBL	:	Electron Beam Lithography
FC	:	Field Cooling
FCC	:	Face Centered Cubic
Fe-O	:	Iron Oxide
FJJ	:	Ferromagnetic Josephson Junction
ICP	:	Inductive Coupled Plasma
IV	:	Current – Voltage
MFM	:	Magnetic Force Microscopy
MH	:	Magnetization – Auxiliary Field
MIBK	:	Methyl Isobutyl Ketone
MT	:	Magnetization – Temperature
PMMA	:	Polymethyl Methacrylate
PVD	:	Physical Vapor Deposition
PID	:	Proportion – Integral – Derivative
PPMS	:	Physical Property Measurement System
QCM	:	Quartz Crystal Monitor
RCSJ	:	Resistively and Capacitively Shunted Junction
RF	:	Radio Frequency
RIE	:	Reactive Ion Etching
RT	:	Resistance – Temperature
SEM	:	Scanning Electron Microscope
SF	:	Superconductor – Ferromagnet

SFQ	:	Superconducting Flux Qubit
SFS	:	Superconductor – Ferromagnet - Superconductor
SQUID	:	Superconducting Quantum Interference Device
SUNUM	:	Sabancı University Nanotechnology Application and Research Center
VSM	:	Vibrating Sample Magnetometry
VTI	:	Variable Temperature Inert
XRD	:	X-Ray Diffraction

1. INTRODUCTION

Superconducting tunneling junctions or Josephson junctions are one of the biggest discoveries in the 20th century, where new conceptual and technological approaches were gradually triggered in development of various macroscopic quantum circuits. Today, they are promising candidates for the cryogenic applications such as superconducting quantum interference devices (SQUID),[1] high resolution bolometers,[2] artificial terahertz emitters,[3] spin valves for spintronic circuits,[4] and superconducting qubits.[5] Especially, they are considered as primary elements in constructing a quantum computing circuit, because they can be lithographically manufactured and be easily manipulated by external fields and additionally their macroscopic quantum characteristics allow various operations and readout options. Therefore, they are widely used as a superconducting qubit (s-qubit) in the development of quantum computing circuits. Albeit with various advantages of the s-qubits, there are major obstacles in their implementations to the quantum technology such as decoherence disrupting the superposition states and the stored information through interactions of the qubits with the environment. Due to these problems, new approaches and concepts are still needed in the research and development of s-qubits. More recently, ferromagnetic Josephson junctions (FJJ, also so-called π-junctions) offer innovative approaches to the s-qubit technologies and rich physics concepts such as triplet superconductivity, odd-frequency pairing, Fulde-Ferrell-Larkin-Ovchinnikov pairing, long-range equal-spin supercurrents, π-junctions, and mutual proximity effects because the sandwiched stack of superconducting and magnetic layers comprises the coexistence of superconductivity and magnetism.[6] Therefore, FJJs have been extensively studied over the past 20 years. The presence of the magnetic tunneling barrier between two superconducting electrodes induces spit-triplet cooper pairs during the tunneling event which enables to develop a spin-valve system for cryogenic memory devices.[6–11] The coexistence of ferromagnetism and superconductivity in FJJs also enable the development of new superconducting qubits which can be used as a phase shifter in programmable logic circuits and an integrating element with other conventional Josephson junctions in

superconducting flux qubit (SFQ) circuits.[11–14] In a superconducting circuit, the ferromagnetic layer in the π-junctions allows to tune the phase of the ground state of a junction, which opens access to low energy excitations inside a finite potential well. With a proper tuning, the junction platform can act a phase qubit in which the excitations and readouts are carried out in terms of applied currents and microwave pulses to the junction. Since there are still unexplored territory in the new concept, and some problems in their implementations into quantum circuit, many research groups still focus on designing and development of new FJJs. As a result of the extensive research activities, experimental achievements approach to the extraordinary Josephson effects in FJJs by demonstrating spin-triplet supercurrent in their tunneling characteristics, thickness induced 0-π transitions and cusp structure on the temperature dependence of critical current.[6,8] However, it is very hard to achieve ideal ferromagnetic characteristic in the ultra-thin tunneling barrier between superconducting layers and additionally high-quality interface between layers.[15] Even if desired ferromagnetic layer is achieved with a high-quality interface feature in a FJJs, its electrical characteristic also plays a crucial role in their performance. For example, π-junction characteristics have been observed in conventional FJJs which comprise a ferromagnetic-metallic barrier such as CuNi, PdNi (weak ferromagnets), Ni, Fe, Co, NiFe (strong ferromagnets). However, the presence of ferromagnetic metals between superconducting electrodes causes low-energy quasi-particle excitations, which is an origin of the strong dissipation and also a weak voltage jump across the junctions which cannot be sufficiently monitored by nanovoltmeters. In some theoretical studies it was envisioned that Josephson junctions with a ferromagnetic insulating barrier (FIJJs) can be promising candidates to solve the quasiparticle dissipation and increase the voltage jump across the junction.[16–18] In spite of a large number of ferromagnetic materials exhibiting metallic or semiconducting behaviors, there are few ferromagnetic insulators such as magnetite (Fe_3O_4), EuS, EuO, YIG, LaCoO3 and GdN. In this work, magnetite was preferred as FI barrier to realize π-junctions due to its unique electrical and magnetic properties, high curie temperature and high spin polarization. For example, magnetite shows a half-metallic behavior at room temperature while it becomes an insulator below 120 K because of a structural phase transition from a cubic to monoclinic structure.[19] For this purpose, a systematic experimental program has been implemented to optimize the magnetron sputtering conditions for separately depositing the ferromagnetic iron oxide and superconducting niobium (Nb) films on MgO (100)

and Al_2O_3 (0001) substrates. Crystallographic and transport properties of niobium and iron oxide thin films are investigated, where the results are discussed together with the morphological, magnetic, and chemical properties of iron oxide films. The best growth conditions for each layer were determined by characterizing their structural, magnetic and electrical properties using X-ray diffraction (XRD), Raman spectroscopy, vibrating sample magnetometry (VSM) and low-temperature transport electrical measurements. The ideal growth conditions were employed in the deposition of the superconducting and ferromagnetic insulating layers of a coplanar Josephson junction arrays on MgO and Al_2O_3 substrates. In the fabrication of the FI-JJ arrays thermal and e-beam evaporation, electron beam lithography and non-reactive ion etching techniques were used. The temperature dependence of the transport characteristics of the coplanar FI-JJs have been measured under various external magnetic fields in the cryogenic system from room temperature down to 2 K. Their transport characteristics have been systematically studied for the prerequisite signatures of π-junctions such as π-phase shift, and spin-triplet supercurrents in their Fraunhofer patterns, and temperature dependent of I_c and I_cR_N products. The growth and fabrication conditions are discussed to correlate crystalline structure and electrical/magnetic behaviors of each layer. The results are promising for the ultimate goal of the research project aiming at realizing an ideal ferromagnetic insulator-based Josephson junction for cryogenic memory and phase qubit systems.

2. THEORY & FUNDAMENTALS

In this part, the fundamental discoveries on the theory of superconductivity, superconductive tunneling and properties of magnetite and maghemite are covered in detail with a chronological order.

2.1. Superconductivity: Foundation and Persistent Currents

Superconductivity is a quantum mechanical phenomenon where below a critical temperature the resistivity of a material suddenly drops down to zero. It is discovered by Heike Kamerlingh Onnes in 1911, where Onnes observed the resistance of solid mercury disappeared below a certain critical temperature. The discovery was awarded with a Nobel prize in 1913.[20]

In normal metals, it is impossible to obtain a perpetual electric current since charges dissipate their energies due to the resistance of the material. However, in a superconductor charge carriers can travel freely without any energy dissipation since there is no resistance. This phenomenon is often referred as *infinite current* or *persistent current* which is also discovered by Kamerlingh Onnes and reported in 1914.[20]

If we combine the Coulomb's force with Newton's equation of motion, we have

$$\ddot{r} = -\frac{e}{m_e}\vec{E} \tag{1}$$

where m_e is the mass of the electron and e is the elementary charge.

Now, if we define the current density for a number of superconducting electrons n_s

$$\vec{J} = -en_s\dot{\vec{r}} \tag{2}$$

and by taking the time derivative

$$\dot{\vec{J}} = \frac{n_s e^2}{m_e} \vec{E} \tag{3}$$

This equation is equivalent to Ohm's law for superconductors in a very classical and rough manner.

2.2. Meissner Effect and London Equations

In 1933, Walther Meissner and Robert Ochsenfeld discovered that in the close vicinity of a superconductor, internal magnetic fields cancel out. It is known as the *Meissner effect*, which states that a superconductor acts also as a perfect diamagnet until an applied critical magnetic field is reached where superconductivity vanishes.[21] For some of the superconductors, there exists a mixed state between two or more critical field points of the applied magnetic field, which will be discussed further in the following subsection.

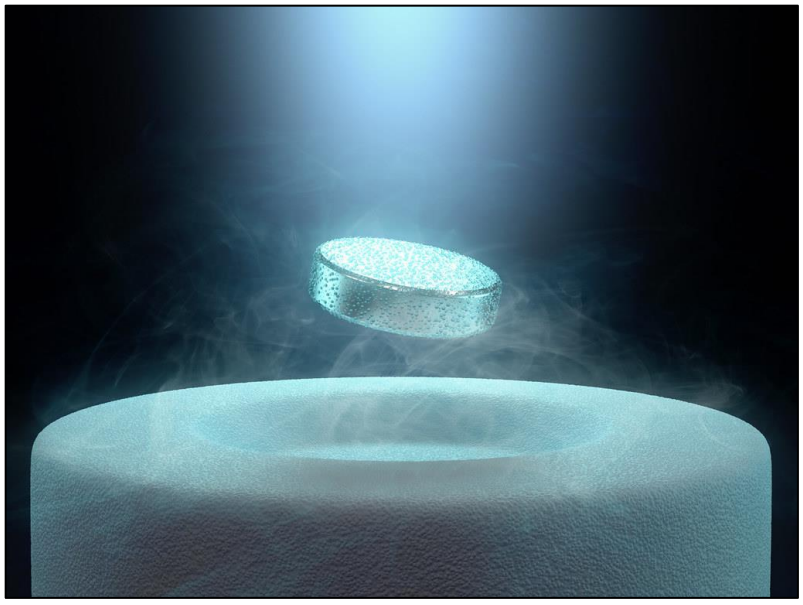

Figure 1. Levitation of a magnet over a high TC superconductor (Picture was obtained from a public article by Vic Comello shared in November 25, 2014 at Argonne National Laboratory government website)

One year after the discovery of Meissner, a paper on the electromagnetic equations of superconductivity was published by London brothers, which gives a description for the supercurrent in terms of vector potential over a diamagnetic volume density.[22]

If we use Faraday's law on the last derived equation for the persistent currents, we have

$$\vec{\nabla} \times \vec{E} = -\frac{1}{c}\dot{\vec{B}} \tag{4}$$

$$\vec{\nabla} \times \dot{\vec{J}} = -\frac{n_s e^2}{m_e c}\dot{\vec{B}} \tag{5}$$

Now, if we use Ampère's law, we have

$$\vec{\nabla} \times \vec{\mathrm{B}} = \frac{4\pi}{c}\vec{J} \tag{6}$$

$$\vec{\nabla} \times \vec{\nabla} \times \dot{\vec{B}} = -\frac{4\pi n_s e^2}{m_e c^2}\dot{\vec{B}} \tag{7}$$

If we use the identity $\vec{\nabla} \times \vec{\nabla} \times \vec{B} = \overrightarrow{\nabla \cdot}\left(\vec{\nabla} \cdot \vec{B}\right) - \nabla^2 \vec{B}$ since we know that the divergence of a magnetic field is zero from Maxwell equations, we have

$$\nabla^2 \dot{\vec{B}} = \frac{1}{{\lambda_l}^2}\dot{\vec{B}} \tag{8}$$

$$\lambda_L = \sqrt{\frac{m_e c^2}{4\pi n_s e^2}} \tag{9}$$

where λ_L is the *London penetration depth*. For the element niobium, London penetration depth is ~40 nm.[23]

Removing the time derivatives in order to consistently capture the Meissner Effect where $B = 0$ at $T < T_c$

$$\nabla^2 \vec{B} = \frac{1}{{\lambda_L}^2}\vec{B} \tag{10}$$

If we combine this with Ampere's law, we have

$$\vec{\nabla} \times \vec{J} = -\frac{n_s e^2}{m_e c}\vec{B} \tag{11}$$

In the choice of Coulomb's gauge, this becomes

$$\vec{J} = -\frac{n_s e^2}{m_e c}\vec{A} \tag{12}$$

which is known as the *London equation*.

2.3. Ginzburg – Landau Theory

A phenomenological approach emerged from Lev Landau and Vitaly Ginzburg in 1950 which defines the macroscopic properties of superconductors by defining a complex order parameter as a macroscopic Schrödinger-like wavefunction.[24]

If we define a free energy functional $\mathcal{F}[(\psi(r)]$ for an order parameter $\psi(r)$ of a superconductor, where the average of the order parameter above the critical temperature is zero and non-zero below. Above the critical temperature, free energy of the normal state should be smaller than the free energy of the superconducting state, therefore the equilibrium point of $\mathcal{F}$ is positive. Below the critical temperature, free energy of the normal state should be larger than the free energy of the superconducting state, therefore the equilibrium point of $\mathcal{F}$ is negative. This indicates that $\mathcal{F}$ should vanish at the critical temperature. Considering the requirements, we can expand $\mathcal{F}$ in even powers of constant ψ

$$\mathcal{F}(\psi, \bar{\psi}) = \alpha|\psi|^2 + \frac{\beta}{2}|\psi|^4 \tag{13}$$

This expansion is known as Landau free energy expansion. For the free energy to be unbounded, the quadratic coefficient must be positive.

We can take the derivative of Landau free energy with respect to $\bar{\psi}$ in order to minimize it

$$\frac{\partial \mathcal{F}}{\partial \bar{\psi}} = \alpha\psi + \beta\bar{\psi}|\psi|^2 = 0 \tag{14}$$

with solutions

$$|\psi| = 0\ (normal\ state) \tag{15}$$

$$|\psi| = \sqrt{-\frac{\alpha}{\beta}}\ (superconducting\ state) \tag{16}$$

So, if the superconducting state solution exists, it gives the global minimum of the Landau free energy. Since $\beta > 0$, in order to have a physical solution $\alpha < 0$ where it changes sign across the critical temperature.

$$\alpha = \alpha'(T - T_C) \tag{17}$$

Now, if we make the expansion for $\psi \to \psi(r)$ we need to take into consideration that the charge carriers are coupling with the electromagnetic field, so we can write down

$$\mathcal{F}\left[\psi(r), \bar{\psi}(r), \vec{A}\right] = \alpha|\psi(r)|^2 + \frac{\beta}{2}|\psi(r)|^4 + \frac{1}{4m_e}\left|\left(\frac{\hbar}{i}\vec{\nabla} + \frac{2e}{c}\vec{A}\right)\psi\right|^2 + \frac{B^2}{8\pi} \tag{18}$$

This is the Ginzburg-Landau free energy expansion where the last two terms are due to the coupling between the charge carriers and electromagnetic field. Notice that the coefficients $e \to 2e$ and $2m \to 4m$, indicating that one charge carrier should consist of two electrons. These corrections were made after the implementation of the microscopic theory by Gor'kov.[25]

Minimizing this functional with respect to the vector potential and using the Maxwell-Ampère law, we can write down the supercurrent equation and the wavefunction solution:

$$\vec{J} = -\frac{e\hbar}{2m_e i}\left(\bar{\psi}\vec{\nabla}\psi - \psi\vec{\nabla}\bar{\psi}\right) - \frac{2e^2\vec{A}}{m_e c}|\psi|^2 \tag{19}$$

$$\psi(r) = \frac{1}{\sqrt{2}}\sqrt{n_s(r)}e^{i\phi(r)} \tag{20}$$

where $\psi(r)$ is the order parameter, $n_s(r)$ is the non-uniform charge carrier density and $\phi(r)$ is the phase of the superconductor. For a uniform charge density, the supercurrent can be represented as

$$\vec{J} = -\frac{e\hbar n_s}{2m_e}\vec{\nabla}\phi - \frac{n_s e^2}{m_e c}\vec{A} \tag{21}$$

where for a uniform phase, the equation reduces to the London equation. This order parameter and supercurrent equation is valid near the critical temperature, where it covers most of the macroscopic properties of the superconductivity.

The supercurrent equation above indicates that there are two important lengths. One is the characteristic length for a weak magnetic field which is introduced as the London penetration depth λ_L in equation (9).

$$\lambda_L = \sqrt{\frac{m_e c^2}{16\pi|\psi|^2 e^2}} \qquad n_s = 4|\psi|^2 \tag{22}$$

The other length is the *coherence length* ξ, which defines the distance of variation of the order parameter. For a perfect superconductor, the coherence length is given such as,

$$\xi(T) = \frac{\hbar v_F}{\pi|\Delta|} \tag{23}$$

where v_F is the Fermi velocity and Δ is the gap energy, which will be discussed in the following subsection.

If we write the ratio of these two lengths, we have

$$\frac{\lambda_L}{\xi} = \kappa \tag{24}$$

This ratio is known as the *Ginzburg-Landau parameter*. Both lengths are temperature dependent in the same order, therefore this ratio is temperature independent. Knowing the fact that this was a remarkable result of the Ginzburg-Landau theory, Alexi Abrikosov stated on his paper that this ratio indicates that there should be two classes of superconductors: Type-I superconductors with $\kappa < 1/\sqrt{2}$ and type-II superconductors with $\kappa > 1/\sqrt{2}$.[26]

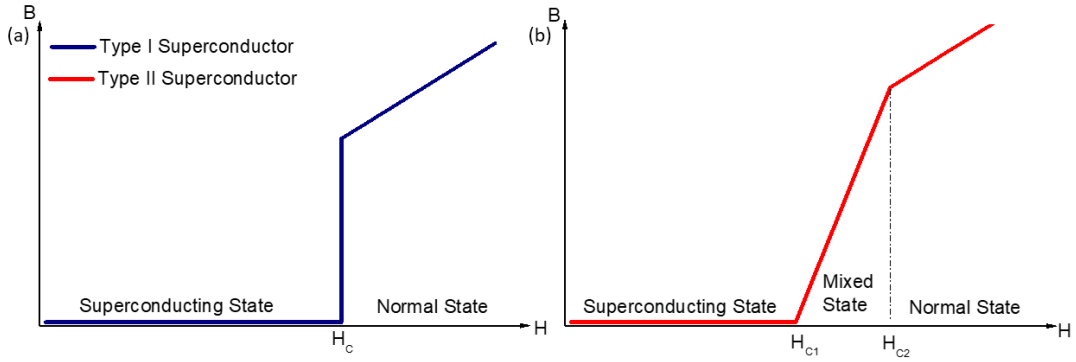

Figure 2. Internal magnetic field vs applied magnetic field plots for (a) type-I and (b) type-II superconductors

For a superconducting region surrounding a normal metal region, the current on a closed path surrounding this region is zero. Therefore, if we integrate the supercurrent equation along this path, we have

$$\frac{\hbar c}{2e} \oint \vec{\nabla}\phi \cdot d\vec{l} = -\oint \vec{A} \cdot d\vec{l} \tag{25}$$

Applying Stoke's theorem to the right hand side:

$$\oint \vec{A} \cdot d\vec{l} = \int (\vec{\nabla} \times \vec{A}) \cdot d\vec{S} = \int \vec{B} \cdot d\vec{S} = \Phi \tag{26}$$

The result of the phase integral is discrete due to the harmonic solution

$$\oint \vec{\nabla}\phi \cdot d\vec{l} = 2\pi n \qquad n = 1,2,\ldots \tag{27}$$

Therefore, we have the magnetic flux as

$$\Phi = \left|\frac{hc}{2e}\right| n = \Phi_0 n \qquad n = 1,2,\ldots \tag{28}$$

$$\Phi_0 = \left|\frac{hc}{2e}\right| \tag{29}$$

where Φ_0 is the *magnetic flux quantum*. This result shows that the magnetic field inside a superconducting loop is quantized.

When a type-II superconductor is in the mixed state, normal metal regions start to emerge inside the superconductor, where an external magnetic field can penetrate through until the last critical field point. After exceeding the last critical field, the whole structure turns into a normal metal region. These normal metal regions are also known as Abrikosov vortices.

2.4. BCS Theory

Ginzburg-Landau theory was an important milestone, where it gives a satisfactory macroscopic explanation for superconductivity and magnetic flux quantization, yet the microscopic explanation for the phenomenon was still not complete at that time. One loose end was the exponential decay of specific heat at superconducting transition, which was an indication of a gap in the energy spectrum of a superconductor. The other one was the isotope effect, where the critical temperature of the superconducting material changes inversely proportional with the atomic mass, which indicates that phonon interactions should be considered for the emergence of superconductivity.[27]

In 1957, a microscopic explanation for superconductivity was published by John Bardeen, Leon Cooper, and Robert Schrieffer, which is now known as their initials:

BCS theory. Essentially, it is based on a variational principle, where the electron coupling is justified due to the electron-phonon exchange.[28]

For two electrons interacting with each other, if we define an arbitrary attractive potential $V = V(\overrightarrow{r_1} - \overrightarrow{r_2})$, we can write down the Schrödinger equation:

$$\left[-\frac{\hbar^2}{2m_e}\nabla_{\overrightarrow{r_1}}{}^2 - \frac{\hbar^2}{2m_e}\nabla_{\overrightarrow{r_2}}{}^2 + V(\vec{r}_1 - \vec{r}_2)\right]\psi(\vec{r}_1, \vec{r}_2) = E\psi(\vec{r}_1, \vec{r}_2) \tag{30}$$

As in two body central mass problem, we can rewrite parameters in terms of relative displacement, position vector for center of mass, total mass, and reduced mass.

$$\left[-\frac{\hbar^2}{2M}\nabla_{\vec{R}_{CoM}}{}^2 - \frac{\hbar^2}{2\mu}\nabla_{\vec{r}}{}^2 + V(\vec{r})\right]\psi(\vec{r}, \vec{R}_{CoM}) = E\psi(\vec{r}, \vec{R}_{CoM}) \tag{31}$$

Where $\vec{R}_{CoM} = (\overrightarrow{r_1} + \overrightarrow{r_2})/2$ is the position of center of mass, $\vec{r} = \vec{r}_1 - \vec{r}_2$ is the relative displacement, $M = 2m_e$ is the total mass, and $\mu = m_e/2$ is the reduced mass. The solution is of the form:

$$\psi(\vec{r}, \vec{R}_{CoM}) = \psi(\vec{r})e^{i\vec{K}\cdot\vec{R}_{CoM}} \tag{32}$$

We are only concerned with the interaction of two particles, therefore since the potential is only depending on relative displacement, we can disregard the center of mass part of the equation. We have

$$\left[-\frac{\hbar^2}{2\mu}\nabla_{\vec{r}}{}^2 + V(\vec{r})\right]\psi(\vec{r}) = E\psi(\vec{r}) \qquad E_n = E - \frac{\hbar^2 K^2}{2M} \tag{33}$$

where E_n is the energy eigenvalue. For the lowest energy eigenvalue, the momentum of the center of mass vanishes. In this case, the coupling electrons have opposite momenta. Due to symmetry, there are even and odd solutions for the spatial wavefunction where the electron spins form either a singlet or a triplet state in order to preserve the anti-symmetry of the complete wavefunction.

Now, if we take the Fourier transform of the equation, we have

$$\psi(\vec{k}) = \int \psi(\vec{r}) e^{-i\vec{k}\cdot\vec{r}}\, d^3r \tag{34}$$

$$\int \frac{d^3k'}{(2\pi)^3} V(\vec{k}-\vec{k}')\,\psi(\vec{k}') = \left(E - 2\varepsilon_{\vec{k}}\right)\psi(\vec{k}) \quad , \qquad \varepsilon_{\vec{k}} = \frac{\hbar^2 k^2}{2m} \tag{35}$$

where $\varepsilon_{\vec{k}}$ is the free electron energy. The total energy of a bound state of two electrons is smaller than their total free energy. We can define a modified wavefunction, such as

$$\Delta(\vec{k}) = (E - 2\,\varepsilon_{\vec{k}})\psi(\vec{k}) \tag{36}$$

$$\Delta(\vec{k}) = \int -\frac{d^3k'}{(2\pi)^3} \frac{V(\vec{k}-\vec{k}')}{\left(E - 2\varepsilon_{\vec{k}}\right)} \Delta(\vec{k}') \tag{37}$$

To define the potential, since we assume that the attractive interaction between electrons is mediated by phonons, we write

$$V(\vec{k}-\vec{k}') = \begin{cases} -V_0 & for \quad \varepsilon_{\vec{k}}, \varepsilon_{\vec{k}'} < \hbar\omega_D \\ 0 & otherwise \end{cases} \tag{38}$$

where ω_D is the Debye frequency for the crystal lattice. For a constant solution $\Delta(\vec{k}) = \Delta$, the solution will be an even spatial wavefunction, indicating a spin singlet (anti-parallel spins). To write the constant solution, we write the density of states per spin for an electron pair:

$$N(\varepsilon) = \frac{m^{3/2}}{\sqrt{2}\pi^2\hbar^3} \int_0^{\omega_D} \frac{\sqrt{\varepsilon}}{(2\varepsilon - E)}\, d\varepsilon \tag{39}$$

and for the solution, we have

$$\Delta = \frac{V_0 \Delta m^{3/2}}{\sqrt{2}\pi^2\hbar^3} \int_0^{\omega_D} \frac{\sqrt{\varepsilon}}{2\varepsilon - E}\, d\varepsilon \tag{40}$$

$$1 = \frac{V_0 m^{3/2}}{\sqrt{2}\pi^2\hbar^3} \left[\sqrt{\omega_D} - \sqrt{-\frac{E}{2}} \arctan\left(\frac{2\omega_D}{-E}\right) \right] \tag{41}$$

To obtain the minimum value of V_0, we take the limit

$$\lim_{E\to 0^-} V_0 = \frac{\sqrt{2}\pi^2\hbar^3}{\sqrt{\omega_D}m^{3/2}} \tag{42}$$

One fundamental fact is that the attractively interacting electrons are the ones near the Fermi level. Since $\varepsilon_F \gg \hbar\omega_D$, we can write

$$1 = \frac{V_0 m^{3/2}}{\sqrt{2}\pi^2\hbar^3}\left[\sqrt{\omega_D} - \sqrt{-\frac{E}{2}}\arctan\left(\frac{2\omega_D}{-E}\right)\right] \tag{43}$$

$$\Delta = V_0 N(\varepsilon_F)\Delta\int_{\varepsilon_F}^{\varepsilon_F+\hbar\omega_D}\frac{1}{2\varepsilon - E}\,d\varepsilon \tag{44}$$

$$\frac{2}{V_0 N(\varepsilon_F)} = ln\left[\frac{2(\varepsilon_F + \hbar\omega_D) - E}{2\varepsilon_F - E}\right] \tag{45}$$

In the case of $V_0 N(\varepsilon_F) \ll 1$, we can approximate $2(\varepsilon_F + \hbar\omega_D) - E \cong 2\hbar\omega_D$. Therefore, we have

$$E_B = 2\hbar\omega_D e^{-\frac{2}{V_0 N(\varepsilon_F)}} \tag{46}$$

which is the binding energy for two electrons inside the crystal lattice. These electron pairs are called *Cooper pairs*, which are the fundamental charge carriers of a superconductor. It was known that at low temperatures, the average kinetic energy of the electrons decreases, where electrons get more localized. With BCS theory, it is understood that the electron-phonon scattering also contributes to this localization, allowing the formation of Cooper pairs.

Now for a many-body system, first we define the pair amplitude function.

$$f_{\sigma,\sigma'}(\vec{r}) = \langle\psi_\sigma(\vec{r})\psi_{\sigma'}(\vec{r})\rangle \tag{47}$$

Then, we can define the electron-electron interactions with the effective Hamiltonian,

$$\begin{aligned} H = \sum_\sigma \int \left[\psi_\sigma^\dagger(\vec{r})H_0(\vec{r})\psi_\sigma(\vec{r})\right]d\vec{r} \\ + \sum_{\sigma,\sigma'}\int\left[\lambda_{\sigma,\sigma'}(\vec{r},\vec{r}')\psi_\sigma^\dagger(\vec{r})\psi_{\sigma'}^\dagger(\vec{r}')\psi_\sigma(\vec{r})\psi_{\sigma'}(\vec{r}')\right]d\vec{r}d\vec{r}' \end{aligned} \tag{48}$$

Where $\psi_\sigma^\dagger(\vec{r})$ and $\psi_\sigma(\vec{r})$ are creation and annihilation operators for electrons at position $\vec{r}$, $\lambda_{\sigma,\sigma'}(\vec{r},\vec{r}')$ is the spin coupling term for spin states σ, and H_0 is the Hamiltonian for a single electron,

$$H_0 = \frac{1}{2m}\left(-i\hbar\nabla - e\vec{A}\right)^2 + U(\vec{r}) - \mu \tag{49}$$

Now, if we consider a singlet coupling, such as

$$\lambda_{\sigma,\bar{\sigma}}(\vec{r},\vec{r}') = \lambda(\vec{r})\hat{\delta}(\vec{r}-\vec{r}') \qquad\qquad \lambda_{\sigma,\sigma}(\vec{r},\vec{r}') = 0 \tag{50}$$

where $\hat{\delta}(\vec{r}-\vec{r}')$ is an operator defining the fluctuations around the mean field and $\bar{\sigma}$ is the opposite spin state. We can write the interaction term in the effective Hamiltonian in terms of pair amplitudes, such as

$$\psi_{\bar{\sigma}}(\vec{r})\psi_\sigma(\vec{r}) = f(\vec{r}) + \hat{\delta}_{\bar{\sigma}\sigma}(\vec{r}) \tag{51}$$

where $\langle\hat{\delta}(\vec{r})\rangle = 0$. If the system is symmetric in terms of spin rotation, the effective Hamiltonian becomes:

$$\begin{aligned} H = \sum_\sigma \int \left[\psi_\sigma^\dagger(\vec{r})H_0(\vec{r})\psi_\sigma(\vec{r})\right]d\vec{r} \\ + \int \left[\Delta(\vec{r})^*\psi_\sigma(\vec{r})\psi_{\bar{\sigma}}(\vec{r}') + \Delta(\vec{r})\psi_\sigma^\dagger(\vec{r})\psi_{\bar{\sigma}}^\dagger(\vec{r}')\right]d\vec{r} \\ - \int \Delta(\vec{r})f^*(\vec{r})d\vec{r} \end{aligned} \tag{52}$$

The last integral is the energy difference between superconducting and normal states of matter. In order to diagonalize this Hamiltonian, we use a transformation developed by Nikolay Bogoliubov in 1958, called *Bogoliubov transformation* [29]

$$\psi_\uparrow(\vec{r}) = \sum_n \gamma_{n\uparrow}u_n(\vec{r}) - \gamma_{n\downarrow}^\dagger v_n^*(\vec{r}) \tag{53}$$

$$\psi_\downarrow(\vec{r}) = \sum_n \gamma_{n\downarrow}u_n(\vec{r}) - \gamma_{n\uparrow}^\dagger v(\vec{r}) \tag{54}$$

where $\gamma_{n\sigma}$ and $\gamma_{n\sigma}^{\dagger}$ are annihilation and creation operators for superconductive state. To find $u_n(\vec{r})$ and $v_n(\vec{r})$, considering the diagonalization requirement of the effective Hamiltonian, we write the *Bogoliubov-de Gennes equation.*

$$\begin{bmatrix} H_0(\vec{r}) & \Delta(\vec{r}) \\ \Delta^*(\vec{r}) & -H_0^{\dagger}(\vec{r}) \end{bmatrix} \begin{bmatrix} u_n(\vec{r}) \\ v_n(\vec{r}) \end{bmatrix} = E_n \begin{bmatrix} u_n(\vec{r}) \\ v_n(\vec{r}) \end{bmatrix} \tag{55}$$

The equation decouples when $\Delta(\vec{r}) = 0$, such as

$$H_0 u_n = E_n u_n \tag{56}$$

$$H_0^{\dagger} v_n = -E_n v_n \tag{57}$$

These equations correspond to Schrödinger's equation for electrons and holes. The pair potential $\Delta(\vec{r})$ is defined as

$$\Delta(\vec{r}) = \lambda(\vec{r}) \sum_n v_n^*(\vec{r}) u_n(\vec{r}) tanh(\frac{E_n}{2k_B T}) \tag{58}$$

which couples with the quasiparticle excitations. This pair potential is a self-consistency equation for the energy gap.

Now, if we express the density of states for such excitations:

$$N_S(E) = N_F \frac{|E|}{\sqrt{E^2 - |\Delta|^2}} \theta(|E| - |\Delta|) \tag{59}$$

where $|\Delta|$ is the energy gap of the superconductor. For energies much lower than the energy gap, none of the states are available for quasiparticle excitation, which points out that electrons and holes in the superconductor do not alter the superconducting behavior at low temperatures.

2.5. Josephson Effect and Superconductive Tunneling

One of the most important macroscopic quantum effects under the topic of superconductivity is the *Josephson effect*, which states that cooper pairs are allowed to tunnel from a weak link between two superconductors. It was predicted by Brian David Josephson in 1962 [30]

Starting with a phenomenological macroscopic approach, we consider two different superconducting electrodes with two different order parameters $\psi_A = \sqrt{n_A}e^{i\phi_A}$ and $\psi_B = \sqrt{n_A}e^{i\phi_B}$ separated by a weak link as illustrated below.

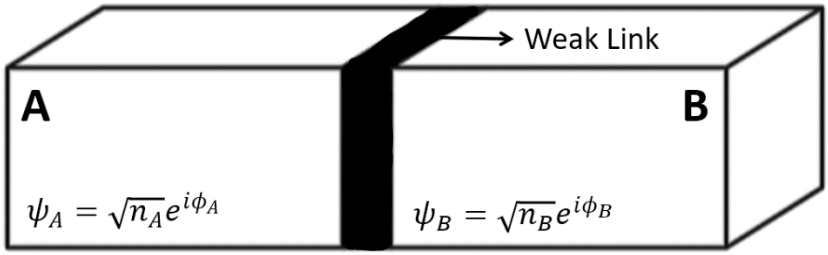

Figure 3. An illustration of two superconducting isles A and B separated by a weak link

Following the treatment of Richard P. Feynman for coupled quantum systems [31] we can write down the Schrödinger equation for the order parameters such as:

$$i\hbar\frac{\partial}{\partial t}\begin{bmatrix}\sqrt{n_A}e^{i\phi_A}\\ \sqrt{n_B}e^{i\phi_B}\end{bmatrix} = \begin{bmatrix}eV & K\\ K & -eV\end{bmatrix}\begin{bmatrix}\sqrt{n_A}e^{i\phi_A}\\ \sqrt{n_B}e^{i\phi_B}\end{bmatrix} \tag{60}$$

Now, if we write down the time derivatives of the order parameters, we have:

$$\dot{\psi}_A = \dot{n}_A\frac{1}{2\sqrt{n_A}}e^{i\phi_A} + \dot{\phi}_A i\sqrt{n_A}e^{i\phi_A} = \frac{eV}{i\hbar}\sqrt{n_A}e^{i\phi_A} - \frac{K}{i\hbar}\sqrt{n_B}e^{i\phi_B} \tag{61}$$

$$\dot{\psi}_B = \dot{n}_B\frac{1}{2\sqrt{n_B}}e^{i\phi_B} + \dot{\phi}_B i\sqrt{n_B}e^{i\phi_B} = -\frac{eV}{i\hbar}\sqrt{n_B}e^{i\phi_B} - \frac{K}{i\hbar}\sqrt{n_A}e^{i\phi_A} \tag{62}$$

To decouple the time derivatives of charge densities, we multiply the equations by $e^{-i\phi_A}$ and $e^{-i\phi_B}$ and separate the real and imaginary parts, and defining the phase difference between the order parameters, we have

$$\dot{n}_A = -2K\sqrt{n_A n_B}sin\phi \tag{63}$$

$$\dot{n}_B = 2K\sqrt{n_A n_B}sin\phi \tag{64}$$

for the real part, where $\phi = \phi_B - \phi_A$ is the *Josephson phase*. This implies the formation of a supercurrent through the junction due to the phase difference of two superconductors. If we write down the supercurrent equation, we have

$$J = J_C sin\phi \tag{65}$$

where J_C is the critical current density. For a junction with cross section area A, we have $I = J/A$, therefore the current across the junction is given as

$$I = I_C sin\phi \tag{66}$$

which is known as the *DC Josephson relation*. It shows that without a potential difference across the junction, there still exists a current tunneling through the junction due to the phase difference between two superconductors. The junction can carry a current up to a critical current I_C without energy dissipation. If the current exceeds I_C, energy dissipation starts where a potential difference is observed across the junction. This form of the current-phase relation is valid for high temperatures close to the critical temperature.

Following the derivation, we can write down the imaginary part as

$$\dot{\phi}_A = -\frac{eV}{\hbar} + K\sqrt{\frac{n_2}{n_1}}cos\phi \tag{67}$$

$$\dot{\phi}_B = \frac{eV}{\hbar} + K\sqrt{\frac{n_1}{n_2}}cos\phi \tag{68}$$

If we use similar superconducting isles where $n_A \approx n_B$, we obtain:

$$\dot{\phi} = \frac{2eV}{\hbar} \tag{69}$$

For a constant voltage, we can use direct integration, which yields:

$$\phi = \phi(0) + \frac{2eVt}{\hbar} \tag{69}$$

Now, the current-phase relation can be written as:

$$I = I_C sin\left(\phi(0) + \frac{2eVt}{\hbar}\right) \tag{70}$$

This relation implies that a current formed by a potential difference across the junction will oscillate over time, which is known as *AC Josephson relation.*

There are other parameters worth mentioning, such as the *Josephson energy* and *Josephson inductance,*

$$E_J = \frac{\Phi_0 I_C}{2\pi} \tag{71}$$

$$L_J = \frac{\Phi_0}{2\pi I_C} \tag{72}$$

where Φ_0 is the magnetic flux quantum, which was previously given in equation (29).

First observation of the Josephson tunneling effect was reported by P. W. Anderson and J. M. Rowell in 1963. [32]

2.6. Microscopic Nature of Tunneling

In the proximity of a normal metal (N) and a superconductor (S) intersection, when an electron in a normal metal with energy lower than the gap energy of the superconductor

hits the interface, it cannot penetrate the superconductor since there are no states to occupy below the gap energy in the superconductor. Therefore, the electron either scatters from the interface or reflects as a hole from the interface, and by charge conservation creating a Cooper pair inside the superconductor. This reflection phenomenon is known as *Andreev reflection* (AR). [33] If we solve the Bogoliubov-de Gennes equation (55) for such a configuration, and simplifying the problem by making the assumption of a constant gap energy inside the superconductor, we have:

$$\psi_N = \begin{bmatrix}1\\0\end{bmatrix} e^{ik_N^+ x} + r_{e-e}\begin{bmatrix}1\\0\end{bmatrix} e^{-ik_N^+ x} + r_{e-h}\begin{bmatrix}0\\1\end{bmatrix} e^{ik_N^- x} \tag{73}$$

$$\psi_S = t_+ \begin{bmatrix}u_0 e^{i\phi_S}\\ v_0\end{bmatrix} e^{ik_S^+ x} + t_- \begin{bmatrix}v_0 e^{i\phi_S}\\ u_0\end{bmatrix} e^{-ik_N^+ x} \tag{74}$$

$$\psi = \psi_N + \psi_S \tag{75}$$

For the normal metal wavefunction, the first term represents an incoming electron to the interface, the second term represents an electron reflected from the interface and the third term represents a hole reflected from an incoming electron via AR. If we disregard the scattering of the electrons due to the geometrical imperfections and impurities, we can assume that at the interface the total wavefunction must be continuous and differentiable. For the energies below the gap energy, the transmission and reflection probabilities are:

$$r_{e-e} = t_+ = t_- = 0 \tag{76}$$

$$|r_{e-h}|^2 = 1 \tag{77}$$

Therefore, Andreev reflection is the only possible process if the quasiparticles are below the gap energy for a perfect interface. Due to this effect, the cooper pairs can exist in the vicinity of the S/N interface and in the close proximity of the normal metal. This phenomenon is known as the *proximity effect.*

Now, if we consider a weak link between two superconductors A and B, quasiparticles may reflect back and forth between two superconducting interfaces and changing from

electrons to holes and from holes to electrons consecutively at each reflection as shown in Figure 4.

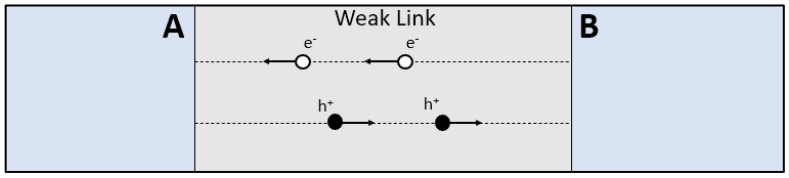

Figure 4. Simple illustration of consequent Andreev reflections between superconductors A and B

Assuming that the weak link is short enough so that we can ignore the dynamical phase due to the translation, if we define the phases for the reflections, we have

$$\theta_{e-h} = -arccos\left(\frac{E}{\Delta}\right) + \phi_A \tag{78}$$

$$\theta_{h-e} = -arccos\left(\frac{E}{\Delta}\right) - \phi_B \tag{79}$$

with the total phase

$$\theta = -2arccos\left(\frac{E}{\Delta}\right) + \phi \tag{80}$$

where $\phi = \phi_A - \phi_B$ is the phase difference between two superconductors. These reflections may lead to a bound state if:

$$\theta = 2\pi n \qquad n = 1,2, \ldots \tag{81}$$

In this case, the bound state energies are given as:

$$E_{\pm}^{ABS} = \pm cos\left(\frac{\Delta\phi}{2}\right) \tag{82}$$

These states are called *Andreev bound states* (ABS), which carry supercurrent from one superconducting isle to another across the tunneling barrier with each cycle of reflection, which is a microscopic explanation for the Josephson effect with normal

metal weak links. Therefore, it can be regarded as the governing mechanism of Cooper pair tunneling over a weak link. ABS defines the characteristics of the weak link between the superconductors. It is possible to observe ABS in ferromagnetic proximities. [34,35] Also in hybrid superconductor – semiconductor links, emergence of Majorana bound states evolving from ABS are reported. [36]

If we continue the subject at hand, for each bound state, we can write the carried amount of current as

$$I_S = \frac{e\Delta^2 \tau sin(\phi)}{2\hbar E_+^{ABS}} tanh\left[\frac{E_+^{ABS}}{2k_B T}\right] \tag{83}$$

where τ is the transmission probability. For the temperatures below and close to the critical temperature, $E_+^{ABS} \approx \Delta$, if we add together all the transmission probabilities, we obtain the supercurrent equation

$$I = \frac{\pi\Delta sin(\phi)}{2eR_N} tanh\left[\frac{\Delta}{2k_B T}\right] \tag{84}$$

which is known as *Ambegaokar-Baratoff relation* (AB relation). It was proposed by Vinay Ambegaokar and Alexis Baratoff in 1963[37]

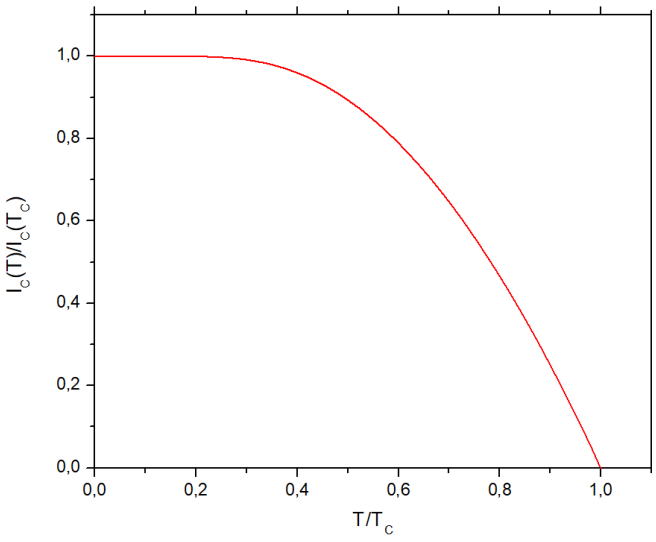

Figure 5. AB relation normalized with critical temperature

If we combine this relation with DC Josephson relation, we have

$$I_C(T) = \frac{\pi\Delta}{2eR_N} tanh\left[\frac{\Delta}{2k_BT}\right] \quad (85)$$

which is a relationship between the critical current, gap energy and temperature of a junction.

2.7. Stewart – McCumber Model

In the previous subsection 1.1.5, it is mentioned that a Josephson junction shows resistance if the critical current is exceeded in a junction. Also, due to the separation of two superconducting isles carrying charges, there is a capacitance forming in the junction. It is possible to model a realistic Josephson junction by defining an ideal Josephson junction shunted with a hypothetical resistor and a capacitor, as illustrated in Fig 6. This model is known as resistively and capacitively shunted junction (RCSJ) model or *Stewart-McCumber model*. [38]

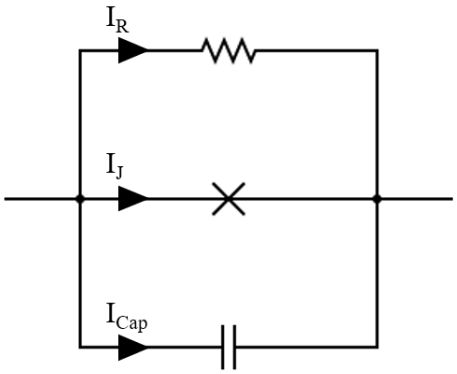

Figure 6. RCSJ circuit diagram with an ideal Josephson junction in the middle shunted with a resistor and a capacitor

We can write the total current across the RCSJ circuit as

$$I = I_J + I_R + I_{Cap} \quad (86)$$

The current branches to the resistor, the Josephson junction, and the capacitor. For the resistor branch, the current is given as:

$$I_R = \frac{V}{R} \tag{87}$$

If we use the AC Josephson relation in the form of equation (69) for the voltage, we have:

$$I_R = \frac{\hbar}{2e}\frac{\dot{\phi}}{R} \tag{88}$$

For the capacitor branch, the current is given as

$$I_{Cap} = \dot{q} = C\dot{V} \tag{89}$$

and the capacitance of the junction is given as

$$C = \frac{\epsilon A}{d} \tag{90}$$

where ϵ is the electric permittivity of the weak link, A is the tunneling area of the junction and d is the length of the tunneling layer.

If we again use the AC Josephson relation, we have:

$$I_{Cap} = C\frac{\hbar}{2e}\ddot{\phi} \tag{91}$$

For the junction branch, we can use the DC Josephson relation to obtain the current. Therefore, the total current is expressed as

$$I = I_C sin\phi + \frac{\hbar}{2e}\frac{\dot{\phi}}{R} + C\frac{\hbar}{2e}\ddot{\phi} \tag{92}$$

If we rewrite the current equation in terms of magnetic flux quanta and divide both sides by the critical current, we have:

$$\frac{I}{I_C} = sin\phi + \frac{\Phi_0}{2\pi}\frac{\dot{\phi}}{R} + C\frac{\Phi_0}{2\pi}\ddot{\phi} \tag{93}$$

Defining RC time constant and Josephson time constant,

$$\tau_{RC} = RC \qquad \tau_J = \frac{L_J}{R} = \frac{\Phi_0}{2\pi I_C R} \qquad \tilde{\tau} = \frac{t}{\tau_J} \tag{94}$$

Now, we can normalize the current equation by replacing the partial time derivatives with $\frac{\partial}{\partial\tilde{\tau}}$, which yields:

$$\frac{I}{I_C} = sin\phi + \frac{\partial\phi}{\partial\tilde{\tau}} + \beta_c\frac{\partial^2\phi}{\partial\tilde{\tau}^2} \tag{95}$$

The coefficient in the third term at the right hand side of the equation is known as *Stewart McCumber parameter*:

$$\beta_c = \frac{\tau_{RC}}{\tau_J} = \frac{2\pi I_C R^2}{\Phi_0} \tag{96}$$

From this point of view, the damping behavior of a real junction can be categorized into two: overdamped and underdamped behavior. This parameter is a measuring stick for the damping behavior of the junction where for $\beta_c < 1$ the junction shows overdamped behavior and for $\beta_c > 1$ it shows underdamped behavior. It is not possible to extract much information from an overdamped junction, the jump to the finite voltage state may occur below the critical current. For the underdamped junctions, the current-voltage characteristics are hysteretic; junction carries supercurrent without energy dissipation up until the critical current, switching to the finite voltage state with a normal state resistance R_N at the critical current, where the corresponding voltage is defined as:

$$V_g \approx \frac{2\Delta}{e} \tag{97}$$

Now, if the current starts to decrease after switching to the resistive state, the junction will enter the superconductive state at a current I_R which is smaller than the critical current, creating a hysteresis.

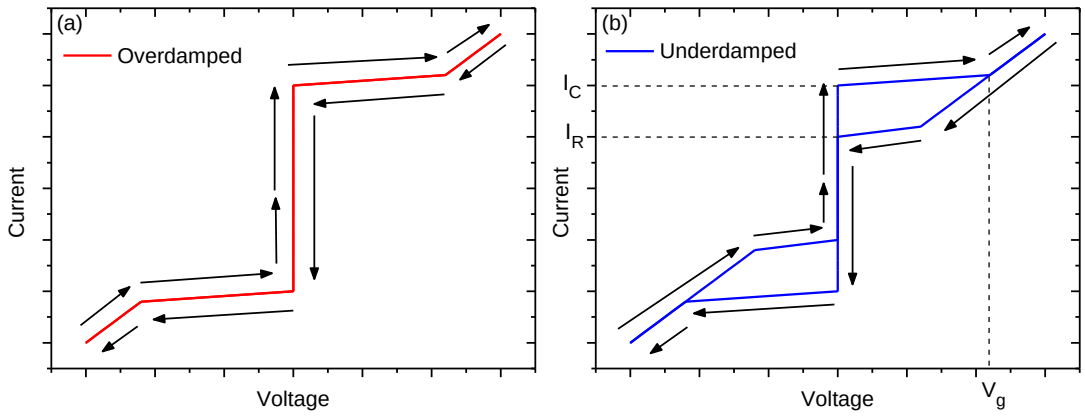

Figure 7. Plots for I-V characteristics of (a) overdamped and (b) underdamped Josephson junctions

This model for the current is analogous for a mechanical system. If we consider a system where a particle with mass $\left(\frac{\hbar}{2e}\right)^2 C$ moving at the phase ϕ with an effective potential

$$U(\phi) = -E_J cos\phi - (I\frac{\hbar}{2e})\phi \tag{98}$$

which is known as the *washboard potential*. At zero current, the "particle" is confined inside the potential well, where the wells are defined by the cosine function and the height of the well is scaled by the Josephson energy:

$$\Delta U = \frac{8\sqrt{2}}{3} E_J \left(1 - \frac{I}{I_C}\right)^{3/2} \tag{99}$$

With increasing current, the washboard potential gets tilted and ultimately the particle slips down from the edge of the extremum points when the critical current is exceeded. An illustration for the mechanical analogy is illustrated in Figure 8.

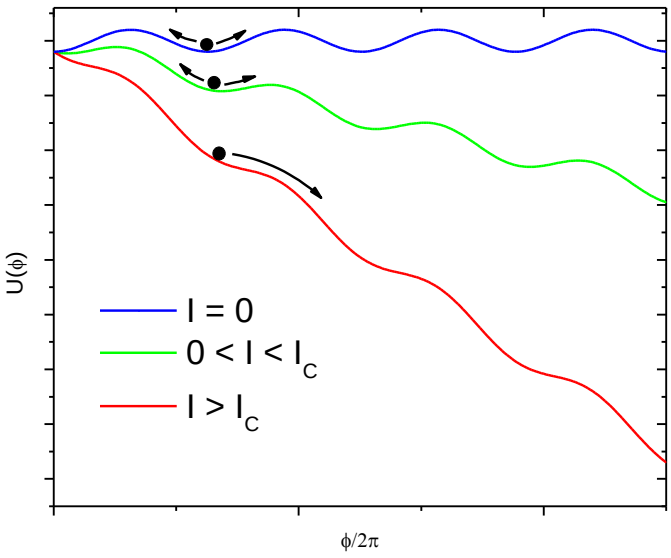

Figure 8. Washboard potentials for I = 0, 0 < I < I_C, and I > I_C.

The particle is trapped in one of the anharmonic potential wells in the washboard potential for the cases I = 0 and 0 < I < I_C since local minimum points exists, which is the zero voltage state for the junction. However, it will not be trapped in the case I > I_C because there are only saddle points on the potential, which is the finite voltage state of the junction. For the underdamped junction, the hysteretic behavior can be expressed within this analogy; after exceeding the critical current, the particle does not immediately get re-trapped in the next well but keeps slipping down until it is re-trapped in a lower potential well. By using the RCSJ model, it is possible to extract important parameters in order to investigate the behavior of a Josephson junction.

2.8. Josephson Junction in a Magnetic Field

In the previous subsections 1.1.2 and 1.1.3, the effects of applied magnetic field on a superconductor is discussed where the diamagnetic behavior of the superconducting condensate, destruction of the superconducting state at a critical magnetic field with a

defined penetration length, and the quantization of magnetic field inside a superconducting loop are mentioned. Now, if we consider a Josephson junction with superconducting isles A and B under a perpendicular magnetic field with respect to the tunneling axis, the effective magnetic thickness is

$$d_{eff} = d_t + \lambda_A tanh\frac{l_A}{\lambda_A} + \lambda_B tanh\frac{l_B}{\lambda_B} \tag{100}$$

where λ_A and λ_B are London penetration depths for superconductors A and B, l_A and l_B are the lengths of the superconductors, d_t is the thickness of the tunneling barrier and d_w is the width of the junction, as shown in Figure 9.

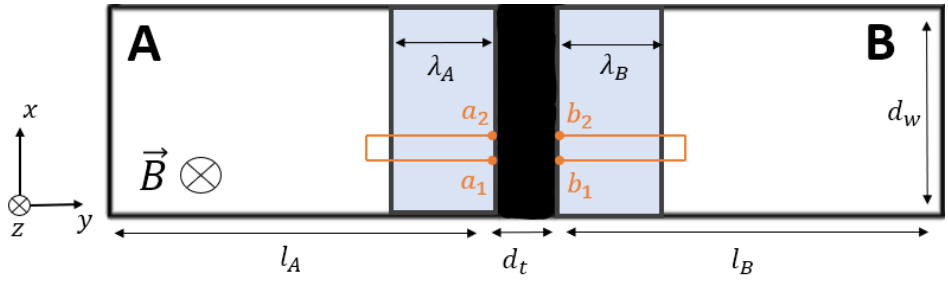

Figure 9. Illustration of a Josephson junction under magnetic field $\vec{B}$ perpendicular to the tunneling axis

If we assume that A and B are same superconducting materials where $\lambda_A = \lambda_B = \lambda_L$ with the same lengths $l_A = l_B \gg \lambda_L$, then the effective magnetic thickness can be approximated as

$$d_{eff} \approx d_t + 2\lambda_L \tag{101}$$

Now, we can write the Josephson phase as:

$$\phi = \phi_A - \phi_B - \frac{2\pi}{\Phi_0}\int_{a_1}^{a_2} \vec{A}\cdot d\vec{l} \tag{102}$$

where $\vec{A}$ is the vector potential. In terms of vector potential, we can define the magnetic field as:

$$\vec{B} = \vec{\nabla} \times \vec{A} \tag{103}$$

If we use the supercurrent equation (21) that we obtained from Ginzburg-Landau theory, we can write down the phase gradient in terms of current density and vector potential as:

$$\vec{\nabla}\phi = \frac{2\pi\lambda_L^2\mu_0}{\Phi_0}\vec{J} + \frac{2\pi}{\Phi_0}\vec{A} \tag{104}$$

where μ_0 is the permeability of the free space. Now, if we integrate the phase gradient over the paths on two superconductors, we have:

$$\phi(a_1) - \phi(a_2) = \frac{2\pi}{\Phi_0}\lambda_L^2\mu_0\int_{a_2}^{a_1}\vec{J}\cdot d\vec{l} + \frac{2\pi}{\Phi_0}\int_{a_2}^{a_1}\vec{A}\cdot d\vec{l} \tag{105}$$

$$\phi(b_2) - \phi(b_1) = \frac{2\pi}{\Phi_0}\lambda_L^2\mu_0\int_{b_1}^{b_2}\vec{J}\cdot d\vec{l} + \frac{2\pi}{\Phi_0}\int_{b_1}^{b_2}\vec{A}\cdot d\vec{l} \tag{106}$$

If we sum them up, we have:

$$\begin{aligned}\phi(a_1) - \phi(a_2) + \phi(b_2) - \phi(b_1) \\ = \frac{2\pi}{\Phi_0}\lambda_L^2\mu_0\int_{a_2}^{a_1}\vec{J}\cdot d\vec{l} + \frac{2\pi}{\Phi_0}\int_{a_2}^{a_1}\vec{A}\cdot d\vec{l} + \frac{2\pi}{\Phi_0}\lambda_L^2\mu_0 \\ + \frac{2\pi}{\Phi_0}\int_{b_1}^{b_2}\vec{A}\cdot d\vec{l}\end{aligned} \tag{107}$$

If we add the following integrals to both sides of the equation;

$$\frac{2\pi}{\Phi_0}\int_{a_1}^{b_1}\vec{A}\cdot d\vec{l} + \frac{2\pi}{\Phi_0}\int_{a_2}^{b_2}\vec{A}\cdot d\vec{l} \tag{108}$$

The LHS becomes:

$$\left[\phi(b_2) - \phi(a_2) - \frac{2\pi}{\Phi_0}\int_{a_2}^{b_2}\vec{A}\cdot d\vec{l}\right] - \left[\phi(b_1) - \phi(a_1) - \frac{2\pi}{\Phi_0}\int_{a_1}^{b_1}\vec{A}\cdot d\vec{l}\right] \tag{109}$$

And the RHS becomes:

$$\frac{2\pi}{\Phi_0}\oint \vec{A}\cdot d\vec{l} + \frac{2\pi\lambda_L^2\mu_0}{\Phi_0}\left[\int_{a_2}^{a_1}\vec{J}\cdot d\vec{l} + \frac{2\pi}{\Phi_0}\int_{b_1}^{b_2}\vec{J}\cdot d\vec{l}\right] \tag{110}$$

where the last term is equal to zero for thick electrodes. Defining the flux through the path as

$$\Phi = Bd_{eff}dx = \oint \vec{A}\cdot d\vec{l} \tag{111}$$

and the complete equation can be expressed as:

$$\frac{\partial\phi}{\partial x} = \frac{2\pi}{\Phi_0}Bd_{eff} \tag{112}$$

which indicates that the applied magnetic field generates a phase gradient over the junction width.

If we define the characteristic length for the junction, the *Josephson length* is given as:

$$\lambda_J = \sqrt{\frac{\Phi_0}{2\pi\mu_0 d_{eff}J_C}} \tag{113}$$

For a short Josephson junction where $d_w \leq 4\lambda_J$, the magnetic flux in the Josephson junction which is referred as Josephson flux, and the position dependent phase can be written as:

$$\Phi_J = Bd_{eff}d_w \tag{114}$$

$$\phi(x) = \phi + \frac{2\pi Bd_{eff}}{\Phi_0}x \tag{115}$$

By using the DC Josephson relation in the form of equation (66), we can write a relationship for the total critical current with respect to the magnetic flux as

$$I_C(\Phi_J) = I_C \left| \frac{sin\pi \frac{\Phi_J}{\Phi_0}}{\pi \frac{\Phi_J}{\Phi_0}} \right| \tag{116}$$

which is known as the *Fraunhofer diffraction relation*. If we plot this function in terms of applied magnetic field as illustrated in Figure 1, we will see an interference pattern of the critical current.

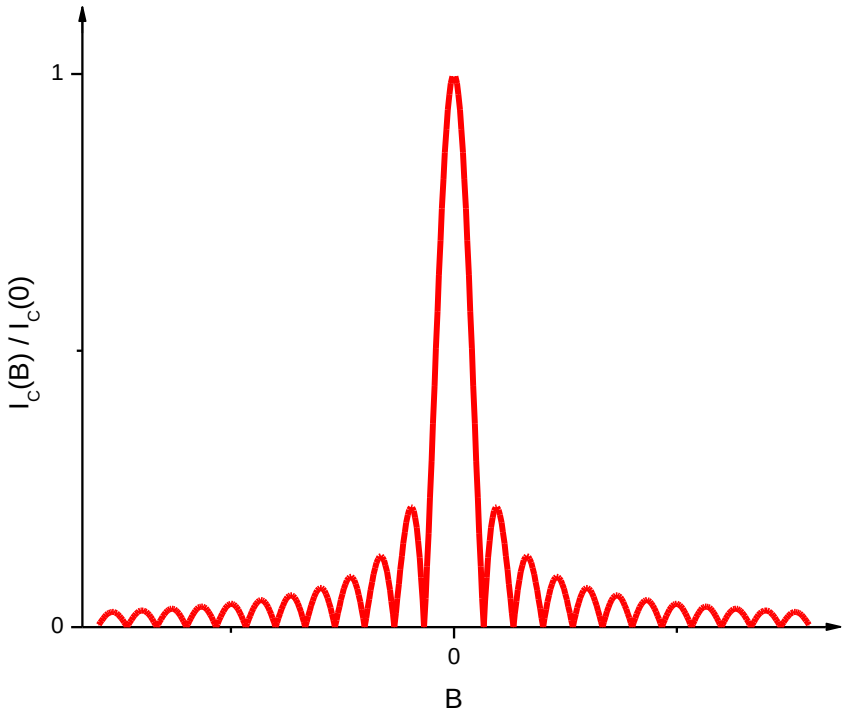

Figure 10. Fraunhofer pattern for a conventional Josephson junction

This behavior of the critical current with respect to the magnetic flux is analogous to the single slit diffraction experiment where a modulation is observed on the intensity of light on a screen passing through a single slit. By this relation, it is possible to screen the effects of the external magnetic field through the critical supercurrent.

2.9. Ferromagnetic Josephson Junction

As discussed in subsection 1.1.4. BCS theory allows the formation of electron pairs in terms of spin singlets and triplets. However, for the superconductor – ferromagnet interfaces, the superconductivity is suppressed from the spin magnetization $|\vec{m}_s|$ due to the magnetic effects. The difference in energy between two spin orientations in the Cooper pair results the order parameter $\Delta(x)e^{i\phi(x)}$ to oscillate and decay in the ferromagnetic region.

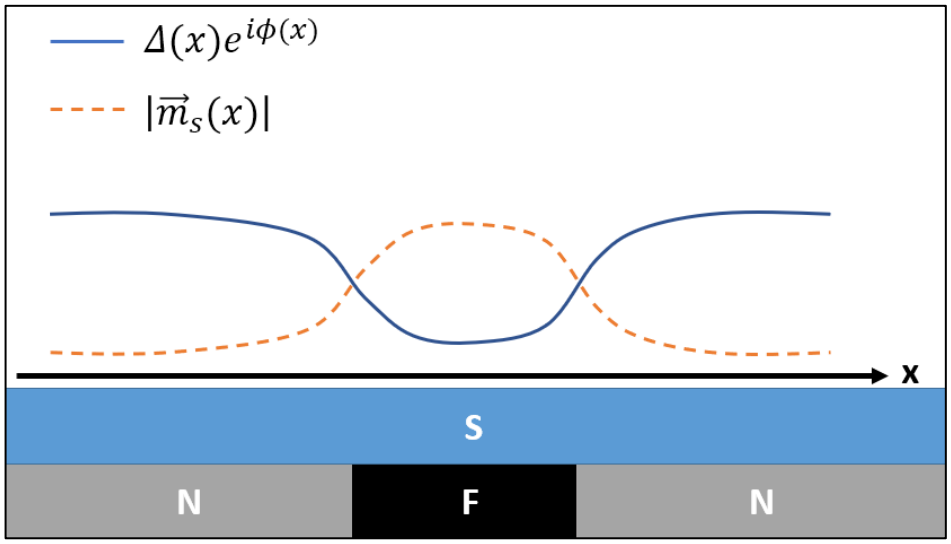

Figure 11. The effect of ferromagnetic coupling to the superconducting order parameter

In the diffusive limit and above, where the length of the interface is smaller than the electron-phonon and electron-electron interaction distance, the interaction with the exchange field originated from the ferromagnetic domains leads to the breaking of Cooper pairs. By nature, singlet pairing is mostly destroyed in s-wave superconductors, while triplet pairing is allowed in various configurations and reported in SF interfaces and ferromagnetic weak links. [7,39–42] This interaction behavior raises the possibility to realize so called π-junctions, where a negative Josephson coupling is observed due to the shift in the ground state of the Josephson phase by an amount of π. [43]

2.10. Properties of Ferrimagnetic Iron Oxide Compounds

Magnetite (γ-Fe_3O_4) is an iron oxide compound like haematite (α-Fe_2O_3) and wüstite (FeO) and it is one of the oldest magnetic materials known in history. It is one of the first crystal structures solved by Lawrence Bragg in 1915.[44] It contains divalent and trivalent iron valences within a stoichiometry Fe^{+2}/Fe^{+3} of ½ fraction. It has an inverse-spinel face-centered cubic crystal structure with space group O_h^7 (Fd3m), which consists of 32 oxygen ions. Fe^{+2} ions and half of the Fe^{+3} ions occupy octahedral sites and rest of the Fe^{+3} ions occupy tetrahedral sites. It has a lattice constant of a = 8.367 Å. A ball and stick representation of magnetite lattice is given in Figure 12.

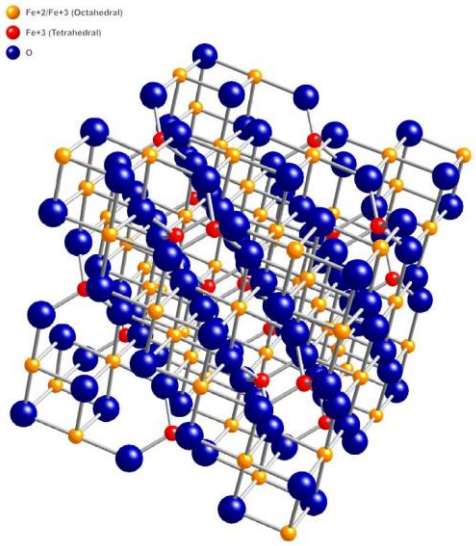

Figure 12. Inverse-spinel cubic crystal structure of magnetite

Maghemite (γ-Fe_2O_3) is another phase of iron oxide, which is different from magnetite in terms of iron-oxygen stoichiometry, but similar to magnetite in terms of crystal morphology. It also has an inverse-spinel FCC structure; however, it has got iron vacancies mostly in the octahedral sites. Due to the similarities in the alignment of crystals in magnetite and maghemite lattices, it is challenging to distinguish their structures with conventional X-ray diffraction techniques.[45]

Both magnetite and maghemite are ferrimagnets, where the theory of ferrimagnetism is developed by Néel having magnetite as its main example in 1948.[46] Ferrimagnetism is a state of matter closely related with ferromagnetism, where different magnetic moments

align opposite to each other similar to antiferromagnets, but due to the difference in magnitude, a spontaneous magnetic moment remains in the material. Néel proposed that for magnetite, trivalent iron is antiferromagnetically aligned in the tetrahedral and octahedral sublattices, therefore after they cancel out the only magnetic contribution is due to the divalent iron in the octahedral sites.[46]

The concept of magnetic anisotropy leads to a concept of magnetization axes inside a material, where for magnetite, a triaxial magnetic anisotropy with a single easy axis towards <111> direction, a single hard axis towards <100> direction, and an intermediate axis towards <110> direction, respectively. There are different types of magnetic anisotropy, depending on the crystallography, shape, elasticity and stress, and homogeneous / heterogeneous impurities.

In room temperature, magnetite behaves as a poor conductor where the conductivity is related with the electron relaxation time of the electron exchange between divalent and trivalent iron atoms in the octahedral lattice sites by the Stokes-Einstein relation,

$$\sigma = \frac{ne^2a^2}{k_BT\tau}$$

where n is the charge carrier concentration, a is the distance between octahedral sites, $k_BT$is the thermal energy, τ is the relaxation time and σ is the conductivity. This electron exchange phenomenon is also known as “electron hopping”. [47]

Maghemite on the other hand is a semiconductor material at room temperature with a spin dependent bandgap energy of 2 eV. [48]

It is known that variations in oxygen stoichiometry of iron oxides causes a change in electrical and magnetic responses. The half metallic and insulating characteristics of magnetite and hematite at room temperature is an example. In band theory, the presence of down spin electrons at the Fermi level is an implication of the half metallic behavior of magnetite.[49] Another one is the difference in the magnetic response of hematite and magnetite. Usually, in literature α-Fe_2O3 and γ-Fe_2O_3 are known as a ferrimagnetic insulator and an antiferromagnetic insulator respectively.

The magnetic and electrical behaviors of magnetite are altered by a temperature dependent transition, occurring at around 120 K due to a structural change of the lattice

structure from inverse spinel cubic to normal spinel monoclinic structure with a slight distortion in the crystal lattice, which is known as Verwey transition. It was discovered by Evert Verwey in 1939 and it is the first observed metal-insulator transition.[50] The resistivity increases in few orders of magnitude and the magnetization behavior is suppressed below the transition temperature T_v. The structure change from inverse spinel to normal spinel, trivalent iron occupies the octahedral site, which eliminates the electron hopping and resulting in an increase in the resistance. This valence change in the octahedral site also changes the ferrimagnetic behavior. Furthermore, the distortion in the crystal lattice from cubic to monoclinic structure leads to a deviation in the easy and hard axes of magnetite at the transition temperature, which can be observed with changing temperature under the effect of a uniform magnetic field. These strong and distinguishing characteristics of magnetite makes it a candidate in various applications.

3. EXPERIMENT

In this section, experimental process in the deposition of niobium (Nb) and iron oxide (Fe-O) thin films, all techniques for their structural electrical and magnetic analyses, design and every fabrication step of coplanar Josephson junctions were described. Additionally, details of measurements techniques used for magnetic and electrical behaviors of the coplanar Josephson junction are given.

3.1. Thin Film Deposition by Magnetron Sputtering Technique

In the thin film technology, there are various deposition techniques, mainly categorized as physical vapor deposition (PVD) and chemical vapor deposition (CVD) , where there are many other methods to grow thin films on different substrates.[51,52] In this work, PVD methods are used for crystal growth and material deposition, such as magnetron sputtering and evaporation.

Magnetron sputtering is a physical vapor deposition technique which utilizes highenergy plasma under vacuum to remove atoms/molecules from a target material, where they are deposited on a substrate. This technique enables to deposit almost all materials and offers good adhesion, high and conformal step coverage, and tunable deposition rates down to roughly atomic layer per second.

In order to obtain plasma with low working pressures in a sputtering system, first a precursor gas with a controlled flow is inserted inside the deposition chamber kept in high vacuum ($<10^{-8}$ mTorr) and followed by ionization of the sputtering gas by DC or RF power applied to a magnetron gun. Usually, argon gas is used as a precursor sputtering gas because it is chemically inert and heavy enough to eject the target atoms. By tuning the generated plasma, coating material is removed from the surface of the

target and deposited on a substrate at a desired thickness. For the film deposition by reactive sputtering, non-inert gasses such as oxygen and nitrogen are used as a precursor gas.[53] By adjusting the partial pressures on the flow of a reactive gas, it is possible to tune the stoichiometry of a material. A simple diagram of the sputtering process is schematically illustrated below

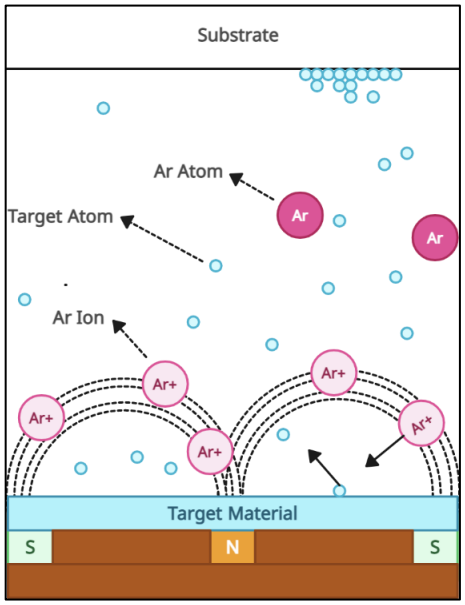

Figure 13. Non-reactive magnetron sputtering process

A typical sputtering system consists of a vacuum chamber, a sample stage, a power source (DC or RF) connected to a magnetron gun where the target material is loaded, and gas inlets with pressure and mass flow regulation. For various purposes, it is possible to customize a sputtering device with many additional different equipment, such as a heater or a sample rotator.

Base pressure, working pressure, precursor mass flow rate, bias power and temperature are the most important parameters of sputtering process. These parameters ultimately affect the deposited film quality through generated stress, crystallinity, electronical configuration, and morphology of the deposited thin film.

In this thesis, Nb film growth experiments were carried out in two sputtering systems, while Fe-O films were deposited in the AJA sputtering system. The specifications of two film deposition systems are described in the following sections. %99.999 purity Nb, Au and Fe3O4 sputtering targets used in this experiment are purchased from Kurt Lesker company from the project budget.

3.1.1. NanoVak and AJA Phase II J Magnetron Sputtering Systems

For the growth optimization of niobium thin films, NanoVak magnetron sputtering system is used, which is located in Sabancı University Nanotechnology Research and Application Center (SUNUM). The sputtering device consists of a vacuum chamber, 2 DC and 1 RF magnetron guns for targets, a sample stage with a rotator, and a heater which reaches up to 450 ^{O}C.

Figure 14. NanoVak NVSP-400 magnetron sputtering system

It was not possible to optimize the growth of magnetite thin films on this system since the substrate heating option does not allow us to increase the in-situ film growth temperature beyond 400°C. Initially, NanoVak sputter was preferred for Nb film deposition. However, Nb-O was observed in as-grown films due to outgassing from the chamber walls and low pumping power of the system.

Mostly AJA Phase II J magnetron sputtering system was used for the growth optimization of magnetite and niobium thin films, and fabrication of Josephson junctions. The AJA sputtering system is located in Boğaziçi University, and it is used by the research group BUSPIN.

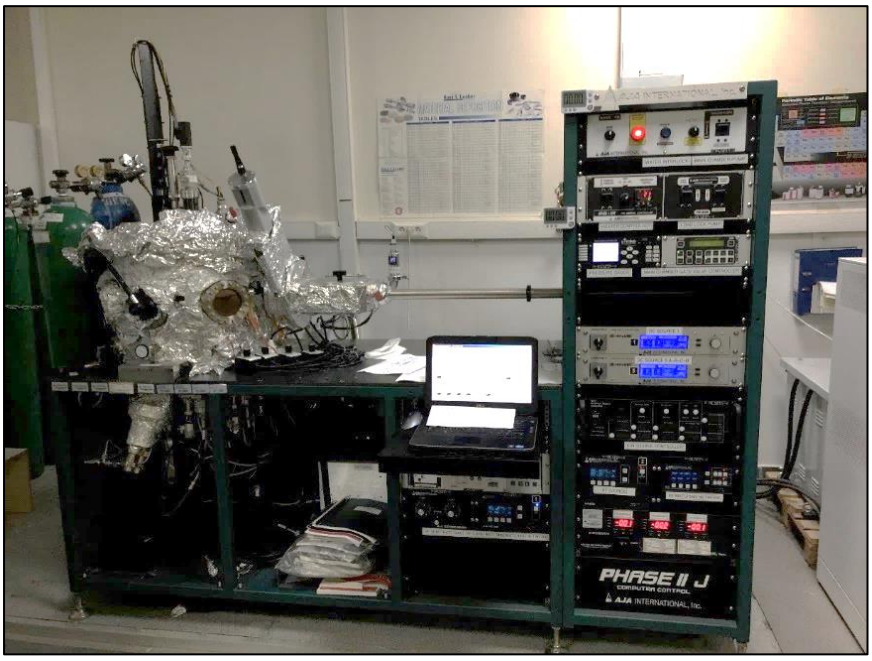

Figure 15. AJA Phase II J magnetron sputtering system.

The system consists of a main vacuum chamber which contains 8 guns and an ion milling gun, a load-lock system, a sample heater which reaches up to 850 ^{O}C, and two different sample stage options (magnetic and non-magnetic) which allows substrate voltage biasing and rotating. A simplified diagram for the AJA sputtering system is presented in Figure 16.

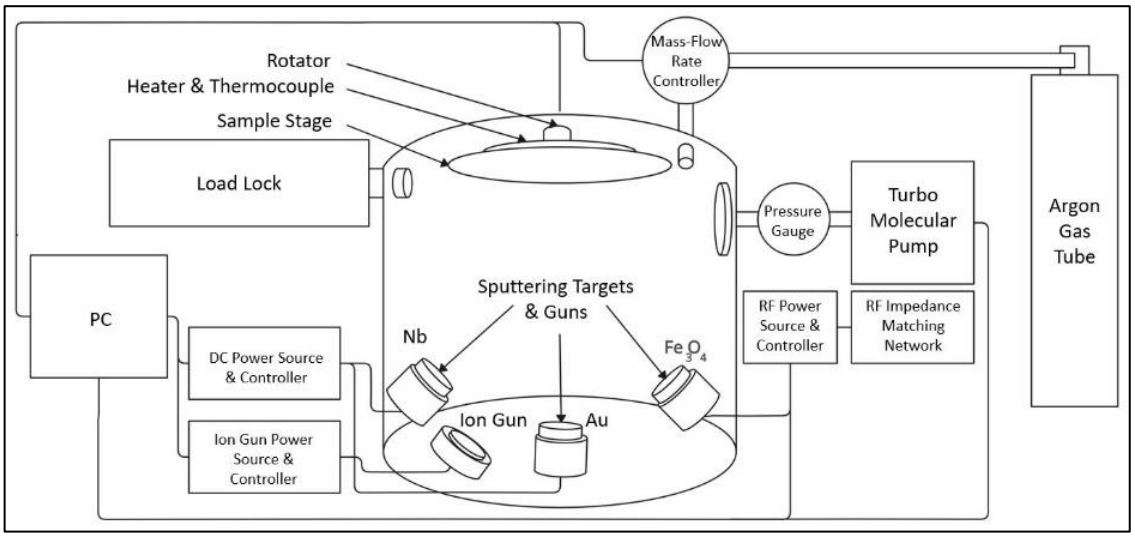

Figure 16. Simplified diagram of AJA Phase II J sputtering system for the used components

The sputtering system is maintained periodically by regular target-change procedures by BUSPIN research group and before each target-change procedure, the stainless-steel components of the target guns are decontaminated by using sand-milling followed by solvent ultrasound cleaning. After integrating the clean parts and the target material with the system, the deposition chamber is vacuumed and baked at 160 ^{O}C for around 48 hours in order to decontaminate the excess oxygen inside the chamber. After baking, the base pressure of the main chamber reaches down to ~10^{-9} Torr, which is suitable for high quality thin-film deposition.

3.1.2. Substrate Preparation

For niobium thin film deposition, single crystal MgO (010) and Al2O3 (0001) substrates with size of 1 × 1 cm^2 are provided from Crystal GmbH company. For magnetite deposition, only MgO substrates are used. In addition, for VSM measurements 2 mm × 5 mm samples are diced with the scriber from pristine MgO substrates. Before deposition, substrates are washed-out in using an ultrasonic bath sequentially in acetone, isopropanol, and ethanol for 5 minutes at each process and then dried by nitrogen blow.

Thin film deposition is carried out after the cleaning process.

3.1.3. Growth Rate Calibration in AJA and NanoVak Sputtering Systems

After conditioning the sputtering device for a suitable plasma characteristic, the growth rates for magnetite, niobium, gold, and titanium targets are manually calibrated by using photoresist patterned silicon wafers as calibration gratings for AJA system. Target materials are deposited at fixed parameters and deposition time is recorded. An image of the deposition process is given in Figure 17.

Figure 17. DC Sputtering of niobium target in AJA at 100 W DC power

After depositing the material on the calibration grating, the photoresist is removed by rinsing acetone and thin film thickness is measured on different sites of the film by using a profilometer. After the measurement, the growth rates for magnetite and niobium targets are obtained by dividing the thickness to the elapsed sputtering time.

For the thin films grown in NanoVak system, the deposition rate is obtained by two quartz crystal monitor (QCM) devices located near the sample holder, and thicknesses are cross-checked with the profilometer measurements.

3.1.4. Sputter Deposition of Niobium and Iron Oxide Thin Films

Niobium thin films are systematically deposited on substrates with changing sputtering powers and gas pressures in NanoVak and AJA sputtering systems. Before deposition, pre-sputtering is carried out for 30 minutes in order to clean the surfaces of the targets while target shutters are closed. The deposition of Nb thin films is done at room temperature followed by coating a gold layer with thickness of 5 nm on the top of Nb films in order to prevent atmospheric oxidation of niobium. A list of samples and sputtering parameters for niobium thin films are depicted in Table 1.

Table 1. Sputtering parameters for niobium thin films on periclase and sapphire substrates grown at NanoVak sputtering system

Sample Name	Substrate	Base Pressure (Torr)	DC Power (W)	Mass Flow Rate (sccm)	Working Pressure (Torr)	Temperature (°C)	Growth Rate (Å/s)
N1	MgO	6.57×10^{-7}	74.1	0.9	7×10^{-3}	250	0.55
N2	MgO	9.46×10^{-7}	73.6	0.9	7×10^{-3}	25	0.52
N3	MgO	2.96×10^{-7}	72.8	3.7	12×10^{-3}	25	0.47
N4	Al_2O_3	6.57×10^{-7}	74.1	0.9	7×10^{-3}	250	0.54
N5	Al_2O_3	9.46×10^{-7}	73.6	0.9	7×10^{-3}	25	0.51
N6	Al_2O_3	2.96×10^{-7}	72.8	3.7	12×10^{-3}	25	0.49

After optimizing sputtering parameters for the growth of niobium thin films, iron oxide deposition is carried out using AJA sputtering system. A series of iron oxide thin films are grown on MgO substrates with in-situ heating at different temperatures. The temperature range have been extensively studied in the magnetite film deposition by in-situ heat treatment before the growth experiments. Prior to the film deposition, the substrates are heated at 700 ^{O}C for 1 hour to remove some hydroxide groups on the surfaces. After the growth, 5 nm thick titanium cap layers are coated at room temperature on top of each thin film in order to prevent oxidation. The list of magnetite samples and sputtering parameters are shown in Table 2.

Table 2. Sputtering parameters for magnetite thin films on periclase substrates grown at AJA sputtering system

Sample Name	Base Pressure (Torr)	RF Power (W)	Mass Flow Rate (sccm)	Working Pressure (Torr)	Temperature (°C)	Growth Rate (Å/s)
M3	1.7×10^{-8}	40	5.0	8.3×10^{-3}	25	0.032
M4	2.5×10^{-7}	40	5.0	8.3×10^{-3}	300	0.037
M5	3.3×10^{-7}	40	5.0	8.3×10^{-3}	400	0.038
M6	3.7×10^{-8}	40	5.0	8.3×10^{-3}	500	0.042
M7	4×10^{-8}	40	5.0	8.3×10^{-3}	600	0.045

One of the main challenges of the experiment was low growth rates for iron oxide thin films. After the deposition, iron oxide samples are characterized by using X-ray diffraction (XRD), Raman spectroscopy, vibrating sample magnetometry (VSM) magnetic force microscopy (MFM), and transport measurements.

After the optimization experiments are carried out for the growth of the thin films, the design and the fabrication flow of the junction is formed and carried out.

3.2. Design and Fabrication of Coplanar Josephson Junctions

Many considerations are made before the fabrication of the junctions, such as top to bottom and bottom to top fabrication approaches, coplanar, step-like and stack type fabrications, intersection geometry of the weak link, and so on. A modular and practical fabrication idea is followed first by creation of the junction designs, followed by the liftoff protocol fabrication procedure.

3.2.1. Design

To form the junction stacks with 4-point contact leads, a process flow chart was prepared according to the bottom-to-top fabrication protocol. The junction design and all steps in the process flow chart were planned considering the constraints of fabrication steps, performed in two different laboratories.

Technical design of the junction is realized by using AutoCAD software. The superconducting electrodes of junctions are designed in a bow-antenna shape where the tips of both electrodes are designated as sub layers for precision writing in the lithography process. The layout designs shown in Figure 18 consist of four layers which are employed separately to form the junction layers such as the bottom Nb electrode with alignment markers (1^{st} layer), the top Nb electrode (2^{nd} layer), outer contact leads (3^{rd} layer), and a window to separate the contact on the same Au layer. In the design, four different junction units with a size of 5x5 mm^2 can be fabricated on the same MgO substrate (1 x 1 cm^2). For alignment of subsequent layer on the previous one, 20 x 20 μm^2 square-shaped alignment markers are used in the lithography process.

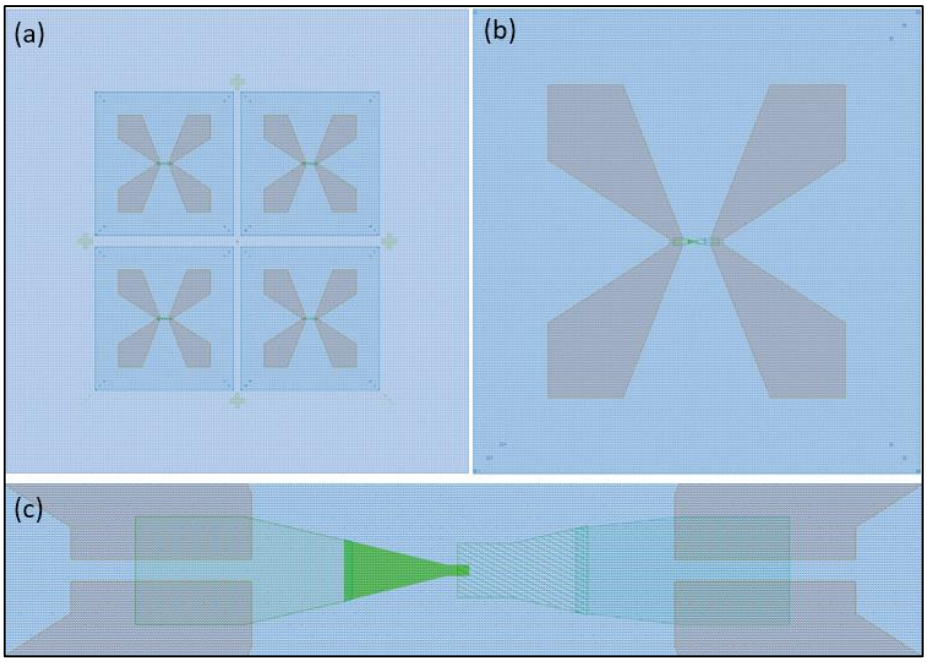

Figure 18. Coplanar Josephson junction design: (a) Complete design on a 1 cm x 1 cm layout, (b) 5 um x 5 um junction die with contact pads, (c) junction area close-up.

The wider electrode is designed for patterning on top of the smaller electrode in order to prevent shunting from sides. Since magnetron sputtering has conformal step coverage, the side walls of the smaller superconducting electrode are covered with magnetite, ultimately preventing a short circuit between electrodes.

3.2.2. Fabrication Process

Coplanar Josephson junctions are fabricated on MgO substrates using the bottom-to-top fabrication techniques. The lift-off protocol is used to form all junction layers with desired size and geometry. In this fabrication protocol, windows with a desired undercut feature are opened on a spin coated resist layer by using lithography, followed by the deposition of the desired material, and finalized by dissolving the resist in high grade acetone. Depositions of niobium electrodes and ultra-thin iron oxide tunneling layers, and the ion milling process were carried out in AJA sputtering system at Boğaziçi University. Patterning is done by using non-reactive ion etching and electron beam lithography (EBL), and contact pads are deposited by thermal and e-beam evaporation

techniques, which were carried out in the cleanroom of SUNUM at Sabanci University. The parameters for the EBL, evaporation and etching processes are optimized during the progress of the project by SUQUD research group and used in the fabrication of the junctions. The experiments and corresponding results of the optimization processes are not included in this work.

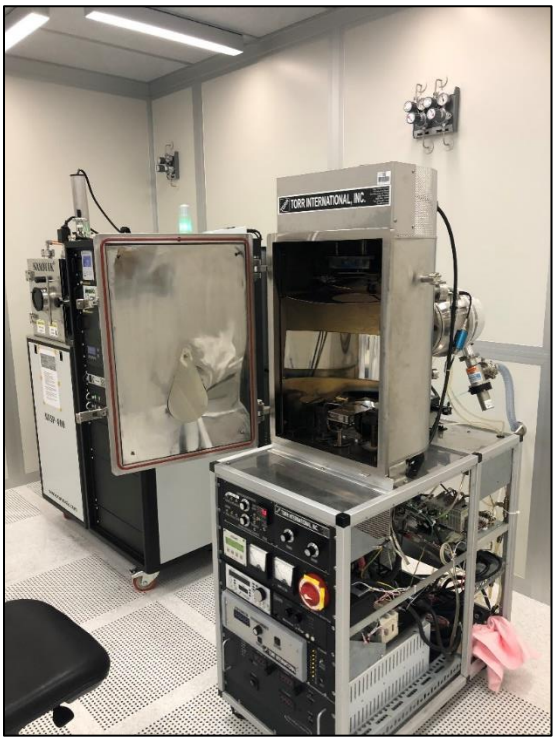

Figure 19. Torr International thermal and e-beam evaporator

Electron beam lithography is an advanced fabrication technique which utilizes an electron beam to generate a pattern from a polymer-based e-beam resist material. The desired pattern is written on the resist by e-beam exposing with a nanoscale resolution. Prior to the first lithography process, the substrates are cleaned using the same procedure described in the previous section. Then, bilayer polymethyl methacrylate (PMMA) layers with two different weights (495 PMMA C6 and 950 PMMA A4) are sequentially covered by spin-coating technique. Once the bottom PMMA layer is coated, the sample is baked on a hot plate at 170° C for 3 minutes. The top PMMA layer is baked at the same temperature for 20 seconds. Since MgO platform is an insulating material, 27 nm of chromium (Cr) is thermally evaporated on top of PMMA in order to ground and prevent the damage originating from charging during the electron beam

exposure. The conductive layer should be relatively thin in order to be able to monitor the conductive marker features underneath the PMMA layers. Then the sample is mounted on the sample stage of EBL with proper grounding, and the holder is inserted into a calibration microscope. After leveling the sample height on stage by adjusting three sensitive elevation screws, coordinates of the alignment markers on the design are determined and recorded through the microscope, which completes the calibration of the sample stage. Then, the stage is loaded inside the load lock of Raith EBPG5000+ electron beam lithography system. An image of the sample loaded and grounded in the sample stage is shown in Figure 20 (b).

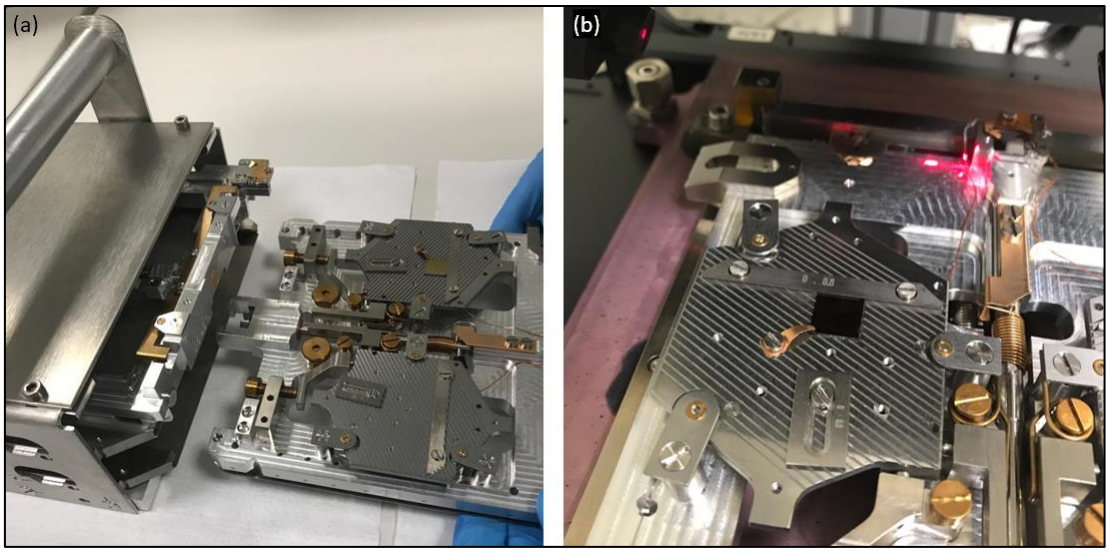

Figure 20. (a) Sample stage of EBL before mounting the sample. (b) Grounded sample on the sample stage.

After loading the sample stage, the recorded marker coordinates are defined in the system software and a reference marker is identified by a quick e-beam scan with the minimum required dose. After referencing, the device can align the designed pattern precisely on the previous one and then designated areas on the PMMA layer is exposed to e-beam with 1500 $\mu C/cm^2$ dose. E-beam exposure breaks the cross links of the PMMA resist which can be removed by puddling the sample inside a developer; a special chemical solvent. The tip of the electrode is exposed by applying lower current for higher precision.

Figure 21. Raith EBPG5000 plus ES 100 kV electron beam lithography system

After e-beam exposure, the sample is immersed into a chrome etchant (TechniEtch Cr01) to remove the chrome on the top of the PMMA layer followed by developing process to remove the exposed PMMA layers. In our processes, two different methyl isobutyl ketone (MIBK) solutions diluted with isopropanol in 1:3 and 1:1 volume ratio are used for sequential develop of the resist, which were applied for 60 and 20 seconds respectively. Then, the process is stopped by washing out the sample in isopropanol for 30 seconds and the solvents are removed by blowing dry nitrogen. The rest of resist residues is cleaned by applying 100 W oxygen plasma for 20 seconds. Thus, the sample is ready for thin film coating in the lift-off protocol.

The fabrication process for the coplanar junction consists of 15 steps. A cross sectional flow of the fabrication is illustrated in Figure 22.

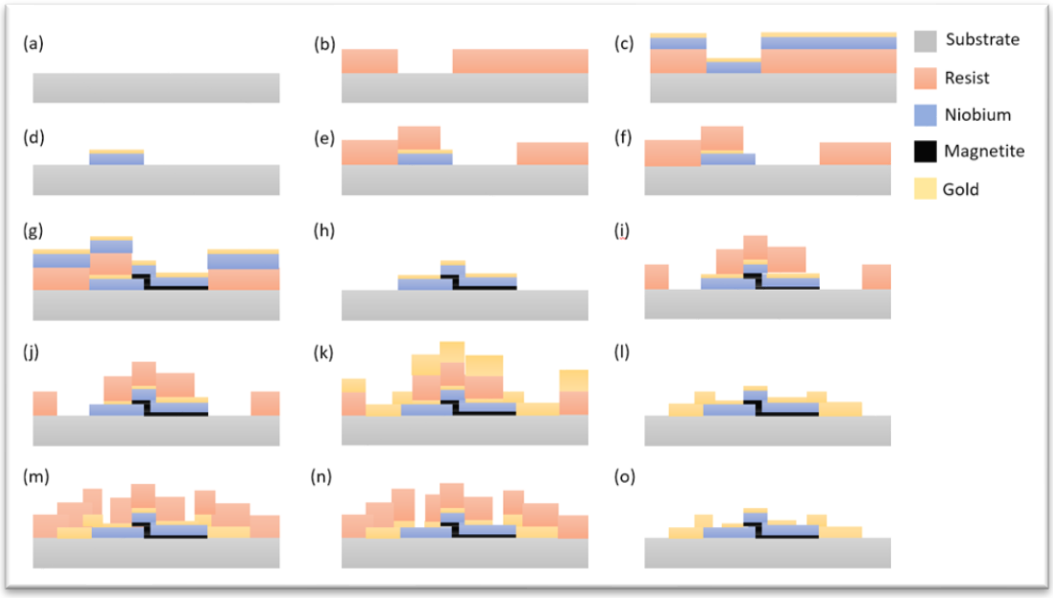

Figure 22. Cross sectional fabrication steps of coplanar Josephson junction. Step by step; (a) empty substrate, (b) first EBL for bottom electrode windows, (c) bottom electrode deposition, (d) liftoff, (e) second EBL for top electrode windows, (f) ion milling of Au cap layer, (g) tunneling layer and top electrode deposition, (h) liftoff, (i) third EBL for contact windows, (j) Au cap layer etching, (k) Cr/Au contact pad deposition, (l) liftoff, (m) fourth EBL for contact separation, (n) Au cap layer etching, (o) liftoff

At the first step, bottom electrode window and marker windows are opened by EBL as described above (Figure 22-b) (Figure 23-a). Then, 130 nm thick bottom niobium electrode is deposited by using magnetron sputtering at 100 W DC power in an argon pressure of 2 mTorr, which were found as the best growth parameters in our Nb growth experiments. The niobium depositions followed by in-situ coverage of a gold cap layer with thickness of 5 nm in the same sputtering environment at 30 W DC power (Figure 22-c). Then, the sample is kept in acetone overnight to remove the PMMA, which completes the lift-off protocol for the first electrode (Figure 22-d) (Figure 23-b) . After the first liftoff process, a subsequent EBL patterning is carried out using the same growth and lithography parameters to form the top electrode (Figure 22-e) (Figure 23-c). Prior to the deposition of the Fe-O and top Nb, Au layer on the bottom Nb electrode is cleaned by ion milling generated at 40 W power under 8.6 mTorr working pressure of argon in the AJA chamber (Figure 22-f). This is a good option to remove layers and deposit a new one without breaking the vacuum of the ALA system. Thus, Fe-O tunneling layer can be sandwiched between two Nb layers. After etching the cap layer, 6 nm of Fe-O thin film is sputtered from Fe3O4 target on the sample at 40 W RF power

under 8.3 mTorr working pressure of argon at room temperature. During the deposition, heat treatment is not applied to the sample since it can oxidize the Nb film surface. Right after Fe-O deposition, 130 nm of niobium with 5 nm gold cap layer is deposited with the previous parameters (Figure 22-g). After deposition, the sample is left under acetone overnight before the contact pad fabrication (Figure 22-h) (Figure 23-d). Thus, a coplanar Josephson junction is formed on the MgO substrate. To form the gold contact leads of the coplanar junction bar, another lift-off process is carried out by e-beam lithography and metal evaporation steps (Figure 22-i,j,k,l) (Figure 23-e,f). Usually, 20 nm of chromium is first deposited as an adhesion layer by using e-beam evaporation, followed by 100 nm gold deposition by thermal evaporation. The contact pads on both electrodes are overlapped on the gold cap layers of the Nb electrodes so a "T" shaped window is opened on the top of the electrodes by EBL (Figure 22-m) (Figure 23-g). Then, the gold layers between the contact points are removed by applying 300 W Ar plasma for 30 seconds in 3 cycles with 10 second breaks at each cycle by using Oxford ICP-RIE dry etching device in SUNUM (Figure 22-n). This process performed for separation the contact pads ensures a 4-point contact geometry for the junction stack. Thus, the contact resistance between Au/Nb is eliminated in the transport measurements. After etching, liftoff process is carried out (Figure 22-o).

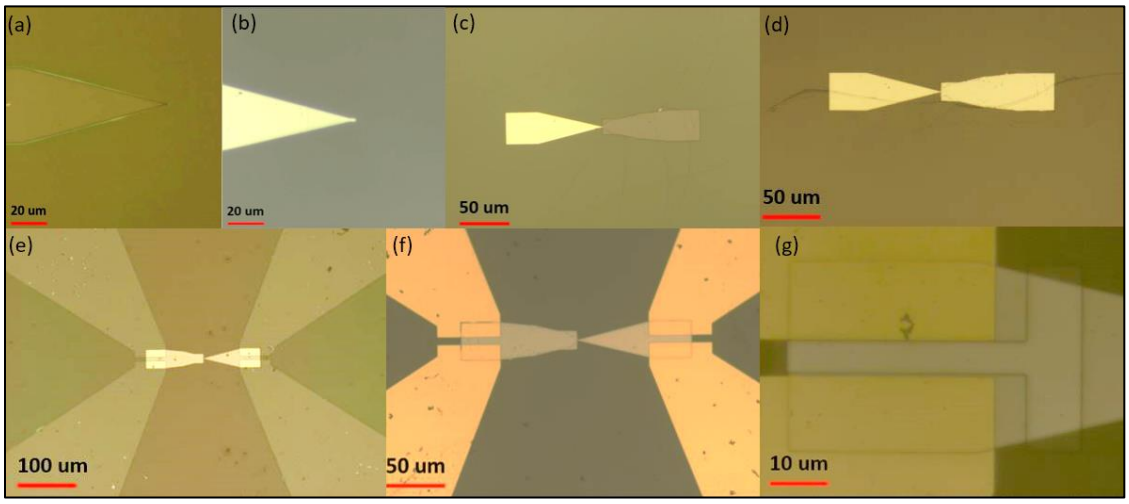

Figure 23. Optical Microscope images of the fabrication steps; (a) first electrode window, (b) bottom niobium electrode, (c) second electrode window, (d) top niobium electrode with bottom electrode, (e) contact pad windows, (f) niobium electrodes and contact pads, (g) "T" shaped window for contact separation.

The fabricated sample is mounted on a chip holder using silver paste. Electrical interconnections between contact bars of the chip holder and four contact terminals of

the sample is individually made by gold wire bonding technique using TBT HB16 semiautomatic wire bonder. Optical microscope and SEM images of junctions are depicted in Figure 24.

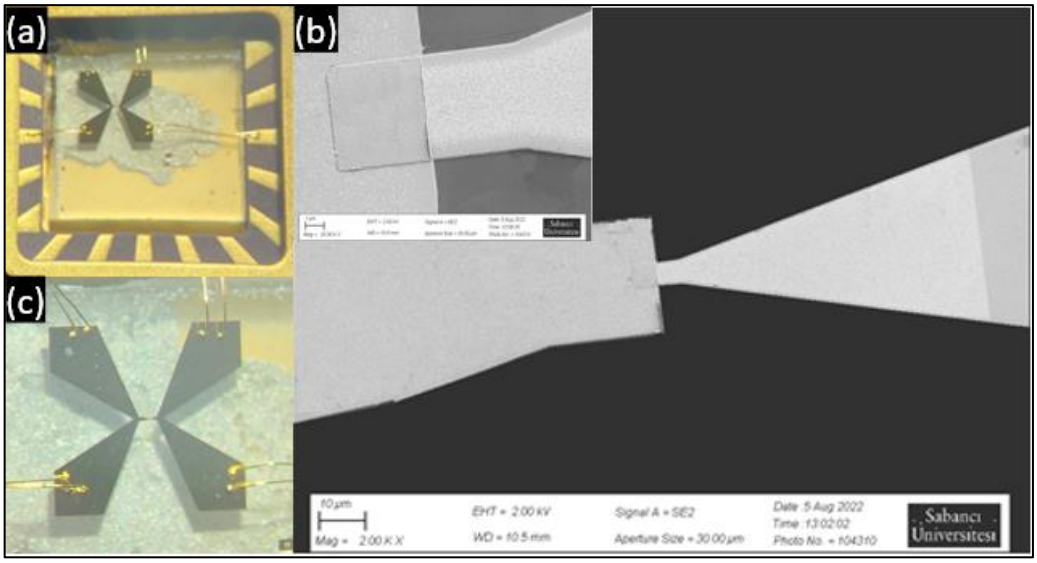

Figure 24. (a) Coplanar Josephson junction bonded on the chip holder. (b) Close up image of the junction under optical microscope. (c) inset shows the SEM image of the coplanar Josephson junction with SEM image of the overlapping tunneling region at the inset.

During the wire bonding process, 500 x 500 nm^2 junction is damaged from static discharge, therefore it is discarded.

For the in-plane transport measurements, iron oxide sample M6 is diced by using a wafer scriber in order to fit the chip holder, which is 5 x 5 mm^2. Then, shadow evaporation technique is used by alligning and fixing a shadow mask on top of the polished side of the sample, followed by gold evaporation in Torr evaporator for 4-point measurements

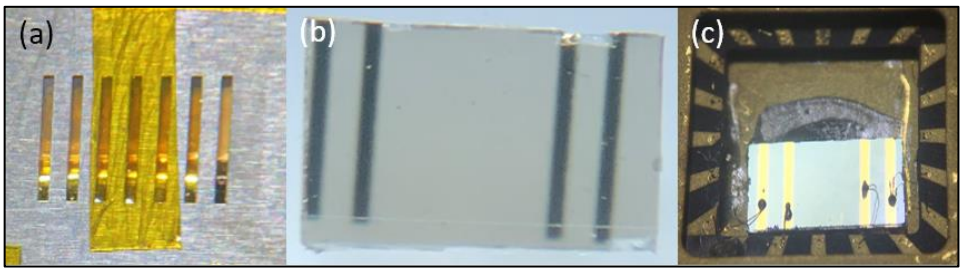

Figure 4. (a) Iron oxide sample with mounted shadow mask, (b) gold evaporated sample, (c) sample mounted on the chip holder with manual contacts

After wire bonding, transport measurements are carried out for the samples.

3.3. Structural Characterization Experiments for the Thin Films

Structural characteristics of thin films are investigated by three different characterization techniques. A picture of three different equpment used in characterization is given in Figure 26 below.

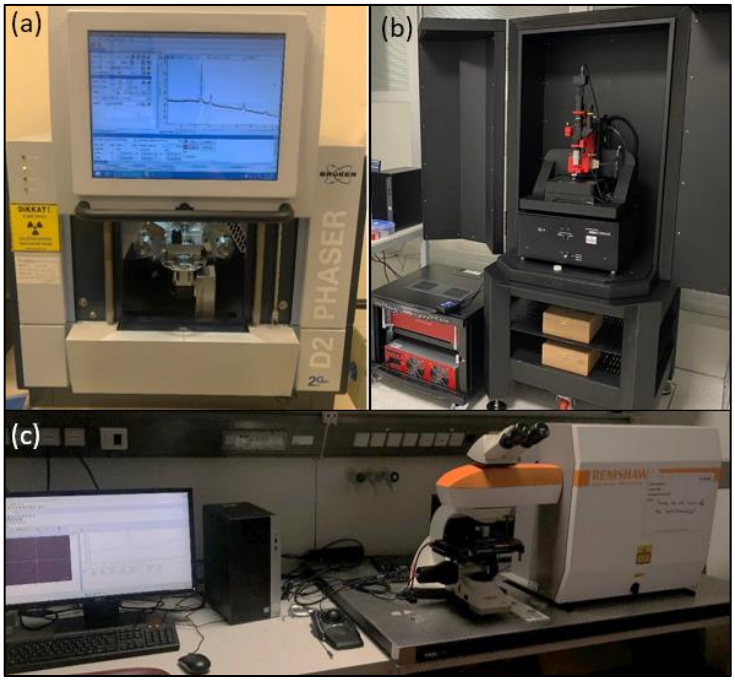

Figure 25. (a) Bruker D2 Phaser XRD System, (b) NanoMagnetics hp-AFM high performance atomic force microscope, (c) Renishaw Raman spectrometer

X-ray diffraction measurements are carried out for crystallographic analysis of the thin films using Bruker D2 Phaser XRD system which is located at FENS building in Sabancı University (Figure 26-a). The system is a tabletop spectrometer including ports for 6 samples which can be used for both thin films and powder samples. The system includes an embedded control computer with an analysis software (EVA), and measurement space with appropriate shielding. The most important parts of the system consist of a Cu based X-ray tube, which is used with a Ni filter for Cu-α emissions with 1.542 Å wavelength, a built in high quality silicon strip detector (LYNXEYE), which is used to obtain diffracted X-rays from the sample, and two crossed rotating arms to hold

the tube and the detector with an electronic goniometer in between the arms in order to obtain the angle to construct the XRD spectrum. All of the spectrums are scanned between 5-90 degree angles with 0.02 º increments. After obtaining the XRD spectra of samples, two correction procedures are applied to the raw data for each sample by using EVA. The first one is the background subtraction where the background intensities are subtracted from the spectrum. Second one is the displacement correction due to the leveling of the sample on the sample holder. With the corrected dataset, search-match algorithm is used with using PDF database, followed by Bragg and Debye-Scherrer analyses operated on EVA.

Following the XRD measurements, Raman spectrums are acquired by using Renishaw Raman Spectrometer, which is located at SUNUM (Figure 26-c). It is a tabletop spectrometer which uses 45 W power laser of 532 nm non-polarized wavelength with 0.3 cm^{-1} spectral resolution. The spectrums are acquired with %50 laser intensity between 100-1600 cm^{-1} wavelength shift intervals and with 20 seconds of acquisition time. No corrections are required for the raw data after the measurement.

After the Raman spectrometry of iron oxide thin films, AFM/MFM measurements are carried out by using NanoMagnetics hp-AFM system, which is located at SUNUM (Figure 26-b). The system is equipped with a closed loop flexure scanner and an optic microscope with 700 nm optical resolution. Before the MFM measurement, a magnetic tip is magnetized and a calibration measurement is carried out by using a magnetic tape. An image of the tape and measurement is depicted in Figure 27.

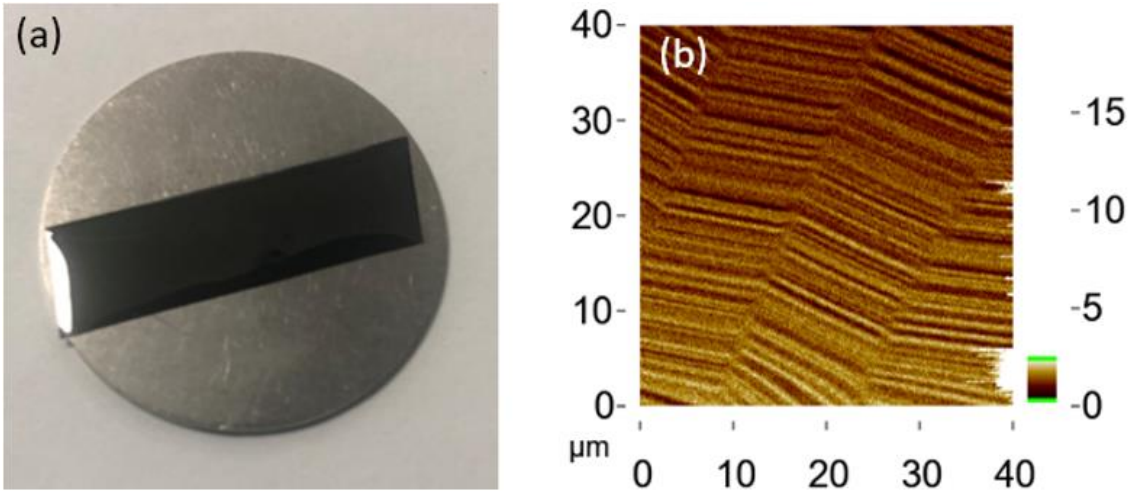

Figure 26. (a) Image of the magnetic tape and (b) calibration measurement of the magnetic phase of the magnetic tape

3.4. Cryogenic Characterization Systems for Transport Measurements

In order to investigate the Verwey transition for iron oxide thin films and superconducting properties of niobium thin films and coplanar Josephson junctions, two different cryogenic systems located in Sabancı University and Boğaziçi University are employed.

3.4.1. Oxford Instruments Teslatron PT Cryostat Measurement System

For the transport measurements, Oxford Instruments Teslatron PT cryostat is used in SUNUM. It is capable of cooling the sample space down to 1.5 K, which is enough to monitor the basic transport characteristics of the junction below the transition temperature of Nb (< 9 K) . A picture of the cryogenic system and measurement rack is shown in Figure 28.

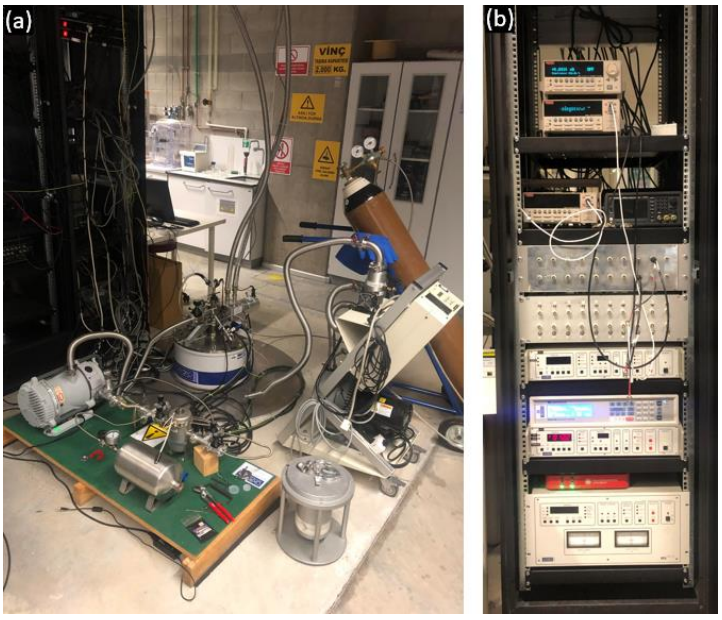

Figure 27. (a) Oxford Instruments Teslatron PT cryostat system. (b) Measurement rack from top to bottom; Keithley Model 6221 DC and AC current source, Keithley Model 2182A nanovoltmeter, (left) Keithley Model 2182A nanovoltmeter and (right) Keysight 33500B true form waveform generator, I/O cabinet for default sample probe, I/O cabinet for rotator sample probe, Oxford Instruments ITC temperature controller, Lake Shore model 336 temperature controller, Oxford Instruments ITC temperature controller, rotator driver, Oxford Instruments IPS magnet controller.

The cryogenic measurement system consists of a sample space, a sample probe, a cold head cooled down to 3 K by a helium compressor, a variable temperature inert (VTI) which is another close helium cycle that transfers the cooling power of cold head to the sample space, and a superconducting solenoid magnet which can generate a magnetic field up to 5 T. Two temperature sensors and two heaters with PID controllers are located one from each on the VTI and sample space respectively. Also, a rack containing controller units, input-output (I/O) boxes and measurement instruments is employed. It is possible to adjust the cooling or heating of the sample space by changing the pressure of VTI cycle or by biasing the heaters.

Before starting the measurement, contact pads and their contact pin positions for the corresponding channel numbers on the input output box are determined and recorded from the optical microscope on the sample. Then, the chip holder with the mounted sample is loaded at the chip holder space, which is on the tip of the sample probe. The chip holder is loaded at a right orientation for the contact pins to match with the I/O channels. After loading the sample, the sample probe is inserted inside the cryogenic enclosure with an o-ring in between the fittings and sealed with a vacuum clamp. A picture of the sample probe is represented in Figure 29.

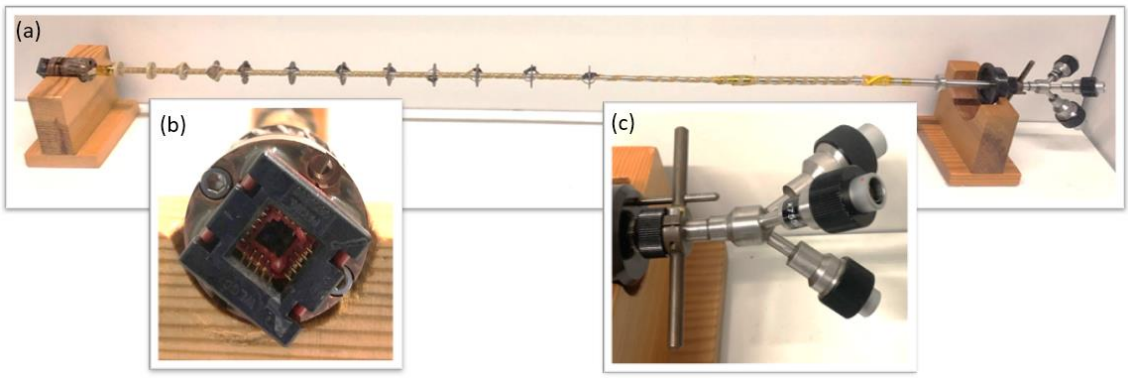

Figure 28. (a) Sample probe, (b) sample space for the chip holder, (c) Fischer connectors for control and measurement

The sample space is purged 3 times by using helium gas and a turbo molecular pump after integration. After the purge, the system is ready for the measurement. The connections are established from the DC current source and a high resolution nanovoltmeter to the I/O box for the desired channels. For the transport measurements

of thin films, the source and drain of the DC current source are connected to the corresponding channels of the outer pads and two voltage terminals are connected to the channels of the inner pads. For the transport measurements of the junctions, source and drain of the current is connected to opposite electrode pins, so as the voltage terminals. The current is applied from the wide electrode to the narrow one.

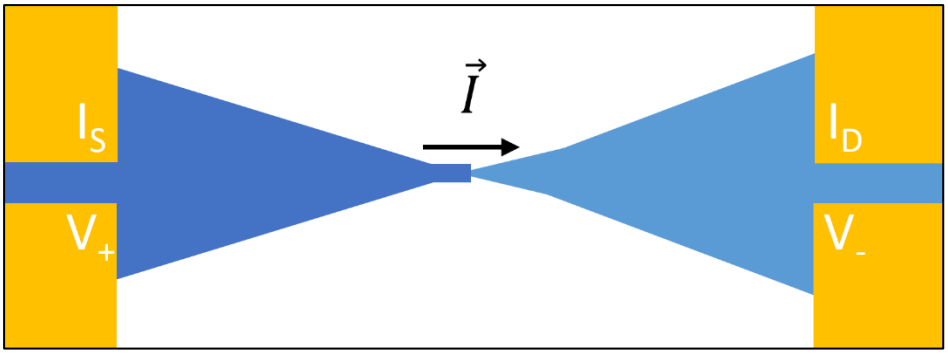

Figure 29. The direction of current flow and the connections of the junction

Data acquisition and live representation together with the control and automation of the instruments in the measurement rack is performed by utilizing LabVIEW programs for different types of transport measurements.

For the current vs voltage (IV) measurements, the temperature is fixed to a desired point and a DC sweep is applied with desired increments down to 100 fA. Junctions are measured with 300 μA sweeps and with 5 μA increments for the low branching of the voltage. For the critical currents, different sweep intervals are chosen in orders of mA. The corresponding voltages are obtained and plotted in real time.

For the resistance vs temperature (RT) measurements, delta mode is used where desired number of positive and negative current pulses are applied to the sample and the voltages are measured simultaneously after each pulse where three point moving averages of the voltage are taken in such a way that each averaging cycle starts with the next pulse. Then, the measured voltages are averaged with the number of cycles to get a precise voltage value. By dividing the voltage values to the applied currents, the resistance values are obtained with changing temperature where the temperature can be

adjusted from either VTI or the heaters, and measured simultaneously with the resistances.

For the magnetic field measurement, the superconducting coil is heated to normal metal region by an embedded magnet heater and a current is applied to the coil in order to generate the desired magnetic field. Then, the magnet heater is closed where the coil is cooled to superconducting region, entering into persistent mode where the field is fixed. After fixing the field point, an IV measurement is carried out as described above and the process is repeated for the next magnetic field point.

3.4.2. Quantum Design PPMS and VSM System

For the vibrating sample magnetometry measurements, Quantum Design PPMS system with a VSM extension toolkit is used. The system is located in Boğaziçi University and operated by BUSPIN research group. It consists of a cryostat capable of reaching 10 K base temperature, a sample space, a solenoid magnet, a VSM head extension with an oscillator drive, a sample holder, a calibration ruler, a probe, motor drivers and connectors, and an external measurement rack containing various measurement electronics. A picture of the system at VSM configuration is given below in Figure 31.

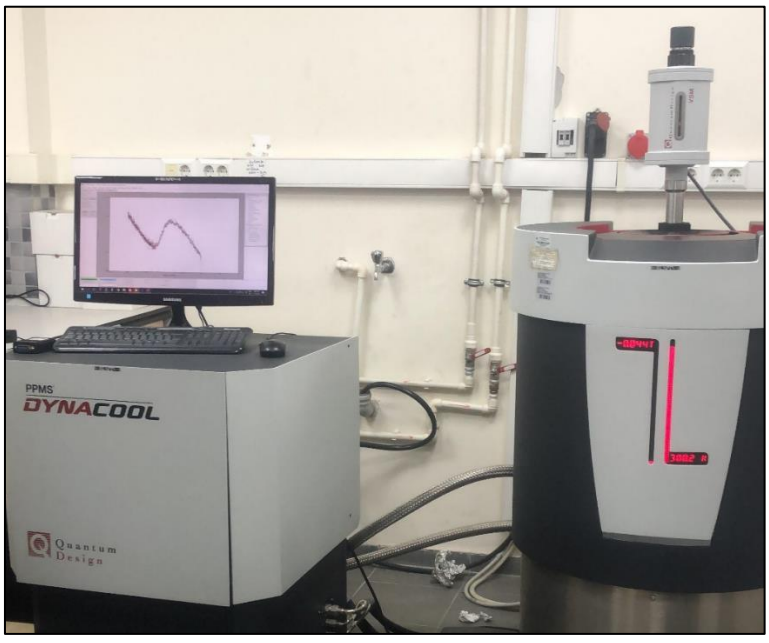

Figure 30. Quantum Design PPMS with mounted VSM measurement equipment

For the VSM measurements, an embedded software of the Quantum Design PPMS system is used. A crystal sample holder with low paramagnetic contribution is used to carry the sample during the measurement. First, the sample is fixed on the crystal by wrapping Kapton tape one and a half revolutions around the crystal without any air gap between the tape, sample, and holder. The amount of the tape used for each measurement is approximately fixed due to the tapes paramagnetic contribution. The width of the sample holder is 3 mm and the active length for the VSM measurement is 5 mm. The coated side of the sample is facing towards the crystal. The position of the sample is determined on a calibration ruler. Figure 30 depicts a picture of the sample holder standing on the ruler.

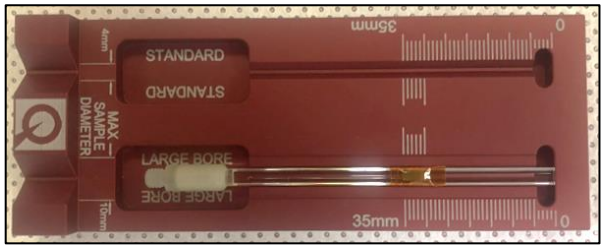

Figure 31. Calibration ruler with the sample taped on a crystal sample holder

After fixing the sample on the crystal with precision, sample holder is mounted on a long probe by screwing the bore on the sample holder, and probe is inserted into the PPMS system, where the sample is ready for measurement.

Starting the VSM measurements, measurement sequences are created as recipies from a very simple and effective software interface in an easy manner. After creating a measurement recipie, the device runs a calibration in which it vibrates the sample at different heights with a uniform applied field and tries to detect its location. Usually, the sample is found at the reference location. If the sample is not found at the scan, it is possible to manually enter the height of the sample, which points out the cruciality and precision requirement of the calibration step. At first a magnetic field sweep is applied while measuring the magnetization of the sample. If the sample is magnetized, at a magnetic field threshold the magnetization is saturated. When the magnetic sweep is

reversed in direction, the magnetization either follows the same path, or a hysteretic path depending on the coercivity of the sample, which shows the relaxation behavior of magnetization. Saturation magnetization values are obtained from magnetization vs applied magnetic field (MH) curves at room temperature. Then the obtained magnetic field amount is applied constantly while the magnetization is recorded with decreasing temperature (MT), which is known as field cooling (FC) measurement. At 150 K, another MH measurement is carried out in order to check if the magnetization of the sample is shifted before the expected Verwey transition. Then, its magnetization versus temperature is measured by FC down to 10K. The last MH scan is carried out at 10 K. The paramagnetic contribution from the sample holder, tape and MgO substrate are recorded as a calibration measurement and subtracted from the raw data before representation.

4. RESULTS & DISCSSION

In this section, the results of different characterizations that were carried out for the thin films and junctions are discussed with highlighting matches and discrepancies throughout the measured physical parameters. In the first part, the effects of the growth condition on the crystalline structure and electrical/magnetic characteristics of the films are discussed. For this purpose, a series of thin-film growth experiments were carried out in the sputtering systems to determine ideal growth conditions for “true” Nb and Fe_3O_4 depositions. In addition to the set of the deposition parameters, in-situ heat treatment is applied to MgO substrates in a temperature range from 300°C to 600°C for Fe-O films deposition. The best condition found in the film growth experiments with a heat treatment was not employed to form the tunneling layer of the coplanar junction, but they show promising results for desired structural and electrical characteristics of Fe-O films. In the second part, the electrical transport characteristics of the coplanar Josephson junction with a Fe-O tunneling barrier are discussed. Their transport RT and IV measurements allows to basically confirm the growth and fabrication conditions in the tunneling characteristics across our junctions, and the consistency with the Stewart-McCumber model.

4.1. Characterization of Niobium Thin Films

X-ray diffraction and transport measurements are carried out in order to elucidate the effects of the crystal structure on electrical transport properties of niobium thin films. Figure 33 shows XRD spectra of the films grown on MgO (a-c) and Al_2O_3 (d-f) substrates under various sputtering conditions. XRD results of the films grown at 250°C on each substrate are also depicted in Figure 33 (a,d). The XRD scans of the films indicates mostly diffraction peaks corresponding to a body-centered cubic (bcc) Nb, in

good agreement with XRD results in the literature.[54] However, their XRD results indicate a polycrystalline texture because of the presence of the multi peaks appeared at approximately 38.7°, 56°, 70°, and 82.5° corresponding to (110), (200), (211) and (220) respectively. Moreover, the reflection peak at around 62° confirms a crystalline Nb_2O in the film structure. This can usually occur due to high affinity of Nb for oxygen. It is well known that Nb film surface immediately oxidizes when it contacts with oxygen in the atmosphere. This result shows that Nb films need a thin cap layer to protect the film surface from oxidation.

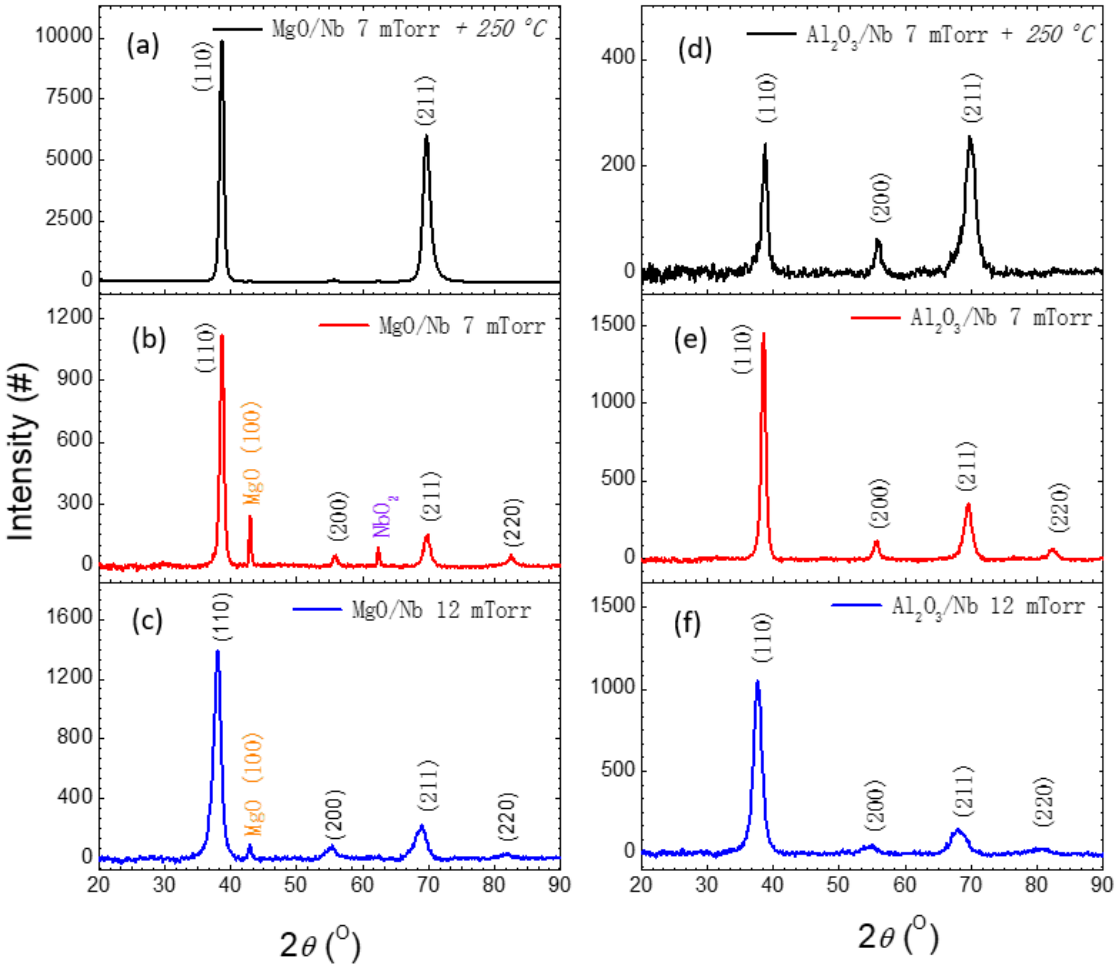

Figure 32. XRD spectrums of Niobium thin films deposited in NanoVak sputtering system on (a)(b)(c) MgO and (d)(e)(f) Al_2O_3 substrates at different argon working pressures: (a)(d) 7 mTorr with 250 ºC in-situ heating, (b)(e) 7 mTorr at room temperature, (c)(f) 12 mTorr at room temperature

It is observed that the other thin films are densely oriented through (110) crystallographic plane. It shows that lower working pressures are much preferable to

attain crystalline niobium films on MgO and sapphire. Moreover, the second dominant (211) peak was found in the XRD spectra of the films grown at 250° and (200) and (220) peaks were not detected. The d-spacing, lattice constant and crystalline size parameters were calculated from (110) peak for all coated Nb films using Bragg and Debye–Scherrer analysis, which are indicated in Table 3.

Table 3. Crystalline size, lattice constant and d-spacing parameters for niobium thin films grown on MgO and Al_2O_3

Sample	d-spacing (nm)	Lattice constant (Å)	Crystalline Size (nm)
N1 MgO – 7 mTorr + 250^{O} C	2.3259	3.2894	10.927
N2 MgO – 7 mTorr	2.3259	3.2894	10.753
N3 MgO – 12 mTorr	2.3588	3.3359	5.741
N4 Al_2O_3 – 7 mTorr + 250^{O} C	2.2671	3.2062	7.7397
N5 Al_2O_3 – 7 mTorr	2.2853	3.2318	9.7954
N6 Al_2O_3 – 12 mTorr	2.3416	3.3115	5.1895

In the Nb thin film growth, in-situ heating does not have an effect on d-spacing and lattice constant, and it has almost no effect on crystalline size. However, with increasing argon working pressure, lattice constant and d-spacing increase whereas crystalline size dramatically decreases. For the films grown on sapphire, these parameters were found to be low by in-situ heating whereas by increasing argon working pressure, lattice constant and d-spacing become larger unlike the crystalline size. These parameters combined with the phase results show that in-situ heating is desirable for niobium on MgO substrates while it is not the best option for niobium on sapphire substrates.

Results also exhibit that lower sputtering working pressures results in larger average crystalline size. In the field of superconductivity , the correlation between structural and superconducting properties of thin films is one of the most popular research topics. This correlation is still studied for Nb films.[55,56] In these studies, it was found that superconducting transition of thin films (T_c) approaches that of bulk Nb when average crystalline size is larger than 25 nm, while Tc gradually decreases by a decrease in the crystalline size. The obtained grain size of a series of thin films deposited at 7 mTorr on heated/unheated varies from 7.7 nm up to 10.9 nm while the change in their lattice parameters starts from 3.20 Å up to 3.28 Å. To determine their T_c, the in-plane transport measurements were performed from 300 K to 1.5 K with 4-point contact geometry. Figure 34 shows their resistance variations as a function of temperature (RT).

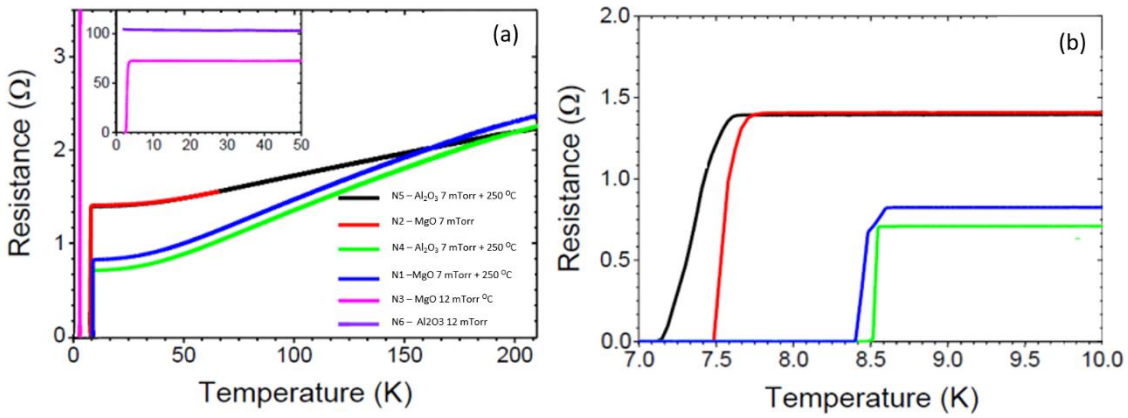

Figure 33. (a) RT plots for niobium thin films on periclase and sapphire substrates grown at NanoVak sputtering system with 12 mTorr samples on the inset (b) close-up to the transition region

The RT plots roughly show a regular metallic resistance behavior above T_c in which the resistance decreases with decreasing temperature. Figure 34 (b) shows a low temperature section of the RT plots to show their T_c variations. It is observed that in-situ heating has a positive effect on the critical temperature where both heated samples grown on MgO and sapphire have higher critical temperature than those of the other deposited at room temperature. The sample N4 exhibits the highest critical temperature at 8.5 K with a sharp transition ($\Delta Tc \sim 0.2$ K). Only sample N6 did not show any superconducting transition down to 1.5 K. The broadest transition width is found for sample N3. Also, it was consequentially found that decrease in T_c is correlated with an increase in resistance. Ar pressure for Nb films grown at room temperature resistance.

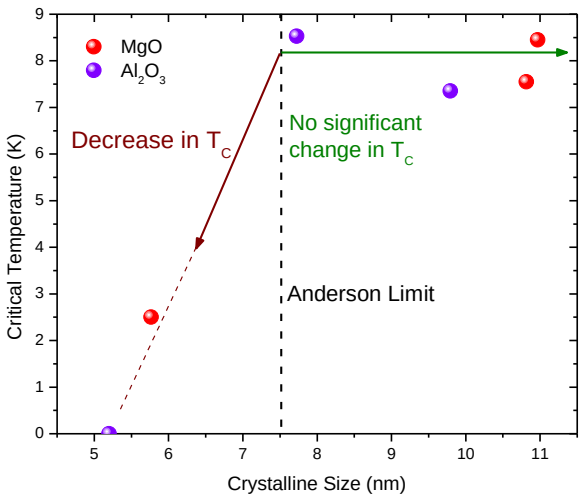

Figure 34. Critical temperature of niobium thin films with different average crystalline size for different substrates

In Figure 35 a variation of T_c with the crystalline size found in the RT and XRD characteristics of all Nb films. The plot reveals an abrupt drop below the crystalline size of 7 nm while it fluctuates above the critical value depending on oxidation of the films. The results agree for niobium thin films grown on Si and Si/SiO_2 substrates with numerous grain sizes and varying critical temperatures that are reported.[55,57]

In these reports, the correlation reveals that superconductivity cannot be induced in a Nb film whose crystalline size is smaller than the coherence length, where for Nb element, $\xi_0 \sim 38\, nm$ at absolute temperature. This implies a limit in the intermediate coupling BCS regime which is known as the Anderson limit.[58,59] Similarly, superconductivity can be induced and enhanced gradually beyond the critical size in Nb films grown in this thesis.

4.2. Characterization of Iron Oxide Thin Films

In the theory part, well known properties of magnetite and maghemite such as its space group, lattice constant, electrical resistivity, and magnetic properties are represented. Also, the characteristic Verwey transition and its origins are briefly discussed. With the use of these properties, it is possible to define the characteristic properties of grown iron oxide samples in the experiment. The uniqueness of Verwey transition allows the investigation of temperature dependent changing properties such as magnetization and resistance. For our purposes, it is possible to trace these characteristic properties through a series of measurements on the iron oxide samples in order to categorize, compare and obtain information. As a priority of this work, the focus of the analysis is on the electrical, magnetic and morphological properties of the samples, whereas the structural and chemical properties are also investigated and analyzed in a conventional manner.

Iron oxide thin films are sequentially characterized by using XRD, Raman spectrometry, magnetic force microscopy and electrical transport measurements in the given order. Additionally, vibrating sample magnetometry measurements are carried out

for magnetite thin films grown at the same process on different substrates with 2 mm x 5 mm surface dimensions. In the previous optimization studies, the best grown condition for desired Fe_3O_4 film deposition was found to be at 40W in the sputtering pressure of 8.3 mTorr. However, their structural analyses exhibited the presence of other Fe-O phases together with the Fe_3O_4, and a direct evidence of magnetite structure was missing. Therefore, a set of in-situ heat treatment was employed in addition to the best sputtering parameters in the growth experiments in this study. As explained in the experimental part, growth experiments were carried out at various temperature ranging from 300 °C to 600 °C with a 100°C increment.

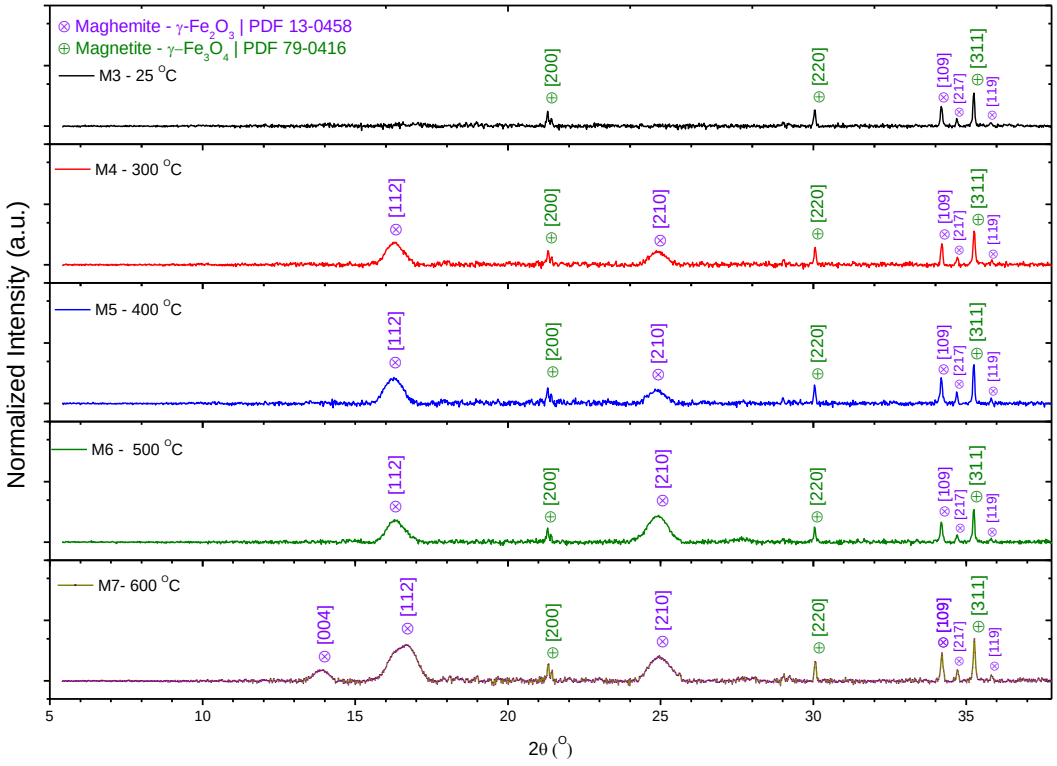

Figure 35. Combined XRD results for magnetite thin films on MgO substrates

The XRD results of the films are presented in Figure 36. Since the iron oxide samples are ultra-thin films (below 100 nm thickness), the substrate peaks dominate the XRD

spectrum, therefore X-ray intensity of the spectra is represented in logarithmic scale at the 2θ scan between 5° and 38°

All of the samples show polycrystalline structures where different crystal orientations for both magnetite and maghemite phases of iron oxide are observed in the XRD spectra of the thin films. With increasing in-situ heating temperatures, different maghemite orientations are observed and attributed as (112), and (210). For M7 one more crystal orientation is observed (004). In all of the samples, (311), (220) and (200) peaks are observed for magnetite. The sample grown at room temperature displays a smaller number of maghemite crystal orientations in comparison of that of in-situ heated samples. The XRD results reveal sub-oxide structures, but stoichiometric volume fraction of the Fe-O structures should be analyzed to confirm the XRD results.

After the XRD measurements, Raman spectrums are acquired in order to search for more information about different sub-oxide structures on iron oxide thin films. The resulting spectra are illustrated in Figure 37.

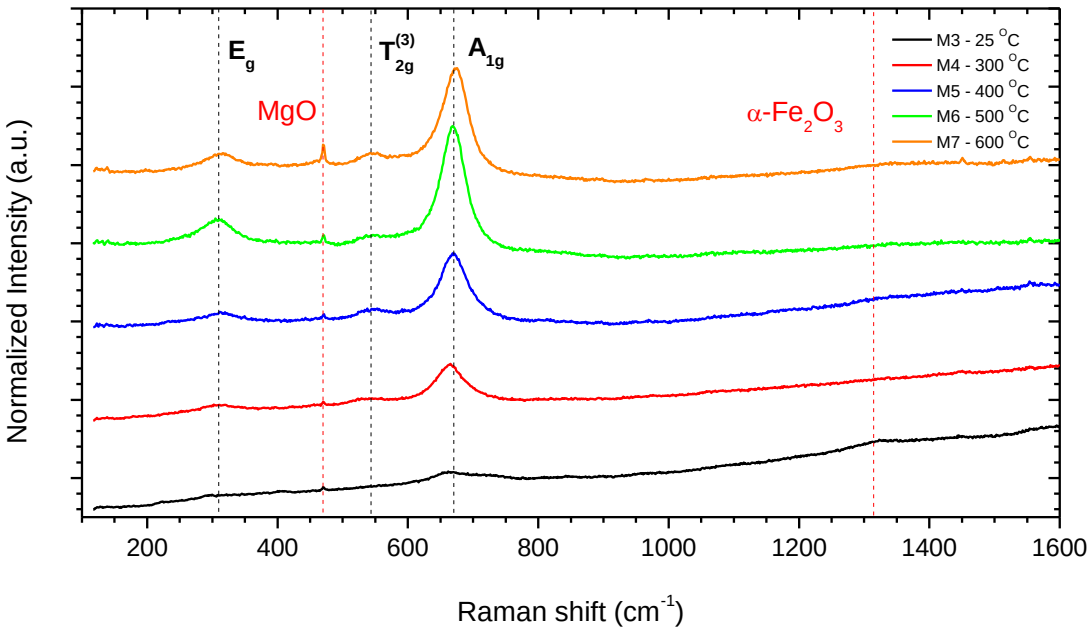

Figure 36. Combined Raman spectra of magnetite thin films

Magnetite has 5 different active Raman modes: A_{1g}, E_g and $T_{2g}^{(3)}$, which are assigned to bands at 666 cm^{-1}, 305 cm^{-1} and 537 cm^{-1} wavelength shifts, respectively.[60–62] The small sharp peak at 470 cm^{-1}, appearing by increasing the substrate temperature, is attributed to periclase substrate.[63] The peak at A_{1g} active mode is present for all thin films grown

with in-situ heat treatment. The Raman spectrum of film grown at room temperature exhibit a broad bump with low intensity approximately appeared at around the wavenumber of A_{1g} mode. Also, the same sample shows a small bump between 1200-1400 cm^{-1}, which is attributed to haematite.[64] The bump diminishes by heat treatment. It is observed that spectrum for sample M6 is the best match with the representative band of magnetite at 666 cm^{-1}. Without polarized Raman spectra with parallel and perpendicular polarization scattering geometries, it is hard to draw further conclusions such as the characteristics of anti-phase boundaries. [65] Results in XRD and Raman measurements may be speculative, in the sense of precisely identifying oxide compounds, specifically the presence of metal-oxides. Therefore, magnetic behavior should be studied to confirm the structural characteristics monitored in the XRD and Raman spectroscopies. Therefore, their magnetic characteristics were analyzed by magnetization measurements and magnetic force microscopy using VSM and MFM.

High performance AFM tool was employed to take the topographic and magnetic images of samples M3 and M6, which extremely exhibit distinct crystallographic structure in the Fe-O film series. By using MFM technique, it is possible to detect long range magnetic interactions by using a magnetic tip together with using the “lift mode”. The magnetic feature on the Fe-O film surface were mapped using a magnetized MFM tip integrated with a high-performance AFM device. Before the MFM measurement, a calibration measurement was done by using a magnetic tape. Topography measurements are carried under tapping mode and MFM measurements are done using the lift mode with 175 nm lift offset at zero external magnetic field. The surface morphologies and magnetic characteristics are shown in Figure 38.

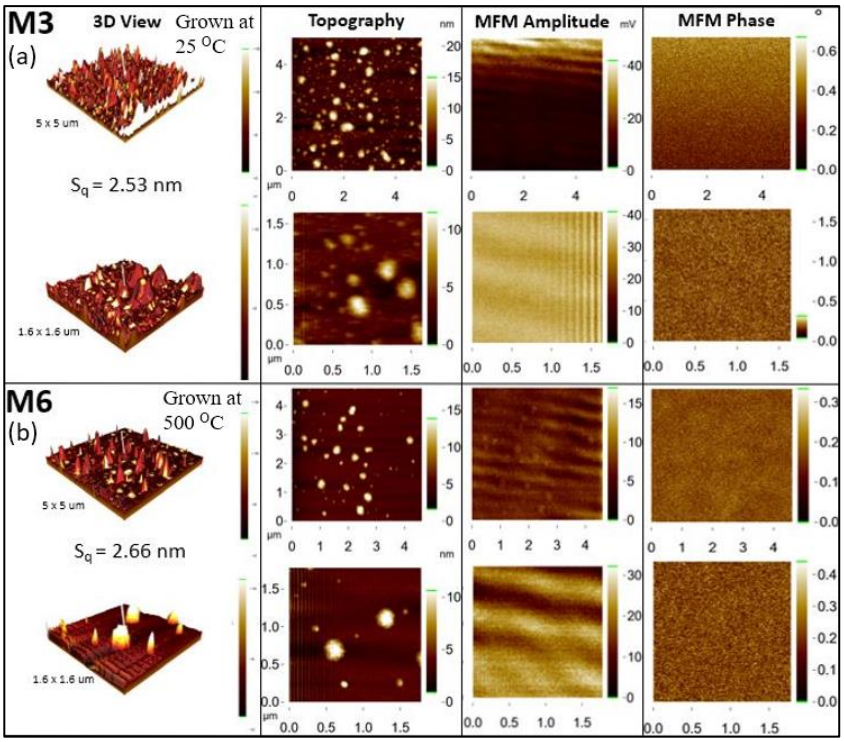

Figure 37. MFM images from two different sites with two different cross-sections of samples (a) M3 and (b) M6. From left to right; 3D View, topography, magnetic response amplitude, and magnetic phase

In comparison to 3D views and topography images of M3, M6 has higher a rms roughness of ~2.66 nm, with dense aggregate structures on the film surface. Topography image of M3 exhibits more seldom aggregates. The size of aggregates ranges between 50 nm - 500 nm whereas their thickness varies from 5 nm to 10 nm. This indicates a requirement for planarization of the samples before further processing of nanostructures on the surface. Although, MFM amplitude images show lower contrast than the topography images, it is still possible to observe the magnetic domain stripes at zero field. The difference of contrast in amplitude measurements indicates opposing magnetic moments. Their magnetic images show that the domain stripes are very narrow and diminishing locally on the film surface of M3, whereas broad domain stripes are observed on the M6 surface. Phase modulation images show no contrast in the regional cross sections of both samples. Since the tip of the MFM is directing towards the z-direction with a lift offset, it is more likely to sense the magnetic field gradient originated from the z-direction oriented magnetic domains. The lack of contrast in the phase modulation implies that the magnetic spins reside in the in-plane direction.[66] However, it is very hard to observe phase contrast on an ultra-thin magnetic

film when the film thickness is below a threshold value. Therefore, the film thickness must be thick enough for the formation of magnetic domains parallel to the film surface.[67]

After the confirmation of a magnetic response from MFM measurements, vibrating sample magnetometry measurements are carried out to investigate temperature dependence of magnetic characteristics of the multiphase iron oxide thin films. Due to the base temperature of the system at 10 K, it was not possible to observe the diamagnetic behavior and critical fields of niobium due to its superconductive transition temperature (T_c < 9 K). Yet, it is possible to observe Verwey transition for iron oxide thin films (T_V ~ 120 K).

As explained in the experiment part, MH loops are obtained at first to observe the saturation magnetizations, where three MH curves are recorded for each sample at 300 K, 150 K and 10 K respectively. Each MH measurement is followed by FC magnetotransport measurements with decreasing temperatures at the field point where the sample magnetization is saturated. Therefore, magnetization of the samples are measured with constant uniform magnetic fields sufficiently magnetizing the sample from 300 K to 10 K.

Figure 39 depicts the MH loops (top) and the MT behaviors (bottom) of the Fe-O thin films measured by VSM. The MH scan of every heated sample exhibits a hysteresis loop with a different saturated magnetization as a ferrimagnetic behavior.

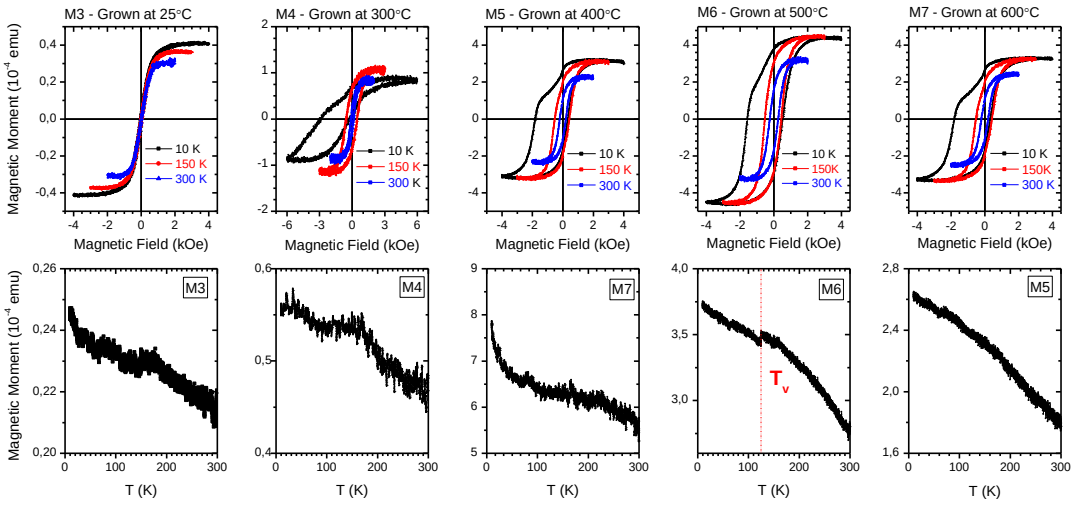

Figure 38. (top) Magnetic moment vs applied magnetic field, and (bottom) field cooling transport measurements for series of magnetite thin films

High saturation magnetizations are observed with an increasing trend under decreasing temperature, which is a ferrimagnetic characteristic of magnetite as pointed out in the literature.[68]

According to the MH loops, coercivity of iron oxide samples are asymmetric at room temperature. Total coercive fields of 150 kOe, 230 kOe, 490 kOe, 405 kOe and shifts of +5 kOe, +15 kOe, +15 kOe, +15 kOe are measured for samples M4, M5, M6, and M7 respectively. Also, overall coercivity and skewness increase with decreasing measurement temperatures, which is consistent with the inhomogeneity of magnetic moment distribution obtained from MFM results.[69]

With the highest saturation magnetization and coercivity, sample M6 demonstrated a discrete drop in magnetic moment at 125 K which is observed in the magneto-transport measurements. It is an indication of Verwey transition for magnetite.[70] This result was expected and it is consistent with the Raman spectroscopy and XRD results of M6 in a rough sense, where it is the best match with magnetite fingerprint Raman spectrum in comparison with the other samples, and it shows two main crystal orientations of magnetite and maghemite. Anti-phase boundaries in the crystal structure or strain on thin films may suppress Tv, which may be the case for the other iron oxide samples where Verwey transition is not observed, assuming that during the FC, the sample was properly magnetized.[71,72]

Although we observed the Verwey transition of the grown sample with 500 ^{O}C in-situ heat treatment, the weak links of the coplanar junctions are grown at room temperature, avoiding the unwanted oxidation of superconducting niobium. Furthermore, liftoff protocol is applied throughout the fabrication of the junction, where the first superconducting electrode and iron oxide with the second electrode are deposited in different processes in order. Therefore, applying heat treatment to the weak link results in the post-annealing of the bottom electrode, which may lead to structural changes in the superconducting isles, which is also avoided.

After VSM measurements, electrical transport measurements are carried out for sample M6. The resistance of the sample is measured by using 4-point contact and applying 100 μA direct current with decreasing temperature down to 5 K. The results are presented in Figure 40.

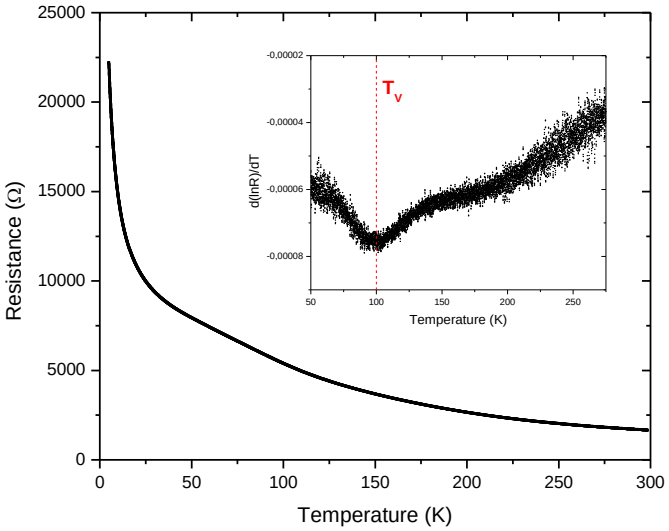

Figure 39. Resistance vs temperature behavior of magnetite sample M6 with logarithmic derivative on the inset

The sharp increase in resistance is as expected behavior for magnetite due to the Verwey transition. By calculating and visualizing the logarithmic derivative, transition temperature is obtained, which broadly shows around 100 K. It is challenging to identify the exact reason behind the slight discrepancy between MT and RT results, since the VSM samples and the main samples are deposited on different substrates at the same processes and the samples for the transport measurement are diced from 1 x 1 cm^2 dies into 2 mm x 5 mm pieces after previous characterizations. Therefore, the VSM samples are measured directly after deposition while the other samples are exposed to X-rays, visible laser with high intensity, and stress from the dicing, which may be the causes of the discrepancy. Yet, transition temperatures from both measurements are in the expected temperature intervals.[73]

4.3. Characterization of Coplanar Josephson Junctions

Coplanar Josephson junctions with three different cross sectional tunneling barriers are characterized through series of transport measurements. The coplanar junctions formed

with sizes of 5 x 5 μm^2 , 2 x 2 μm^2, 0.5 x 0.5 μm^2 are labeled as CP5, CP2 and CP1 in this thesis. First, RT measurements are carried out for CP5.

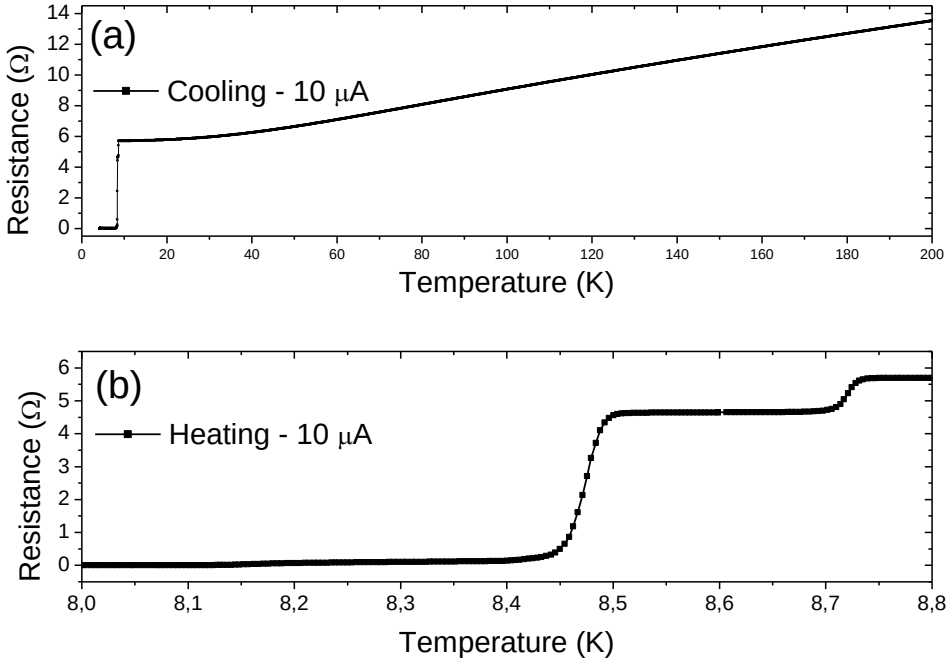

Figure 40. (a) Natural cooling R-T measurement for sample CP5. (b) Close up view of the superconducting transition of the junction

In the figure, trend from 300 K to 2 K exhibit mostly a linear decrease with lowering temperature and superconducting transition is observed below T_c , as expected from a conventional Josephson junction. Superconducting transition occurs in two gradual drops which are 8.4 K and 8.14 K due to the separate depositions of junctions which exhibit different T_c. Also, the iron oxide layer below the second electrode is capable of a minute suppression of T_c. In general, transition temperatures are in the expected interval for niobium electrodes. Transition to superconducting state does not occur at a single critical temperature point since two superconducting electrodes are deposited at different processes. Instead, there are two transition points, one around 8.72 K and one around 8.47 K leading to zero resistance. The transition temperatures are in the expected interval for niobium electrodes.

Following the RT measurements, current-voltage characteristics are obtained for CP5 at different temperatures. The combined graph is illustrated below in Figure 42.

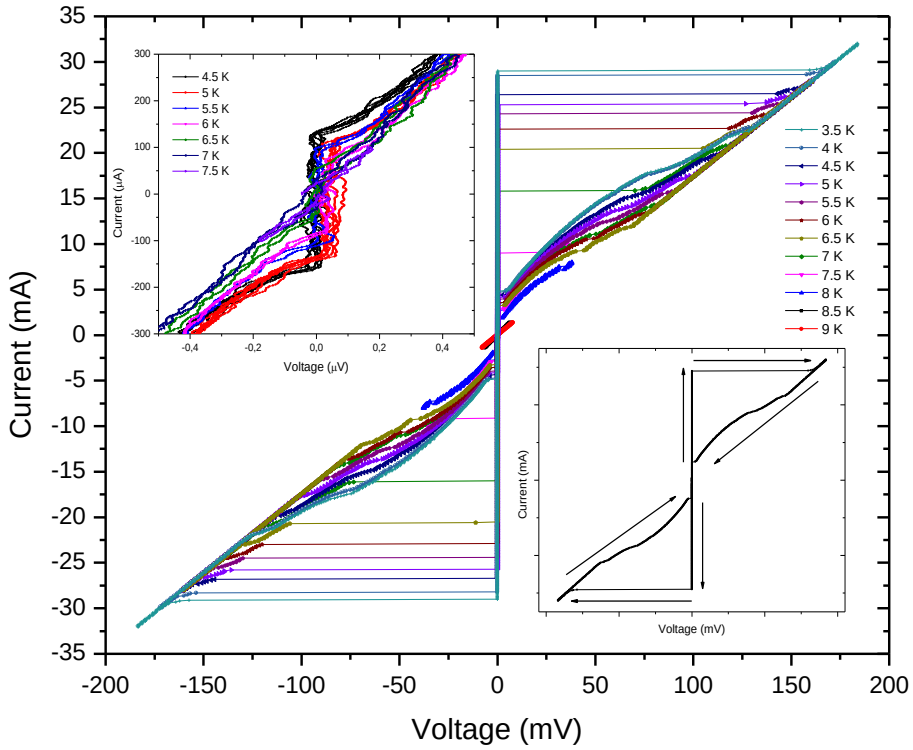

Figure 41. IV characteristics of CP5 at different temperatures. Bottom right inset shows the direction of applied current during the measurement. Top left inset shows the close scale branching to finite voltage state

First observation was the underdamped behavior of the junction with a large hysteresis and high and subgap resistance. The parameters of the measurements are also obtained and presented in Table 4.

Table 4. Characteristic parameters of CP5 obtained from IV curves

CP5 5 μm x 5 μm					
Temperature (K)	V_g (mV)	I_C (mA)	I_R (mA)	I_{SW} (μA)	R_N (Ω)
3.5	159.58	29.05	4.85	-	5.6
4	157.82	28.55	4.75	-	5.48
4.5	142.76	26.46	4.38	140	5.52
5	137.31	25.36	4.14	105	5.39
5.5	130.12	24.35	3.95	100	5.33
6	118.27	22.65	3.55	69	5.21
6.5	104.89	20.44	3.25	52	5.12
7	70.27	15.86	3.24	11.31	4.41

The low current branching at the current I_{Sw} is called premature switching, which is caused by thermal quantum fluctuations.[74] At lower temperatures, the gap between I_{Sw} and I_C close, but at temperatures close to the critical temperature, the switching current decreases dramatically, which is consistent with the underdamped RCSJ model. The critical currents are relatively high for the junction, which is expected since the tunneling occurs from 4 different interfaces with a wide cross section on top.

Gap voltage is another property of the junction, which is reciprocally related with the gap energy. At 4 K the gap energy is 79.8 meV for sample CP5, which is three times the average kinetic energy of one particle at room temperature.

As it was mentioned briefly, there is a non-linear behavior and jumps in the recombination part of the IV curve which corresponds to the subgap resistance R_{Sg}, where the non-linearity is attributed to Joule heating due to switching to the finite voltage state at the critical current and the non-linear cooling afterwards during the recombination. The jumps may indicate a shift in the Josephson ground state between 0 and π states, but it is more likely that they occur by the three different covered tunneling regions. A geometric inhomogeneity may occur from the conformality of sputtering and resolution of EBL, leading to different thicknesses of superconducting topping in different tunneling layers. Also the tunneling layer thickness is not the same for the top and sides of the junction. Therefore, the jumps are attributed to the inhomogeneity [75]

In order to see the effects of Joule heating, temperature and resistive switching are recorded over time while applying the current sweep and the results are presented in Figure 43.

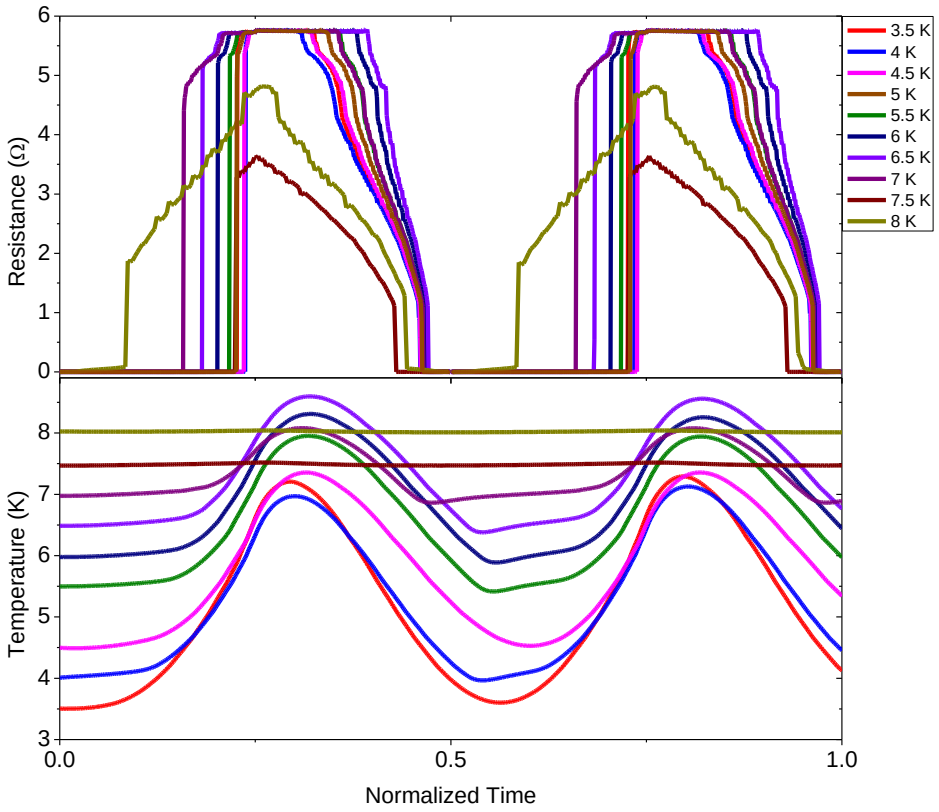

Figure 42. Temperature and resistance plots over normalized time

The time is normalized over the timestamps of the data acquisition, since the incrementation and sweep ranges may differ for varying temperature setpoints. Intense Joule heating is observed on the junction, which is at its maximum for the measurement taken at 3.5 K. During the positive sweep, the sample space was heated from 3.5 K up to 7 K, which is due to premature switching.

After the Joule heating measurements, the supercurrent-temperature relationship is investigated. The critical currents at different temperatures are plotted and illustrated in Figure 44.

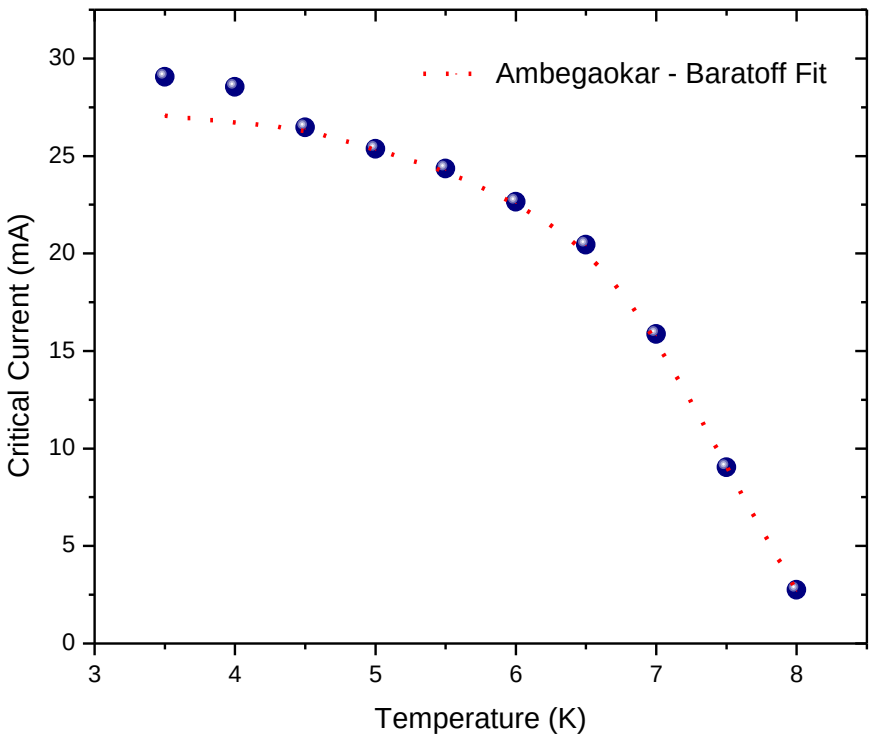

Figure 43. Critical currents vs temperature for different temperatures and Ambegaokar-Baratoff relation for the junction

AB relation is the governing relationship used at high thermal energies where the average kinetic energy due to temperature dominates the Josephson energy. Also, the relationship works well for conducting weak links, but an ordinary behavior is not expected for a ferromagnetic junction.

At most part, the junction behavior is consistent with the AB relation. However, there is an unexpected increase for the measurements at 4 K and 3.5 K, which might be due to the ferromagnetic tunneling layer, where sudden jumps in the $I_C R_N$ is observed in supercurrent induced ferromagnetic thin films.[76] High critical current values also result in high $I_C R_N$ values where at 4 K $I_C R_N = 156.5\, mV$, which indicates a good tunneling barrier. For a single superconductor, $I_C R_N$ product is invariant and independent of the junction geometry where the critical current and normal resistance are related reciprocally by the tunneling area.

After the measurements of sample CP5 are completed, the same measurements are repeated for sample CP2. The change in resistance with decreasing temperature for the junction is represented below in Figure 45.

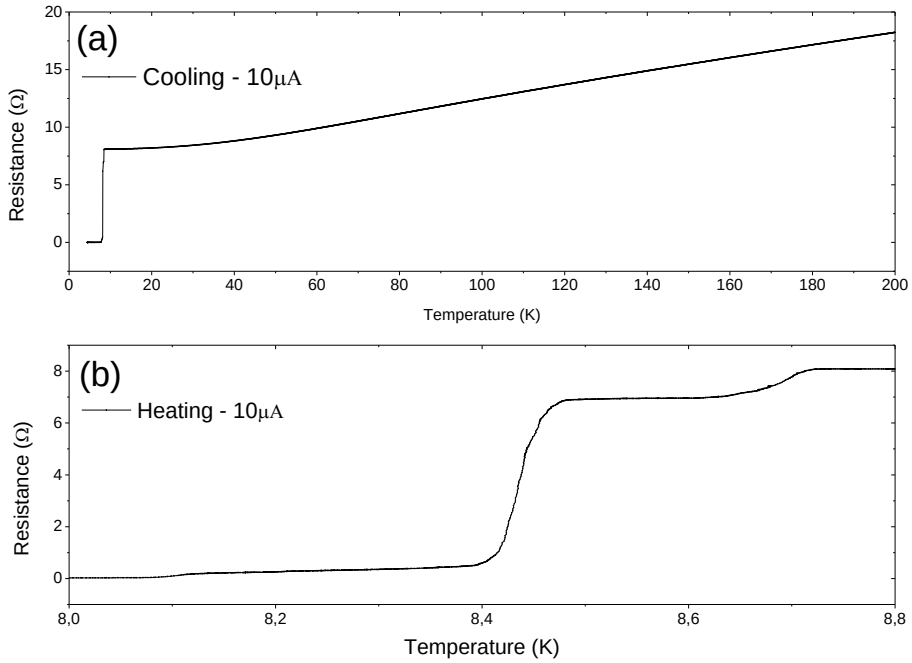

Figure 44. (a) R-T measurements for CP2 from 200 K to base temperature. (b) Close up to the transition temperatures

The room temperature resistance and overall resistance of the junction is higher than the resistance observed on CP5 as expected since the resistance increases with decreasing cross section of the path taken. Since all of the first and second electrodes are deposited at the same time for all junctions in two processes in sequence, the two transition temperatures are the same for all junctions, which is expected. The width of both transitions is broader in comparison with the results for CP5. For this sample, the actual zero voltage state is observed at 7.5 K.

Moving on to the tunneling characteristics, again the IV measurements are carried out for the sample. The results are given in Figure 46.

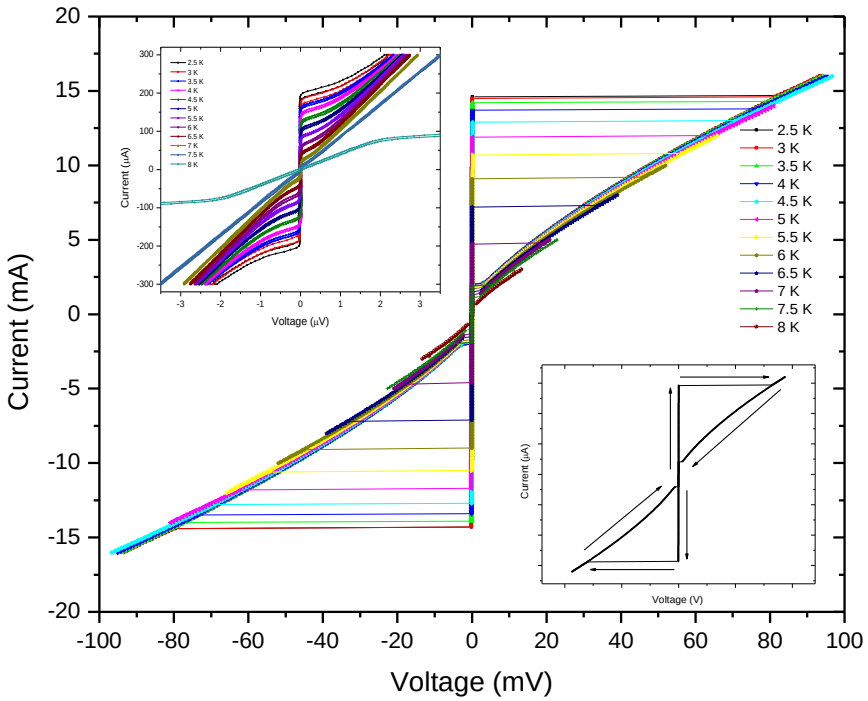

Figure 45. IV curves of CP5 at different temperature setpoints with premature switching measurements and current biasing directions at the insets

In contrast with sample CP5, the recombination behavior of the junction is more stable. Yet, there is still a dominant quasiparticle tunneling which prevents the formation of Cooper pairs while decreasing the current in the finite voltage state. The critical currents and other characteristics obtained from the measurement are presented in Table 5 below.

Table 5. Measured underdamped tunneling characteristics of sample CP2

	CP2 2 μm x 2 μm				
Temperature (K)	V_g (mV)	I_C (mA)	I_R (mA)	I_{SW} (μA)	R_N (Ω)
2.5	82.03	14.67	2.04	201.15	5.57
3	81.1	14.58	2.06	185.43	5.55
3.5	79.5	14.26	2.04	167.43	5.56
4	75.98	13.75	2.05	150.65	5.51
4.5	70.56	12.92	1.97	129.5	5.43
5	63.95	11.99	1.94	111.68	5.32
5.5	56.18	10.75	1.85	89.48	5.20
6	45.71	9.15	1.75	64.14	4.97
6.5	33.9	7.25	1.55	44.2	4.64
7	19.55	4.75	1.35	25.17	4.07
7.5	5.69	1.95	1.15	12.58	2.84
8	1.59	0.75	0.73	-	1.96

Lower critical current values and gap energies are observed in comparison to sample CP5, which is expected from a smaller tunneling cross-section. Still, at 4 K, the $I_C R_N = 75.8\,mV$ for CP2, which is above the quality criteria. Normal state resistances and recombination currents are close to the results of CP5. The decrease in critical current is also expected for sample CP1.

For investigating the occurrence of Joule heating with changing tunneling cross-section, individual resistance and temperature measurements are carried out during the IV sweeps. Their combined results for sample CP2 are illustrated in Figure 47 below.

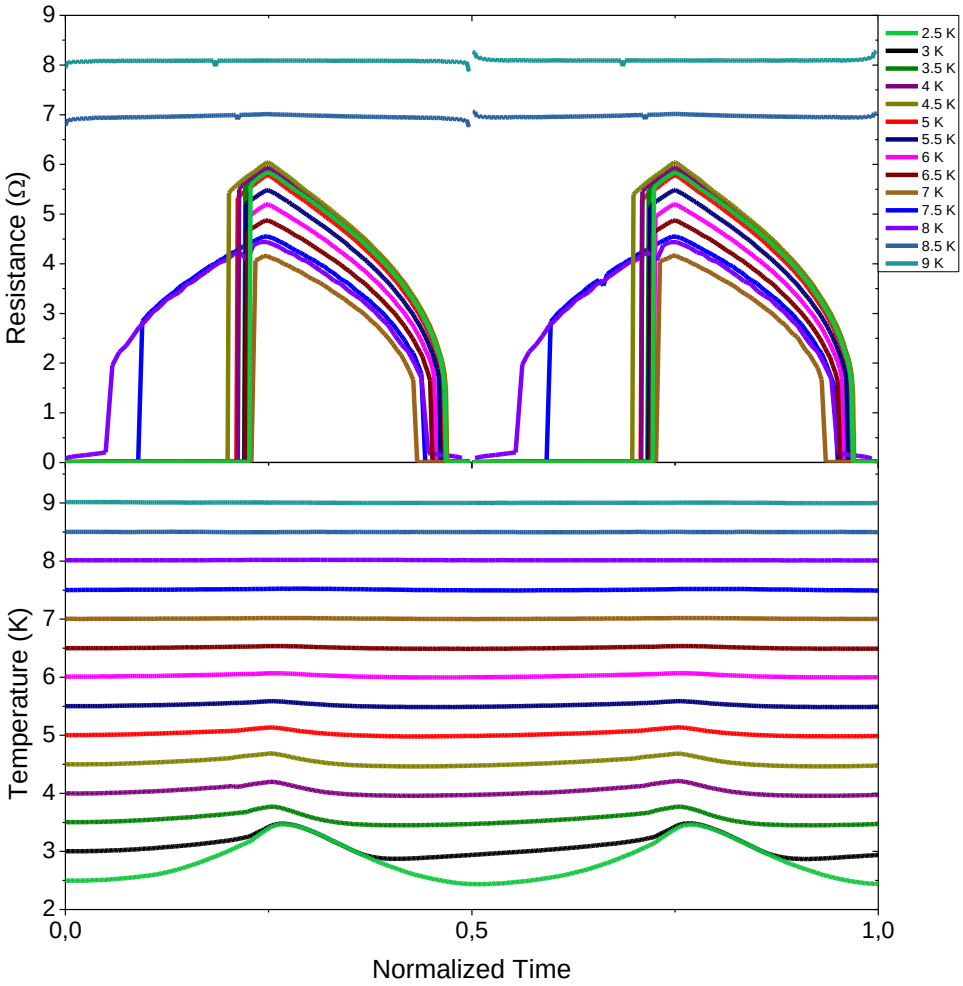

Figure 46. Joule heating on the sample CP2 during direct current sweep

Joule heating is observed at low temperature setpoints, where above 5 K, very minute temperature increases observed in mK orders. This shows that for this geometry,

smaller cross sections for the junctions will result in less Joule heating during current biasing. This is an important finding, since in order to develop further applications on a junction such as storing or processing information in sub-Kelvin temperatures, an understanding of the effects of Joule heating is crucial. It is also possible to directly observe that the normal state resistance R and the finite voltage state resistance R_N is not the same for a junction.

AB relation is investigated for CP2, and the results are presented in Figure 48 below.

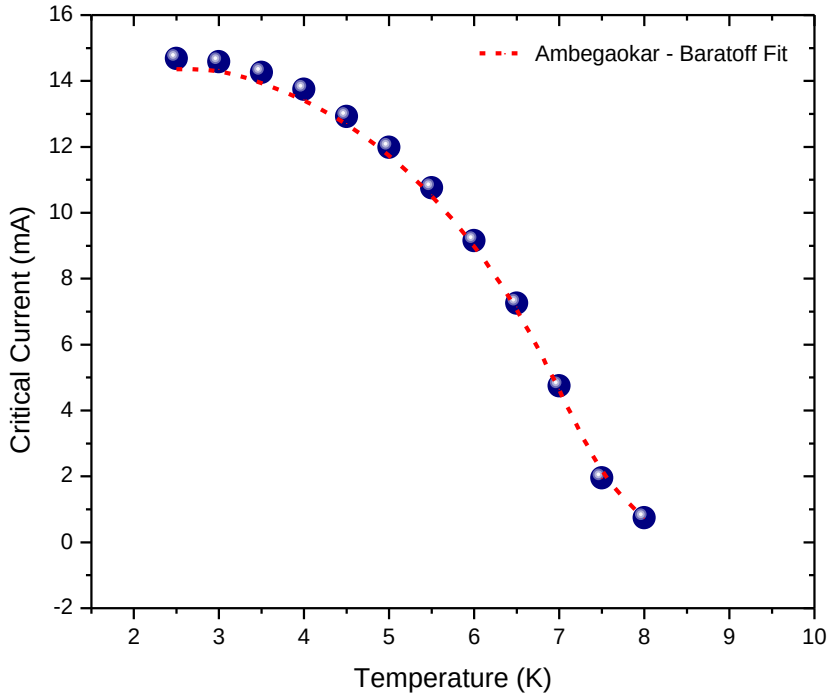

Figure 47. Critical current vs temperature data and Ambegaokar-Baratoff relation for sample CP2

The data shows good correlation with the supercurrent – temperature relationship. Yet, there is no indication of a ferromagnetic weak link from AB data of CP2. For an insulating barrier, this relationship is skewed into a more linear trend, where for a normal metal weak link, the tangent hyperbolic behavior is preserved. From this point of view, the tunneling barrier shows normal metal behavior rather than an insulator.

After the measurements are completed at different temperatures, the sample is fixed to 4 K by using a PID controller, and critical current modulations are investigated under applied magnetic field. The field is applied perpendicular to the substrate plane from the covered side of the junction. The results are shown in Figure 49.

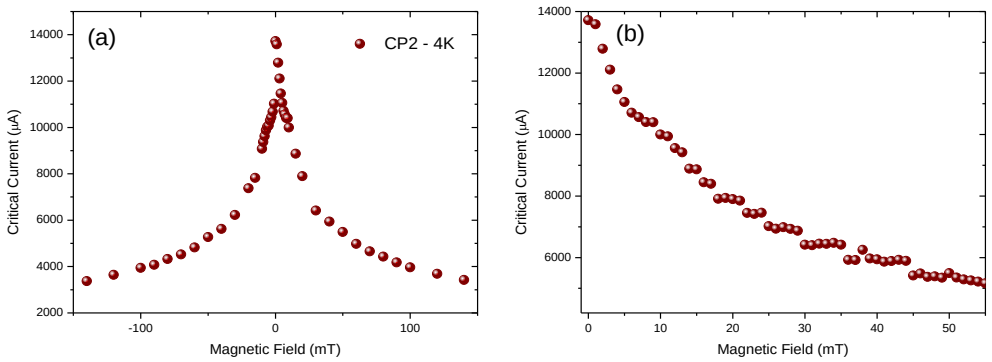

Figure 48. Critical currents at different magnetic fields for sample CP2 at 4 K. (a) magnetic sweep from -150 mT to 150 mT, (b) magnetic sweep with low incrementation from 0 mT to 55 mT

The magnetic sweep on the left side shows that the diffraction pattern is suppressed resulting with a single peak, yet traces of the suppressed modulation are observed from the data with 1 mT increments. The results are in agreement with the reported results for inhomogeneous ferromagnetic/ferrimagnetic Josephson junctions where a single diffraction peak is observed and the oscillation pattern is supressed.[77] This behavior is associated with trapped Abrikosov vortices inside the Josephson junction, influencing an anomalous phase shift of the Josephson junction, which is the aim of this fabrication. Moreover, for square shaped Josephson junctions with lateral geometry and inhomogeneous ferromagnetic weak links, the single suppressed peak is observed to be sharp where the critical current decreases rapidly with increasing magnetic field.[78,79]

After the magnetic field measurement of sample CP2, transport measurements are carried out for the last sample CP1. First, results for resistance at different temperatures are given in Figure 50.

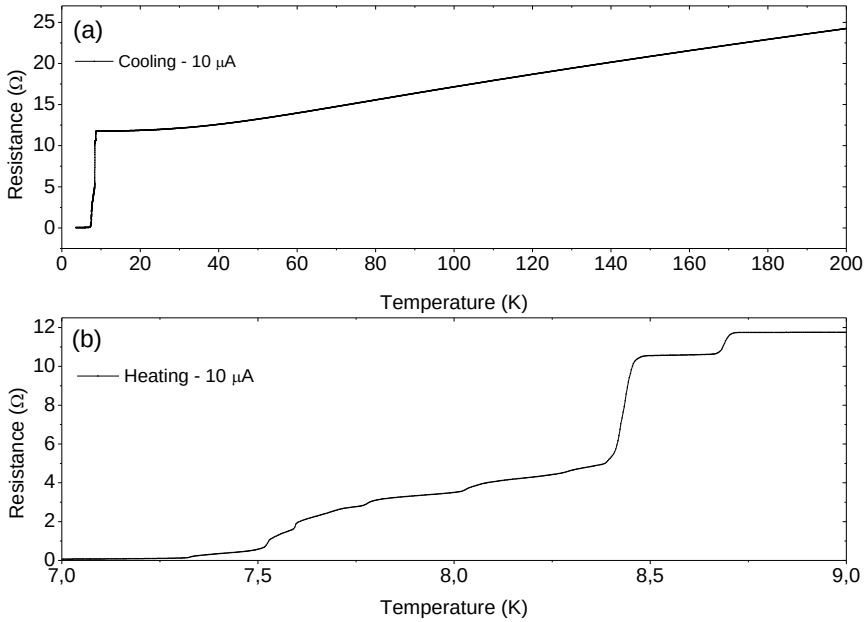

Figure 49. (a) Resistance vs temperature plots for junction CP1, (b) close up to the transition

The transition of CP1 to superconductivity is not as smooth as CP2 and CP5, where the second transition for larger electrode has a very broad width around 1 K, where the full transition occurs at 7.25 K. The resembling part is that if we look closer to the transition of sample CP2, this broad transition region between 7.25 K and 8.4 K is also there, but with much lower resistance. For comparison, the close up transitions of sample CP2 is represented in Figure 51.

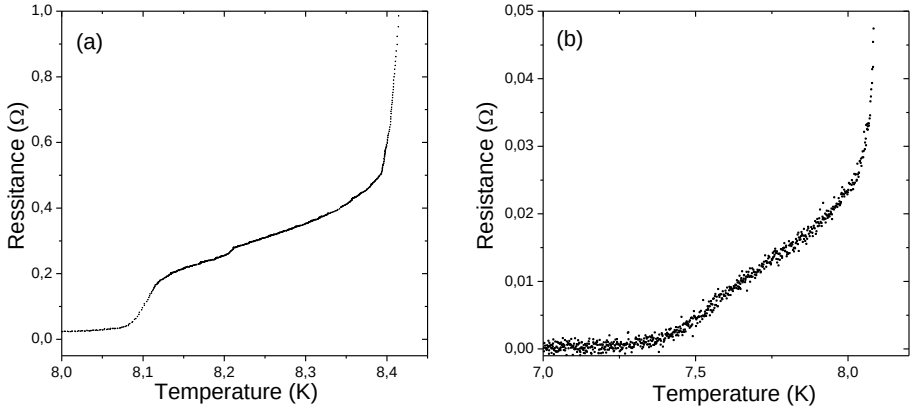

Figure 50. (a) Transition of CP2 to superconductivity between 8 K and 8.4 K. (b) Close up transition of CP2 at 7.25 K to absolute zero-voltage state

This shows that resistive shunting of the junction increases with decreasing tunneling area, which is reasonable.

After the RT measurements, IV curves are obtained for sample CP1, and presented below in Figure 52.

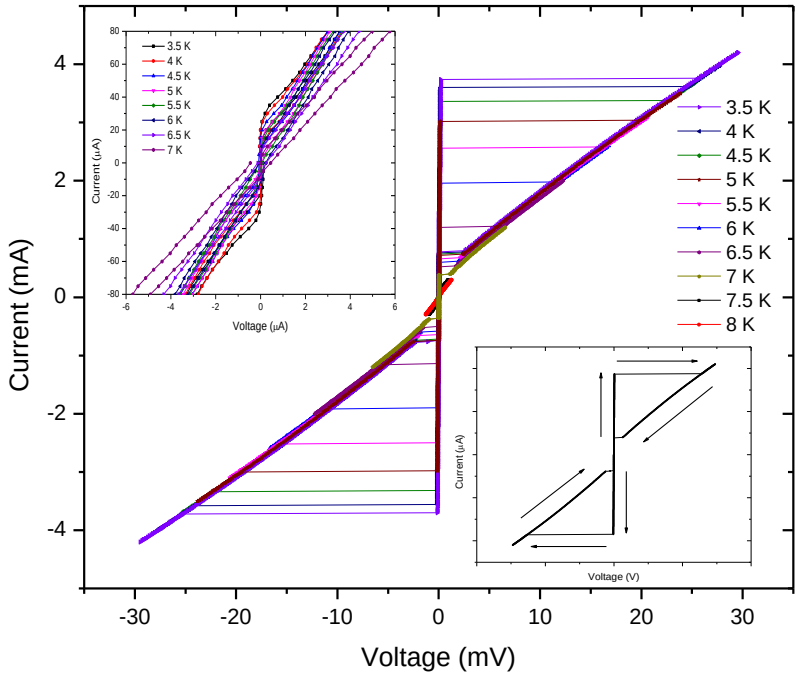

Figure 51. Current-voltage characteristics of junction CP1. Insets show low voltage branching at top left and sweep directions at bottom right inset

Very smooth superconductive recombination trends are observed with $R_N = R_{Sg}$, with large hysteresis at each temperature setpoint. The parameters obtained from the current-voltage sweeps are given in Table 6.

Table 6. Characteristic parameters of sample CP1 obtained from I-V plots

CP1 1 µm x 1 µm					
Temperature (K)	V_g (mV)	I_C (mA)	I_R (mA)	I_{Sw} (µA)	R_N (Ω)
3.5	25.62	3.75	0.8	29.75	6.84
4	24.60	3.61	0.78	27.13	6.76
4.5	22.57	3.37	0.76	22.89	6.69
5	19.74	3.03	0.74	18.43	6.55
5.5	16.11	2.57	0.68	18.18	6.34
6	11.40	1.97	0.62	14.46	5.98
6.5	5.47	1.21	0.54	11.84	5.22
7	1.14	0.4	0.4	11.31	2.85

The decrease of critical current values is as expected for smaller tunneling cross section compared to sample CP2. At 4 K, sample CP1 has a gap energy of 12.3 meV, which is 5-6 times lower than the gap energy of sample CP5, which was also expected. At 4 K the normal state resistance of 6.7 Ω gives us the product $I_C R_N = 24.4\, mV$ which is still above the quality criteria without an excess current.

The resistive switching and corresponding heating were recorded for sample CP1 and illustrated below in Figure 53.

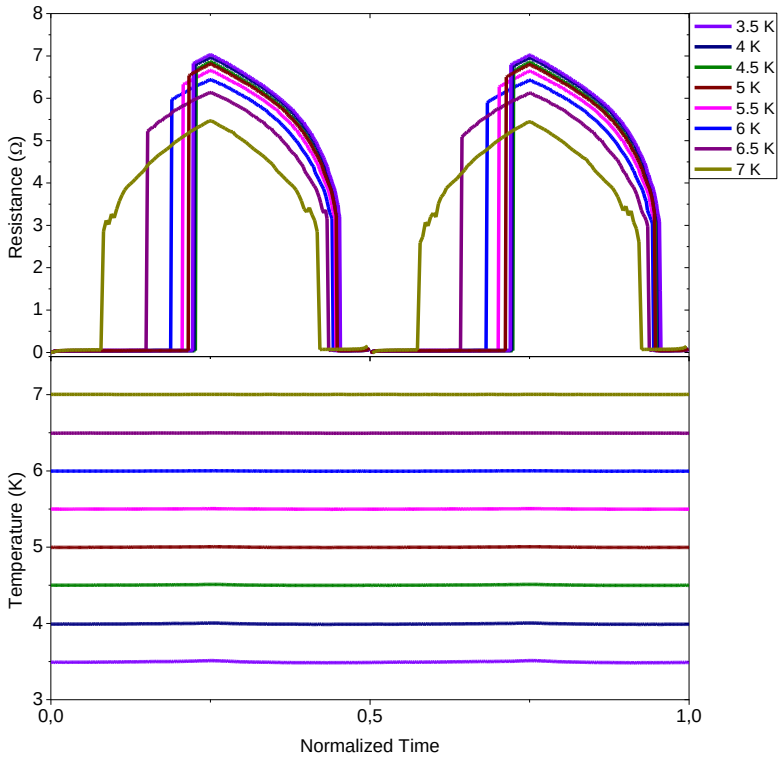

Figure 52. Resistive switching during the current sweep and corresponding temperature change for sample CP1

As expected, with decreasing tunneling cross section, the heating on the junction is decreased where for sample CP1, no heating above 5 mK was observed. For this geometry and material choice, the largest tunneling area for further applications of this Josephson junction must be designated as 1 µm x 1 µm.

Following the heating measurements, Ambegaokar Baratoff relation was investigated for the junction. The results are presented below in Figure 54.

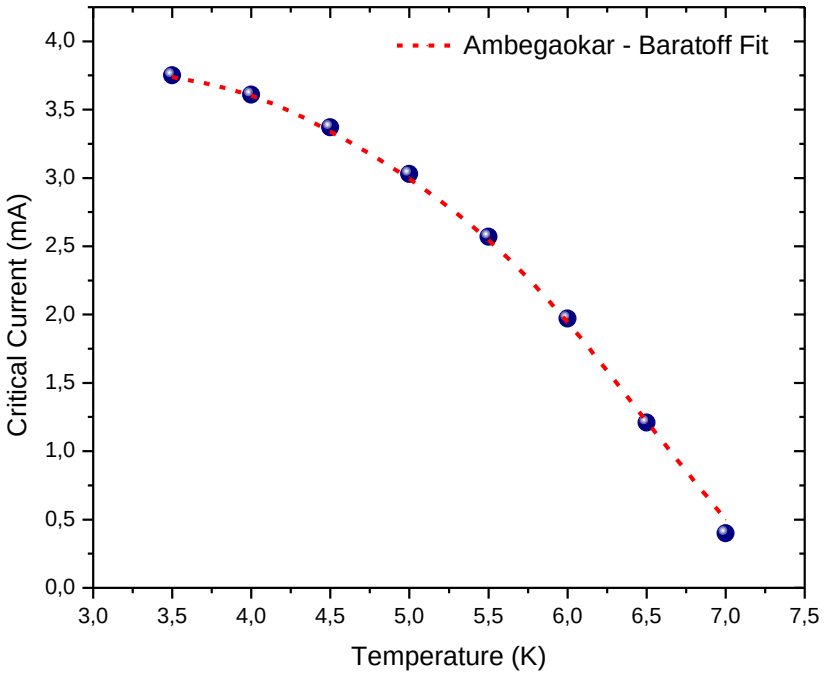

Figure 53. Critical current vs temperature data of CP1 with Ambegaokar-Baratoff trend for the junction

The change in critical current with decreasing temperature evolves into a more linear trend with decreasing tunneling area, yielding the critical current of 4.1 mA at absolute temperature. The trend is in good agreement with AB relation.

5. CONCLUSION

In this study, the sputtering conditions of niobium and iron oxide films and the fabrication steps have been extensively studied to realize coplanar ferromagnetic Josephson junctions. In a series of film growth experiments, the sputtering conditions were optimized in agreement with their structural and electrical/magnetic characteristics individually analyzed by XRD, Raman spectrometry, VSM and in plane transport measurements. Ideal growth condition for each thin film deposition were employed to form sandwiched layers of coplanar Josephson junctions. In the out-of-plane transport measurements of the coplanar junctions, some prerequisite signatures have been systematically investigated through their temperature and external magnetic field dependent properties such as I_cR_N product, and Fraunhofer patterns. While concluding, it is understood that realization of high quality FJJ requires delicacy in many different aspects.

First the quality of each thin film through a series of growth and fabrication processes and interface quality in the coplanar Josephson stacks become crucial in the realization of π-junctions. Every condition in these processes directly alter the thin film structure, electrical/magnetic characteristics and ultimately junction quality. In other words, these characteristics are very sensitive to both growth and fabrication conditions. For instance, the superconducting properties of niobium films can be gradually suppressed in case of any deviation from ideal bulk crystalline structure and/or the presence of any impurities/oxides in the the growth and fabrication processes. Characterization results show that T_c of Nb films gradually approaches to the optimum value of bulk Nb (T_c ~ 9.2 K) beyond a certain crystalline size threshold, which is correlated with the coherence length. Below this threshold, the critical temperature drastically decrease, which is well-known as the Anderson limit. The optimization studies exhibit that the crystalline size of Nb films can be tuned by changing the sputtering parameters.

Also, the quality of the ferromagnetic weak link is extremely important as another aspect, where any deviation in stoichiometry and/or strain occurring in the Fe-O film structure can induce significant changes in the magnetite characteristics such as metal-

insulator Verwey transition, and ferromagnetic behavior. Therefore, any change in the structure and stoichiometry may drastically alter the tunneling behavior of the junction. In addition to the growth experiments at room temperature, in-situ heat treatment was used as another parameter to achieve desired homogeneous magnetite characteristics in the Fe-O films. Expected magnetite characteristics have been successfully attained in Fe-O films deposited at 500 °C verified by Raman spectrometry, VSM and in-plane transport measurements. However, the sputtering condition was not used in the deposition of Fe-O layer of the coplanar junction due to oxygen affinity of Nb at high temperatures. One of the challenges was to achieve the low temperature magnetite characteristic in ultra-thin Fe-O films, where low growth rate of Fe-O films on periclase substrates resulted in ultra-thin films of 35 nm, disabling easy stoichiometric characterization options like electron dispersive X-ray spectrometry. Another challenge was the overlappings of magnetite and maghemite peaks in the X-ray diffraction. Due to these challenges, the first identification of Fe-O films were confirmed by Raman spectrometry.

Another aspect is the size and geometry. With changing dimensions and geometry, tunneling characteristics are changed for a junction where tunneling area is an important variable for a Josephson junction. For quantum computation applications, small junction sizes are more desirable due to low Joule heating and to achieve homogeneous Cooper pair tunneling across the ferromagnetic layer beyond the Coulomb blockade.

In the characterization of Josephson junctions, the challenge was to observe the ferromagnetic behavior of a 6 nm ferromagnetic insulator weak link, in order to achieve the 0-π transition. For all samples, the I_cR_N products shows conventional behaviors with changing temperature, obeying the Ambegaokar – Baratoff relation. Discrete jumps in the superconductive recombination of current-voltage characteristics are observed for sample CP5, yet these jumps are attributed to the 4 different inhomogeneous tunneling regions rather than the ground state phase shift. Aditionally, critical current modulation under magnetic field is measured for sample CP2. An expected unconventional Fraunhoffer pattern is recorded where the interference oscillations are supressed due to the ferromagnetic weak link. These findings indicates the achievement of a ferromagnetic weak link, but the ground state shift of the Josephson phase is unconfirmed.

6. REFERENCES

1. Jaklevic, R. C., Lambe, J., Silver, A. H. & Mercereau, J. E. Quantum Interference Effects in Josephson Tunneling. *Phys. Rev. Lett.* **12**, 159–160 (1964).

2. Lee, G.-H. *et al.* Graphene-based Josephson junction microwave bolometer. *Nature* **586**, 42–46 (2020).

3. Kleiner, R. & Wang, H. Terahertz emission from Bi 2 Sr 2 CaCu 2 O 8+ x intrinsic Josephson junction stacks. *J. Appl. Phys.* **126**, 171101 (2019).

4. Satchell, N. *et al.* Spin-valve Josephson junctions with perpendicular magnetic anisotropy for cryogenic memory. *Appl. Phys. Lett.* **116**, (2020).

5. Yamashita, T., Tanikawa, K., Takahashi, S. & Maekawa, S. Superconducting <math display="inline"> <mi>π</mi> </math> Qubit with a Ferromagnetic Josephson Junction. *Phys. Rev. Lett.* **95**, 097001 (2005).

6. Eschrig, M. Spin-polarized supercurrents for spintronics: a review of current progress. *Reports Prog. Phys.* **78**, (2015).

7. Iovan, A. & Krasnov, V. M. Signatures of the spin-triplet current in a Josephson spin valve: A micromagnetic analysis. *Phys. Rev. B* **96**, 014511 (2017).

8. Linder, J. & Robinson, J. W. A. Superconducting spintronics. *Nat. Phys.* **11**, 307–315 (2015).

9. Baek, B., Rippard, W. H., Benz, S. P., Russek, S. E. & Dresselhaus, P. D. Hybrid superconducting-magnetic memory device using competing order parameters. *Nat. Commun.* **5**, 3888 (2014).

10. Ryazanov, V. V. *et al.* Magnetic Josephson Junction Technology for Digital and Memory Applications. *Phys. Procedia* **36**, 35–41 (2012).

11. Dayton, I. M. *et al.* Experimental Demonstration of a Josephson Magnetic Memory Cell With a Programmable π-Junction. *IEEE Magn. Lett.* **9**, 1–5 (2018).

12. Frolov, S. M. *et al.* Imaging spontaneous currents in superconducting arrays of π-junctions. *Nat. Phys.* **4**, 32–36 (2008).

13. Feofanov, A. K. *et al.* Implementation of superconductor/ferromagnet/ superconductor π-shifters in superconducting digital and quantum circuits. *Nat. Phys.* **6**, 593–597 (2010).

14. Vernik, I. V. *et al.* Magnetic Josephson Junctions With Superconducting Interlayer for Cryogenic Memory. *IEEE Trans. Appl. Supercond.* **23**, 1701208–1701208 (2013).

15. Madden, A. E., Naaman, O. & Birge, N. Ferromagnetic Josephson junctions for cryogenic memory. in *Spintronics XI* (eds. Jaffrès, H., Drouhin, H.-J., Wegrowe, J.-E. & Razeghi, M.) 57 (SPIE, 2018). doi:10.1117/12.2321109.

16. Kawabata, S., Asano, Y., Tanaka, Y., Golubov, A. A. & Kashiwaya, S. Josephson <math display="inline"> <mi>π</mi> </math> State in a Ferromagnetic Insulator. *Phys. Rev. Lett.* **104**, 117002 (2010).

17. Tanaka, Y. & Kashiwaya, S. Theory of Josephson effect and current carrying quasiparticle states in d-wave superconductors. *Phys. C Supercond.* **293**, 101–104 (1997).

18. Kawabata, S., Ozaeta, A., Vasenko, A. S., Hekking, F. W. J. & Sebastián Bergeret, F. Efficient electron refrigeration using superconductor/spin-filter devices. *Appl. Phys. Lett.* **103**, (2013).

19. Wang, X., Liao, Y., Zhang, D., Wen, T. & Zhong, Z. A review of Fe3O4 thin films: Synthesis, modification and applications. *J. Mater. Sci. Technol.* **34**, 1259–1272 (2018).

20. van Delft, D. & Kes, P. The discovery of superconductivity. *Phys. Today* **63**, 38–43 (2010).

21. Meissner, W. & Ochsenfeld, R. Ein neuer Effekt bei Eintritt der Supraleitf﷿higkeit. *Naturwissenschaften* **21**, 787–788 (1933).

22. London, Fritz; London, H. The electromagnetic equations of the supraconductor. *Proc. R. Soc. London. Ser. A - Math. Phys. Sci.* **149**, 71–88 (1935).

23. Maxfield, B. W. & McLean, W. L. Superconducting Penetration Depth of Niobium. *Phys. Rev.* **139**, A1515–A1522 (1965).

24. Ginzburg, V. L. On Superconductivity and Superfluidity (What I Have and Have Not Managed to Do), as well as on the‘Physical Minimum’ at the Beginning of the 21st Century. *ChemPhysChem* **5**, 930–945 (2004).

25. Gor’kov, L. P. Microscopic Derivation of the Ginzburg-Landau Equations in the Theory of Superconductivity. *Sov. Phys. JETP* **36**, 1364–1367 (1959).

26. Abrikosov, A. Magnetic properties of superconductors of the second group. *J. Exp. Theor. Phys.* (1956).

27. Maxwell, E. The isotope effect in superconductivity. *Phys. Today* **5**, 14–18 (1952).

28. Bardeen, J., Cooper, L. N. & Schrieffer, J. R. Microscopic Theory of Superconductivity. *Phys. Rev.* **106**, 162–164 (1957).

29. Bogoljubov, N. N. On a new method in the theory of superconductivity. *Nuovo Cim.* **7**, 794–805 (1958).

30. Josephson, B. D. Possible new effects in superconductive tunnelling. *Phys. Lett.* **1**, 251–253 (1962).

31. Hibbs, Albert R., Feynman, R. P. *Quantum Mechanics and Path Integrals*. (Dover Publications, 1965).

32. Anderson, P. W. & Rowell, J. M. Probable Observation of the Josephson Superconducting Tunneling Effect. *Phys. Rev. Lett.* **10**, 230–232 (1963).

33. Andreev, A. F. Thermal Conductivity of the Intermediate State of

Superconductors. *JETP Lett.* **46**, 1823–1828 (1964).

34. Eschrig, M. Theory of Andreev bound states in S-F-S junctions and S-F proximity devices. *Philos. Trans. R. Soc. A Math. Phys. Eng. Sci.* **376**, 20150149 (2018).

35. Kawabata, S., Tanaka, Y., Golubov, A. A., Vasenko, A. S. & Asano, Y. Spectrum of Andreev bound states in Josephson junctions with a ferromagnetic insulator. *J. Magn. Magn. Mater.* **324**, 3467–3470 (2012).

36. Prada, E. *et al.* From Andreev to Majorana bound states in hybrid superconductor–semiconductor nanowires. *Nat. Rev. Phys.* **2**, 575–594 (2020).

37. Ambegaokar, V. & Baratoff, A. Tunneling Between Superconductors. *Phys. Rev. Lett.* **10**, 486–489 (1963).

38. Stewart, W. C. CURRENT-VOLTAGE CHARACTERISTICS OF JOSEPHSON JUNCTIONS. *Appl. Phys. Lett.* **12**, 277–280 (1968).

39. Kapran, O. M., Iovan, A., Golod, T. & Krasnov, V. M. Observation of the dominant spin-triplet supercurrent in Josephson spin valves with strong Ni ferromagnets. *Phys. Rev. Res.* **2**, 013167 (2020).

40. Fermin, R. *et al.* Superconducting Triplet Rim Currents in a Spin-Textured Ferromagnetic Disk. *Nano Lett.* **22**, 2209–2216 (2022).

41. Khasawneh, M. A., Khaire, T. S., Klose, C., Pratt Jr, W. P. & Birge, N. O. Spin-triplet supercurrent in Co-based Josephson junctions. *Supercond. Sci. Technol.* **24**, 024005 (2011).

42. Iovan, A., Golod, T. & Krasnov, V. M. Controllable generation of a spin-triplet supercurrent in a Josephson spin valve. *Phys. Rev. B* **90**, 134514 (2014).

43. Ryazanov, V. V. *et al.* Coupling of Two Superconductors through a Ferromagnet: Evidence for a <math display="inline"> <mi>π</mi> </math> Junction. *Phys. Rev. Lett.* **86**, 2427–2430 (2001).

44. BRAGG, W. H. The Structure of Magnetite and the Spinels. *Nature* **95**, 561–561 (1915).

45. Kim, W. *et al.* A new method for the identification and quantification of magnetite–maghemite mixture using conventional X-ray diffraction technique. *Talanta* **94**, 348–352 (2012).

46. Néel, M. L. Propriétés magnétiques des ferrites ; ferrimagnétisme et antiferromagnétisme. *Ann. Phys. (Paris).* **12**, 137–198 (1948).

47. Kündig, W. & Steven Hargrove, R. Electron hopping in magnetite. *Solid State Commun.* **7**, 223–227 (1969).

48. Yin, H. *et al.* Controlled Synthesis of Hollow α-Fe2O3 Microspheres Assembled With Ionic Liquid for Enhanced Visible-Light Photocatalytic Activity. *Front. Chem.* **7**, (2019).

49. Zhang, Z. & Satpathy, S. Electron states, magnetism, and the Verwey transition in magnetite. *Phys. Rev. B* **44**, 13319–13331 (1991).

50. VERWEY, E. J. W. Electronic Conduction of Magnetite (Fe3O4) and its Transition Point at Low Temperatures. *Nature* **144**, 327–328 (1939).

51. Ding, J. *et al.* Growth and characterization of Fe3O4 films. *Mater. Res. Bull.* **46**, 2212–2216 (2011).

52. Wu, H.-C. *et al.* Magnetic and transport properties of epitaxial stepped Fe 3 O 4 (100) thin films. *Appl. Phys. Lett.* **105**, 132408 (2014).

53. Aubry, E. *et al.* Synthesis of iron oxide films by reactive magnetron sputtering assisted by plasma emission monitoring. *Mater. Chem. Phys.* **223**, 360–365 (2019).

54. Roeser, H. P. *et al.* Correlation between transition temperature and crystal structure of niobium, vanadium, tantalum and mercury superconductors. *Acta Astronaut.* **67**, 1333–1336 (2010).

55. Hazra, D., Mondal, M. & Gupta, A. K. Correlation between structural and superconducting properties of nano-granular disordered Nb thin films. *Phys. C Supercond.* **469**, 268–272 (2009).

56. Nivedita, L. R., Haubert, A., Battu, A. K. & Ramana, C. V. Correlation between Crystal Structure, Surface/Interface Microstructure, and Electrical Properties of Nanocrystalline Niobium Thin Films. *Nanomaterials* **10**, 1287 (2020).

57. Bose, S., Raychaudhuri, P., Banerjee, R., Vasa, P. & Ayyub, P. Mechanism of the Size Dependence of the Superconducting Transition of Nanostructured Nb. *Phys. Rev. Lett.* **95**, 147003 (2005).

58. Anderson, P. W. New Approach to the Theory of Superexchange Interactions. *Phys. Rev.* **115**, 2–13 (1959).

59. Vlaic, S. *et al.* Superconducting parity effect across the Anderson limit. *Nat. Commun.* **8**, 14549 (2017).

60. Wang, S.-S. *et al.* Low-energy (40 keV) proton irradiation of YBa 2 Cu 3 O 7− x thin films: Micro-Raman characterization and electrical transport properties. *Chinese Phys. B* **28**, 027401 (2019).

61. Zhang, J., Tan, P., Zhao, W., Lu, J. & Zhao, J. Raman study of ultrathin Fe 3 O 4 films on GaAs(001) substrate: stoichiometry, epitaxial orientation and strain. *J. Raman Spectrosc.* **42**, 1388–1391 (2011).

62. Pezzotti, G., Sueoka, H., Porporati, A. A., Manghnani, M. & Zhu, W. Raman tensor elements for wurtzitic GaN and their application to assess crystallographic orientation at film/substrate interfaces. *J. Appl. Phys.* **110**, 013527 (2011).

63. Visweswaran, S., Venkatachalapathy, R., Haris, M. & Murugesan, R. Characterization of MgO thin film prepared by spray pyrolysis technique using perfume atomizer. *J. Mater. Sci. Mater. Electron.* **31**, 14838–14850 (2020).

64. de Faria, D. L. A. & Lopes, F. N. Heated goethite and natural hematite: Can Raman spectroscopy be used to differentiate them? *Vib. Spectrosc.* **45**, 117–121 (2007).

65. Yang, Y., Zhang, Q., Mi, W. & Zhang, X. Lattice deformation in epitaxial Fe 3 O 4 films on MgO substrates studied by polarized Raman spectroscopy*. *Chinese*

Phys. B **29**, 083302 (2020).

66. Liebmann, M. *et al.* Magnetization reversal of a structurally disordered manganite thin film with perpendicular anisotropy. *Phys. Rev. B* **71**, 104431 (2005).

67. Sikora, A., Ozimek, M. & Wilczyński, W. Nanoscopic Investigation of Magnetic Thin Films by Means of Magnetic Force Microscopy Technique. *Acta Phys. Pol. A* **129**, 1226–1229 (2016).

68. Walz, F. The Verwey transition - a topical review. *J. Phys. Condens. Matter* **14**, R285–R340 (2002).

69. Liu, X. H., Liu, W. & Zhang, Z. D. Evolution of magnetic properties in the vicinity of the Verwey transition in <math> <mrow> <msub> <mi>Fe</mi> <mn>3</mn> </msub> <msub> <mi mathvariant="normal">O</mi> <mn>4</mn> </msub> </mrow> </math> thin films. *Phys. Rev. B* **96**, 094405 (2017).

70. Kallmayer, M. *et al.* Magnetic moment investigations of epitaxial magnetite thin films. *J. Appl. Phys.* **103**, 07D715 (2008).

71. Kado, T. Structural and magnetic properties of magnetite-containing epitaxial iron oxide films grown on MgO(001) substrates. *J. Appl. Phys.* **103**, (2008).

72. Eerenstein, W., Palstra, T. T. M., Hibma, T. & Celotto, S. Origin of the increased resistivity in epitaxial <math display="inline"> <mrow> <msub> <mrow> <mi mathvariant="normal">Fe</mi> </mrow> <mrow> <mn>3</mn> </mrow> </msub> </mrow> <mrow> <msub> <mrow> <mi mathvariant="normal">O</mi> </mrow> <mrow> <mn>4</mn>. *Phys. Rev. B* **66**, 201101 (2002).

73. Bohra, M., Agarwal, N. & Singh, V. A Short Review on Verwey Transition in Nanostructured Fe 3 O 4 Materials. *J. Nanomater.* **2019**, 1–18 (2019).

74. Miao, F., Bao, W., Zhang, H. & Lau, C. N. Premature switching in graphene Josephson transistors. *Solid State Commun.* **149**, 1046–1049 (2009).

75. Sickinger, H. *et al.* Experimental Evidence of a <math display="inline"> <mi>φ</mi> </math> Josephson Junction. *Phys. Rev. Lett.* **109**, 107002 (2012).

76. Anwar, M. S. & Aarts, J. Inducing supercurrents in thin films of ferromagnetic CrO 2. *Supercond. Sci. Technol.* **24**, 024016 (2011).

77. Blamire, M. G., Smiet, C. B., Banerjee, N. & Robinson, J. W. A. Field modulation of the critical current in magnetic Josephson junctions. *Supercond. Sci. Technol.* **26**, 055017 (2013).

78. Anwar, M. S., Veldhorst, M., Brinkman, A. & Aarts, J. Long range supercurrents in ferromagnetic CrO 2 using a multilayer contact structure. *Appl. Phys. Lett.* **100**, 052602 (2012).

79. Börcsök, B., Komori, S., Buzdin, A. I. & Robinson, J. W. A. Fraunhofer patterns in magnetic Josephson junctions with non-uniform magnetic susceptibility. *Sci. Rep.* **9**, 5616 (2019).